UNIVERSITÀ DEGLI STUDI DI PADOVA

Dipartimento di Fisica e Astronomia “Galileo Galilei”

Master Degree in Physics

Final dissertation

Lensing voids with peak statistics in massive neutrino cosmologies

Internal thesis advisor

Prof. S. Matarrese

External thesis advisor

Dott.ssa C. Carbone

Thesis co-advisor

Dott. Matteo Calabrese

Candidate

Valentina Picciano

Anno Accademico 2019/2020

Contents

1 The Cosmological Framework **5**
- 1.1 The Friedmann Robertson Walker metric . . . 6
- 1.2 The cosmological constant . . . 8
- 1.3 The matter power spectrum . . . 9
- 1.4 Summary of Chapter 1 . . . 11

2 Massive neutrinos **13**
- 2.1 Massive neutrinos and the Standard Model . . . 13
- 2.2 Massive neutrinos and Cosmology . . . 15
- 2.3 The effect of massive neutrinos on structure formation . . . 16
- 2.4 Summary of Chapter 2 . . . 18

3 Gravitational Lensing **20**
- 3.1 The weak gravitational lensing effect . . . 21
- 3.2 Convergence and cosmic shear . . . 25
- 3.3 Summary of Chapter 3 . . . 26

4 Cosmic Voids **27**
- 4.1 Cosmic voids in cosmology . . . 27
  - 4.1.1 Formation and evolution of voids . . . 28
- 4.2 Algorithms of void finding . . . 29
- 4.3 Summary of Chapter 4 . . . 31

5 Simulated data and analysis pipeline **32**
- 5.1 The DEMNUni cosmological simulations . . . 32
- 5.2 Lensing map making procedure . . . 33
- 5.3 The VOLEs void finder . . . 36
- 5.4 From full-sky to flat-sky . . . 37
- 5.5 Summary of Chapter 5 . . . 39

6 Lensing voids in the massless neutrino scenario **40**
- 6.1 The extraction of convergence peaks . . . 40
- 6.2 Void identification and counts . . . 44
- 6.3 The convergence profile inside voids . . . 50
- 6.4 The shear profile inside voids . . . 52
- 6.5 Summary of Chapter 6 . . . 54

7 Lensing voids in the presence of massive neutrinos **63**
- 7.1 Convergence peaks in the $\nu\Lambda$CDM scenario . . . 63
- 7.2 Void counts in the $\nu\Lambda$CDM scenario . . . 68
- 7.3 Void convergence profiles in the $\nu\Lambda$CDM scenario . . . 71
- 7.4 Void shear profile in the $\nu\Lambda$CDM scenario . . . 73

7.5 Summary of Chapter 7 74

Conclusions **86**

A Check of κ-profiles in the ΛCDM scenario **89**
A.1 κ-profiles for different $N_{\rm side}$ 89
A.2 κ-profile for different $R_{\rm V}$ values 91

B Values of $\Delta(\%)$ between the $\nu\Lambda$CDM and the ΛCDM cosmologies **92**
B.1 $\Delta(\%)$ of the cumulative projected density of lensing peaks 92
B.2 $\Delta(\%)$ of the cumulative projected density of voids 93
B.3 $\Delta(\%)$ of the stacked convergence profile 94
B.4 $\Delta(\%)$ of the stacked tangential shear profile 96

Bibliography **98**

Introduction

The Cosmic Web describes the distribution of structures in the Universe from few Mpc up to scales larger than hundreds of Mpc. It has a foam-like pattern and is composed of knots, filaments, sheets and cosmic voids. The latter is the topic of this thesis.

In the last decades, Cosmic Microwave Background (CMB) experiments and galaxy survey campaigns have highlighted this particular matter distribution, providing information about the evolution and initial conditions from which the Universe has evolved in such an intricate pattern (van de Weygaert and Schaap, 2009). It has been shown that the present cosmological distribution of matter finds its origin in tiny density and velocity perturbations in the early Universe; these perturbations have grown through gravitational instability leading to the formation of large-scale structures (Peebles, 1980).

In particular, the WMAP (Bennett et al., 2013) and Planck (Planck Collaboration et al., 2018) missions have allowed the scientific community to extract almost all possible information from the physics of the CMB. In addition, recent galaxy surveys, such as SLOAN (Abolfathi et al., 2018), BOSS (Alam et al., 2017) and VIPERS (Guzzo and The Vipers Team, 2013; Guzzo and Vipers Team, 2017), have provided important knowledge about the evolution and dynamics of the large scale structure (LSS) of the Universe.

On the one hand, such observations have led to the so-called concordance model of cosmology, *i.e.* the currently accepted and most commonly adopted cosmological scenario, the ΛCDM model. It fits with high level of accuracy the CMB, Supernovae, and Baryon Acoustic Oscillation data, and describes the Universe as a flat and expanding space-time governed by the laws of General Relativity. Its evolution is dictated by the different constituents of the Universe, *i.e.* the ordinary baryon matter (4.9%), the so-called cold dark matter (CDM) (26.8%), and the so-called cosmological constant, Λ, (68.3%), supposed to represent the simplest form of dark energy, the mysterious component of the Universe causing its recent accelerated expansion, whose origin and nature are still unknown.

On the other hand, the discovery of neutrino oscillations demonstrates that at least two neutrino families must have a nonzero mass (Becker-Szendy et al., 1992; Fukuda et al., 1998; Ahmed et al., 2004), evidence for beyond the standard model physics. Cosmological observables provide stringent upper bounds on the sum of active neutrino masses, $\sum_{i=1}^{3} m_{\nu,i}$ (see e.g. Planck Collaboration et al., 2018), and may soon determine the last missing parameter in the standard model.

Furthermore, future galaxy surveys, such as the ESA mission Euclid (Laureijs et al., 2011), and the NASA mission WFIRST (Eifler et al., 2020), in combination with CMB data, will allow a step forward in the knoedge of both the dark energy evolution and neutrino mass.

In this context, cosmic voids represent peculiar structures in the Cosmic Web, as they are under-dense regions in the matter and galaxy distribution of the Universe, as well as the largest structure observed up to now. It is this peculiar characteristic that makes voids a field of interest for the study of the cosmological parameters, dark energy and dark matter. In fact, since they extend up to hundred of Mpc, they are cosmological probes sensitive to large scale effects, as dark energy and free streaming neutrinos. Due to their hot thermal velocities, massive neutrinos are able to escape the gravitational field of dark matter structures, but are trapped inside very large regions as cosmic voids.

In this thesis we study cosmic voids from maps of lensing convergence, κ, with the identifica-

tion of the so-called VOLEs (VOids from LEnsing) (Davies et al., 2018) as under-dense regions in the convergence field. The use of weak lensing convergence maps for the identification of under-densities in the distribution of matter is a relatively new approach for the analysis of void properties.

The staring point of this work is the exploitation of simulated lensing convergence maps, obtained via ray-tracing (Calabrese et al., 2015) across the dark matter distribution of large cosmological simulations. Since the lensing convergence is the integral along the line-of-sight of the dark matter distribution weighted by a geometrical kernel, the identification of voids as under-dense κ regions maintains the nature of voids as being under-density in the total matter distribution field, rather than in the galaxy field which could be affected by bias effects. Among the variety of void finder algorithms present in the literature, we prefer to use an algorithm that directly exploit the convergence field as a void tracer. In this thesis we adopt the tunnel finding method (Cautun et al., 2018), modified in order to analyze convergence fields.

In this thesis we apply the VOLEs finder to a set of weak lensing maps obtained from the Dark Energy and Massive Neutrino Universe (DEMNUni) cosmological simulations (Carbone et al., 2016), in two different cases: the massless neutrinos scenario, which we call ΛCDM cosmology, and the massive neutrino scenario, which we call $\nu\Lambda$CDM. For the latter, we consider a total neutrino mass of $M_\nu \equiv \sum_{i=1}^{3} m_{\nu,i} = 0.16\,\mathrm{eV}$, slightly above the latest constraints from Planck (Planck Collaboration et al., 2018).

In particular we will consider three different lensing probes, all assumed full-sky for simplicity: an ideal CMB-lensing experiment (i.e. sources all located at redshift $z = 1100$), a weak lensing ideal survey with sources all located at $z_\mathrm{s} = 2$, and a weak lensing survey where sources follow the Euclid photometric galaxy redshift distribution. We will analyze such probes, identifying κ-peaks, and combining the so-called peak statistics with the tunnel finding algorithm as void finder, to construct three lensing void catalogs for each of the two cosmological scenarios considered.

This work is structured as follows. In Chapter 1 we introduce the ΛCDM cosmological model, the equations governing the background evolution of the Universe, as well as basic concepts on the clustering of matter perturbations. In Chapter 2 we introduce massive neutrinos, both from the point of view of the Standard Model of particle physics, and from a cosmological point of view; we report about the discovery of ν flavour oscillations, highlighting the need of a model that takes into account a non vanishing mass for these particles. In Chapter 3 we introduce the concept of gravitational lensing focusing in particular on the weak lensing and the different quantities allowing us to quantify such effect. Chapter 4 is devoted to the description of cosmic voids, their properties and their role in the context of gravitational lensing. In Chapter 5 we present our lensing mock maps, and the data analysis pipeline. In Chapter 6, we report our results on lensing void counts and profiles, as well as their redshift evolution in the ΛCDM cosmology, underlying the difference among the three probes considered. In Chapter 7 we focus on the effect of massive neutrinos and how they change void counts and profiles with respect to the massless neutrino case. Finally, in the Conclusions we present our concluding remarks.

Chapter 1

The Cosmological Framework

When the scientific interest towards the study of the Universe brought the necessity of a scientific theory able to describe the whole Universe, it became clear that in order to pursue this goal a guiding principle was needed; then, at the begins of the XXth century, the *Cosmological Principle* has been introduced. This principle claims that on large enough scales the Universe can be considered homogeneous and isotropic from the point of view of a comoving observer(1). This means that on such large scales (more precisely, on length scales larger than hundreds of Mpc) there is not a preferred direction or orientation in the space. Although at first this was just a principle introduced to simplify scientific theories, later on some observations confirmed this assumption (Smoot, 1999). Nowadays it is thought that the model that best describes a Universe with these components is the Λ Cold Dark Matter (CDM) model or ΛCDM model. The main components of the present day Universe are:

- *Dark Energy* ($\sim$ 68 %), it is responsible for the accelerated expansion of the Universe;
- *Dark Matter* ($\sim$ 27 %), it is composed of non-interacting massive particles that have an equation of state dust-like: $p = w\rho$ with w=0, whose nature has not been clarified yet;
- *Baryonic Matter* ($\sim$ 5 %), it is the ordinary matter produced during the Big Bang Nucleosynthesis.

The ΛCDM model is a six free parameters model, this means that six parameters are needed in order to parametrise the ΛCDM model. According to the Planck mission (Planck Collaboration et al., 2018), combining Planck temperature with Planck lensing data, the values of these parameters are written in Tab. 1.1:

(1) A *comoving observer* is an observer that moves with the cosmic flow.

$H_0[c]$	67.66 ± 0.42
τ	0.0561±0.0071
n_s	0.9665 ± 0.0038
$ln(10^{10}A_s)$	3.047 ± 0.014
$\Omega_b h^2$	0.02242 ± 0.00014
$\Omega_m h^2$	0.14240 ± 0.00087

Table 1.1: Cosmological parameters associated to the ΛCDM model with their values from the Planck mission.

1.1 The Friedmann Robertson Walker metric

The model introduced to describe the Universe is based on Einstein's equations of general relativity (GR):

$$G_{\mu\nu} = R_{\mu\nu} - \frac{1}{2} g_{\mu\nu} R = 8\pi T_{\mu\nu} = \frac{1}{M_{\rm Pl}^2} T_{\mu\nu}, \tag{1.1}$$

where $G_{\mu\nu}$ is the Einstein tensor relative to the geometric part (left-hand side) of Einstein's equations, with $R_{\mu\nu}$ and R being the Ricci scalar and the Ricci tensor of the spacetime; $T_{\mu\nu}$ is the stress energy tensor that describes the source of matter-energy of the spacetime and $g_{\mu\nu}$ is the metric tensor that describes the geometric properties of spacetime. Thanks to the Cosmological Principle the energy-momentum tensor from Eq. (1.1) can be written in a simple form

$$T_{\mu\nu} = (\rho + p) u_\mu u_\nu + p g_{\mu\nu}. \tag{1.2}$$

This is the expression of the energy-momentum tensor for a perfect fluid, a fluid with no viscosity, where p is the isotropic pressure and u_μ is the 4-velocity of the fluid. From a geometric point of view our Universe can be described as a 4-dim spacetime with a set of symmetries (the maximum number of symmetries a spacetime of this type can have is ten, as the Minkowski spacetime). In the case of the cosmological model introduced, we have a 4-dimensional spacetime that has a 3-dimensional maximally symmetric space, this means that it has the maximum number of allowed symmetries. Spatial translations and rotations still remain as in the Minkowski case, but not time translation, in fact the Universe we are considering evolves in time, so the assumption of homogeneity is only in space and not in time. The spacetime metric describes the geometrical properties of the Universe. For Minkowski spacetime the line element is expressed as[(2)]:

$$ds^2 = dt^2 - dl^2 = dt^2 - dx^2 - dy^2 - dz^2, \tag{1.3}$$

in Cartesian coordinates, whereas in spherical coordinates it is:

$$ds^2 = dt^2 - dl^2 = dt^2 - d\rho^2 + \rho^2 (d\theta^2 + \sin^2\theta d\phi^2). \tag{1.4}$$

In the case of a Universe where the Cosmological Principle is valid, the most general expression of the spacetime metric is the *Robertson-Walker metric*:

$$ds^2 = dt^2 - a(t)^2 \left[\frac{dr^2}{1 - Kr^2} + r^2 \left(d\theta^2 + \sin^2\theta d\phi^2 \right) \right], \tag{1.5}$$

where $a(t)$ is a function of the cosmic time called *scale factor* and tells us how the Universe is expanding, r is the comoving spatial coordinate, θ and ϕ are the angular comoving coordinates and K is an adimensional constant that refers to the curvature of the Universe. In principle the quantity K can assume three different values that corresponds to three different classes of Universe: $K = 0$ we come back to the case of Minkowski spacetime and we have a flat Universe, $K = 1$ describes a closed Universe and $K = -1$ is for an open Universe.

It is also possible to further simplify the Robertson-Walker metric introducing the concept of conformal time: $dt = a(\eta) d\eta$:

$$ds^2 = a(\eta)^2 \left[d\eta^2 - \left(\frac{dr^2}{1 - Kr^2} + r^2 (d\theta^2 + \sin^2\theta d\phi^2) \right) \right]. \tag{1.6}$$

Solving Einstein's equations of spacetime assuming the line element of Eq.(1.5), we obtain the first Friedmann equation that describes the rate of expansion of our Universe through the Hubble rate $H(t)$:

(2) We are working in natural units, with c=$\hbar$=1

$$H^2(t) = \left(\frac{\dot{a}}{a}\right)^2 = \frac{1}{3M_{\rm Pl}^2}\rho - \frac{K}{a^2}, \tag{1.7}$$

and the second Friedmann equation, called the acceleration equation:

$$\frac{\ddot{a}}{a} = -\frac{1}{6M_{\rm Pl}^2}(\rho + 3p)\,. \tag{1.8}$$

From Eq. (1.8) we see that as long as $(\rho + 3p) > 0$ the Universe is accelerating; since all fluids we are familiar to satisfy this property, it is natural to expect a decelerating Universe, but it is not what happens. In fact, observations of Type Ia supernovae (Riess et al., 1998; Perlmutter et al., 1999) show instead evidences of an accelerated expanded Universe.

Finally, from the continuity equation of the stress-energy tensor

$$D^\mu T_{\mu\nu} = 0. \tag{1.9}$$

it is possible to recover the third Friedmann equation:

$$\dot{\rho} + 3H(\rho + p) = 0. \tag{1.10}$$

Introducing the concept of critical density $\rho_c = 3M_{\rm Pl}^2 H^2$, it is possible to express all densities of the components by mean of a dimensionless unit called *density parameter*, Ω_i, associated to each component, where: $\Omega_i(t) \equiv \rho(t)/\rho_c(t)$ and $\Omega_{\rm TOT}(t) = \sum_i \Omega_i(t)$.

Using $\Omega_i(t)$ the first Friedmann equation (1.7) can be rewritten as:

$$\begin{aligned} H^2(t) &= \frac{1}{3M_{\rm Pl}^2}\sum_i \rho_i(t) - \frac{K}{a(t)^2}, \\ 1 &= \sum_i \Omega_i(t) - \frac{K}{a(t)^2 H(t)^2} = \sum_i \Omega_i(t) + \Omega_K(t), \end{aligned} \tag{1.11}$$

where $\Omega_K(t) = -K/a(t)^2 H(t)^2$ is the parameter density of the curvature. We recover that $1 = \Omega_{\rm TOT}(t) + \Omega_K(t)$ and if $\Omega_{\rm TOT} = 1$ at any time, then $K = 0$, but if $K = 0$ then $\Omega_{\rm TOT} = 1$ is valid for any value of the cosmic time t. Analysis of the CMB measurements combining BOOMERaNG ((Masi, 2002)), Maxima (Balbi et al., 2001), CBI (Wang et al., 2002), WMAP (Komatsu et al., 2009), and Planck (Planck Collaboration et al., 2018) data sets shows that $\Omega_{\rm TOT} \sim 1$, this means that we are in an almost flat spacetime.

If we assume that the density of a fluid ρ is linked to its pressure p through an equation of state (EoS):

$$p = w\rho, \tag{1.12}$$

it is possible to recover the simple scaling relation ρ vs a for each component of the Universe starting from the continuity equation. We are interested in three different kinds of fluid (the three main components of the present-day Universe) and each one of them will have a different EoS.

$$w = \begin{cases} \frac{1}{3} & \text{radiation } (\gamma \text{ and massless } \nu) \\ 0 & \text{matter (ordinary but also dark matter)} \\ -1 & \text{cosmological constant (it accounts for the dark energy content of the Universe)} \end{cases}$$

The continuity equation can be rewritten as:

$$\rho(a) = \rho(a_i)\left(\frac{a_i}{a}\right)^{3(1+w)}. \tag{1.13}$$

The scaling relation will be:

$$\rho \propto \begin{cases} a^{-4} & \text{radiation} \\ a^{-3} & \text{matter} \\ constant & \text{cosmological constant} \end{cases} \tag{1.14}$$

Keeping in mind this scaling relation and going back in time in the evolution history of the Universe, it is possible to identify three main eras through the correspondent values of the scale factor:

- Dark Energy Domination: $a_\Lambda < a < a_0$,
- Matter Domination: $a_{eq} < a < a_\Lambda$,
- Radiation Domination: $0 < a < a_{eq}$.

1.2 The cosmological constant

From the acceleration equation

$$\frac{\ddot{a}}{a} = -\frac{1}{6\,M_{\rm Pl}^2}\,(\rho + 3p)\,, \tag{1.15}$$

it is clear that as long as the term $\rho + 3p > 0$ the Universe is decelerating.

Although at first a possible accelerated expansion of the Universe was excluded since all fluids we are familiar to satisfy this inequality, at the end of the *XX* century two different groups (*Supernova Cosmology Project* and *High-Z Supernova Search Team*) used type Ia supernovae as standard candles to measure the expansion rate of the Universe at different distances and they both found evidences for an accelerated expansion (Perlmutter et al., 1997; Riess et al., 1998).

Obviously this result brought new theories and elements in the physics of the Universe. A possible solution to explain the observed acceleration is to assume the presence of a cosmological constant Λ that appears in the Friedmann's equations as follows:

$$\left(\frac{\dot{a}}{a}\right)^2 = \frac{1}{3M_{\rm Pl}^2}\rho - \frac{K}{a^2} + \frac{\Lambda}{3}, \tag{1.16}$$

$$\frac{\ddot{a}}{a} = -\frac{1}{6\,M_{\rm Pl}^2}(\rho + 3p) + \frac{\Lambda}{3}. \tag{1.17}$$

If $\Lambda > 0$ is the dominant term, the right-hand side of the acceleration equation is positive and a possible accelerating expansion can be explained.

Here, with the cosmological constant term Λ we are introducing also a new component into the Universe beside the ordinary matter, the dark matter and the radiation component. This new element is called *dark energy* and has a characteristic Equation of State $p = w\rho$ where $w = -1$.

We have already seen that in the case of a cosmological constant the energy density ρ_Λ remains constant with the scale factor, so it does not change in time. This means that at some point in the evolution history of the Universe the dark energy component became the dominant component and it drives the present expansion of the Universe. Observations seem to show that the dominance of this cosmological constant starts at $z \sim 1$.

We refer to (Weinberg, 2000; Straumann, 2002) for some history reviews of the cosmological constant problem and the nature of dark energy.

1.3 The matter power spectrum

In order to explain the origin and the evolution of the cosmic structures, we have to take into account primordial matter density perturbations $\delta(x)$. These perturbations came from quantum fluctuations of the scalar field called *inflaton* that filled the Universe in the first stages of its evolution. These density fluctuations, due to gravitational instability, became larger and larger until they generate the cosmic structures we see today, as the Universe during the inflationary period underwent a remarkable expansion of about 60-efolds (Kolb and Turner, 1990).

They can be considered quasi-Gaussian random fields and, as a consequence, can be treated from a statistical point of view as if they were exactly Gaussian; this means that these fields are defined by their mean $< \delta(x) >$ that is zero by definition and their *covariance* or two-point correlation function $\xi(r) = \delta(x)\delta(x+r)$. This field lives in a Robertson-Walker Universe, that geometrically is a spacetime with the three-dimensional spatial component homogeneous and isotropic, this property translates in a definition of a density fluctuation $\delta(x)$ homogeneous and isotropic itself with the two-point correlation function that depends only on the r coordinate with $r = |x_2 - x_1|$.

Moving to Fourier space:

$$\delta(x) = \frac{1}{(2\pi)^3}\int d^3k e^{i\mathbf{k}\cdot\mathbf{x}}\delta_{\mathbf{k}}, \tag{1.18}$$

and the two-point correlation function will be:

$$\xi(r) =< \delta(\mathbf{x})\delta(\mathbf{x}+\mathbf{r}) >= \frac{1}{(2\pi)^6}\int d^3k_1 \int d^3k_2 e^{i(\mathbf{k}_1\cdot\mathbf{x}+\mathbf{k}_2\cdot(\mathbf{x}+\mathbf{r}))} < \delta_{\mathbf{k}_1}\delta_{\mathbf{k}_2} > . \tag{1.19}$$

If the random field is homogeneous and isotropic, also its statistical ensemble will have the same properties, this means that it is possible to write:

$$< \delta_{\mathbf{k}_1}\delta_{\mathbf{k}_2} >= (2\pi)^3\delta^{(3)}(\mathbf{k}_1+\mathbf{k}_2)P(k), \tag{1.20}$$

where the Dirac delta $\delta^{(3)}(\mathbf{k}_1+\mathbf{k}_2)$ ensures translation invariance and the function $P(k)$ called *Power Spectrum* guarantees rotational invariance.

It is possible to show that the power spectrum of our statistical system is simply the Fourier transform of the two-point correlation function

$$\xi(r) = \frac{1}{(2\pi)^3}\int d^3k e^{i\mathbf{k}\cdot\mathbf{r}}P(k), \tag{1.21}$$

$$\xi(r) =< \delta(\mathbf{x})\delta(\mathbf{x}+\mathbf{r}) >=< \frac{1}{(2\pi)^6}\int d^3k_1 \int d^3k_2 e^{i\mathbf{k}_1\cdot\mathbf{x}}e^{i\mathbf{k}_2\cdot(\mathbf{x}\mathbf{r})}\delta_{\mathbf{k}_1}\delta_{\mathbf{k}_2} > \tag{1.22}$$

$$= \frac{1}{(2\pi)^6}\int d^3k_1 \int d^3k_2 e^{i\mathbf{k}_1\cdot\mathbf{x}}e^{i\mathbf{k}_2\cdot(\mathbf{x}\mathbf{r})}\delta_{\mathbf{k}_1}\delta_{\mathbf{k}_2}(2\pi)^3\delta^3(\mathbf{k}_1+\mathbf{k}_2)P(k) \tag{1.23}$$

$$= \frac{1}{(2\pi)^3}\int d^3k_1 e^{-i\mathbf{k}_1\cdot\mathbf{r}}P(k) = \frac{1}{(2\pi)^3}\int d^3k_1 e^{i\mathbf{k}_1\cdot\mathbf{r}}P(k). \tag{1.24}$$

Moving from cartesian coordinates to spherical coordinates in Fourier space the explicit expression of the two-point correlation function will be function of k, θ_k and ϕ_k.

After an integration over the angles it will be:

$$\xi(r) = \frac{1}{2\pi^2}\int dk k^3 P(k)\frac{\sin(kr)}{kr}. \tag{1.25}$$

Now, we focus on the linear regime and study the evolution of density perturbations at this scale.

The equations that describe the evolution of a fluid inside a Universe with a non-static background (remember that Universe evolves) can be written as:

$$\frac{\partial\rho}{\partial t} + 3H\rho + \frac{1}{a}\nabla\cdot(\rho\mathbf{v}) = 0, \tag{1.26}$$

$$\frac{\partial \mathbf{v}}{\partial t} + H\mathbf{v} + \frac{1}{a}(\mathbf{v}\cdot\nabla_{\mathbf{x}})\mathbf{v} = -\frac{1}{a}\nabla_{\mathbf{x}}\Phi, \tag{1.27}$$

$$\nabla^2_{\mathbf{x}}\Phi = 4\pi G a^2 \delta\rho. \tag{1.28}$$

Eq. (1.26) is the *continuity equation*, Eq. (1.27) is the *Euler equation* and Eq. (1.28) is *Poisson's equation*. $H(t)$ is the Hubble constant, $a(t)$ the scale factor and Φ is the Newtonian gravitational potential and $\mathbf{v}$ is the peculiar velocity. We want to write these equation for the evolution of the initial density fluctuation δ in the linear regime, this means that $\delta << 1$ and we can linearise our system.

$$\delta\rho = \rho - \bar{\rho}, \tag{1.29}$$

and

$$\rho = (1+\delta)\bar{\rho}. \tag{1.30}$$

We obtain:

$$\frac{\partial \delta}{\partial t} + \frac{1}{a}\nabla_{\mathbf{x}}\cdot\mathbf{v} = 0, \tag{1.31}$$

$$\frac{\partial \mathbf{v}}{\partial t} + H\mathbf{v} = -\frac{1}{a}\nabla_{\mathbf{x}}\Phi, \tag{1.32}$$

$$\nabla^2_{\mathbf{x}}\Phi = 4\pi G a^2 \delta\bar{\rho}. \tag{1.33}$$

In order to find a solution to this system of equations we go to Fourier space where our vector fields will be $\delta(\mathbf{k}, t)$, $\mathbf{v}$(**k**,t) and Φ(**k**,t).

Now, combining the three equations we get:

$$\ddot{\delta} + 2\frac{\dot{a}}{a}\dot{\delta} - 4\pi G\delta\bar{\rho} = 0. \tag{1.34}$$

If we are in a matter-dominated Universe, then $a(t) \propto t^{2/3}$, $H(t) = 2/3t$ and $\bar{\rho} = 1/6\pi G t^2$ and it is possible to rewrite the second order differential equation as:

$$\ddot{\delta} + \frac{4}{3t}\dot{\delta} - \frac{2}{3t^2}\delta = 0. \tag{1.35}$$

With a substitution we find two different solutions:

$$\delta \propto \begin{cases} t^{2/3} \propto a(t) \\ t^{-1} \propto H(t) \end{cases} \tag{1.36}$$

In particular we introduce $D_+(t)$ that is the growing mode factor and $D_-(t)$ that is the decaying mode factor and we have:

$$\delta(\mathbf{x}, t) = D_+(t)\delta(\mathbf{x}) + D_-(t)\delta(\mathbf{x}). \tag{1.37}$$

Since $D_- \propto t^{-1}$ it becomes negligible in the early stages of the evolution of the Universe, the interesting term is $D_+(t) \propto a(t) \propto t^{2/3}$ that describes the growing mode of the initial density perturbation. As these density perturbations are small, the linear regime approach is able to explain their physical evolution; when the perturbations due to gravitational instability becomes larger, the linear regime is no longer the right approach and we have to pass to the non-linear regime in order to explain structure formation.

1.4 Summary of Chapter 1

In this Chapter we have introduced the ΛCDM model, the standard model of Cosmology with six free parameters. Although up to now this model seems to be the best model to describe the Universe, it is not able to explain the presence of dark energy, whose nature still remains unknown. We know that in its evolution history the Universe passes through different epochs: in its early stages there was the inflationary period, a period of large expansion (we talk about an expansion of 60 e-folds), then there was the radiation dominated era, the matter dominated era and finally the dark energy dominated epoch that it is the one we are living into. Moreover, all the cosmic structure we see (cluster of galaxies, filaments, cosmic voids) are all produced by tiny initial density perturbations of the primordial Universe that grow under the effect of the gravitational instability generating large under-dense regions as well as large over-dense ones. When these perturbations are small, they can be explained by the equations of the linear regime, but when the become bigger, we have to pass to the non-linear regime.

Chapter 2

Massive neutrinos

The ΛCDM model introduced in Chapter 1 does not take into account massive neutrinos, these particles are considered simply massless ones. Although at first the idea of massless neutrinos was supported by the *Standard Model*, with the discovery of the oscillation of atmospheric neutrinos (Fukuda et al., 1998) and solar neutrinos, it became clear that an extension of the ΛCDM model must be introduced in Cosmology as well as a theory beyond the Standard Model must be introduced in Particle Physics. In fact, if we consider massive neutrinos in our model, these particles will have a central role in the structure formation of the Universe and they will leave an imprint on its evolution.

2.1 Massive neutrinos and the Standard Model

Neutrinos are the most peculiar particles among the ones described by the Standard Model of particle physics. They were first hypothesized in the 1930's in the context of the phenomenon of natural radioactivity showed by some nuclei that, even in the absence of external perturbations, emit radiation β (emission of an electron e^- or a positron e^+) (Bilenky, 2013; Dolgov, 2002).

At first it was thought that the decay process for an X atom proceeded this way:

$$ {}^{A}_{Z}X \longrightarrow {}^{A}_{Z+1}X + e^- . \tag{2.1} $$

If this is the real process, then we expect to have monochromatic electrons, so we expect that all e^- emitted have the same exact energy as a consequence of energy and momentum conservation; however, the spectrum observed was a continuum one. This means that, in order to preserve energy and momentum conservation laws, a new particle must be introduced. Actually, the β-decay process proceeds this way:

$$ {}^{A}_{Z}X \longrightarrow {}^{A}_{Z+1}X + e^{-(+)} + \bar{\nu}_e(\nu_e). \tag{2.2} $$

Later, this new particle was called neutrino. According to the Standard Model, neutrinos are massless spin 1/2 fermions with three flavours: $\nu_e(\bar{\nu}_e)$, $\nu_\mu(\bar{\nu}_\mu)$ and $\nu_\tau(\bar{\nu}_\tau)$. At the end of the 1990's the *Sudbury Neutrino Observatory* (SNO) observed neutrino flavour oscillation: neutrinos change flavours as they propagate through a medium (from the Sun toward the Earth or through the Earth atmosphere) and this is possible only if they have masses that are different from zero (see Fig. 2.1 by (Ahmad et al., 2002)).

From the experiments on atmospheric and solar neutrinos we obtain the difference of squared neutrino masses and not the mass relative to each ν flavour:

- atmospheric neutrinos can be understood in terms of the oscillation $\nu_\mu \Longleftrightarrow \nu_\tau$ leading to: (Nakamura and Petkov, 2016)

$$ \Delta m^2_{32} \simeq (2.43 \pm 0.06) 10^{-3}\ (\mathrm{eV})^2 \tag{2.3} $$

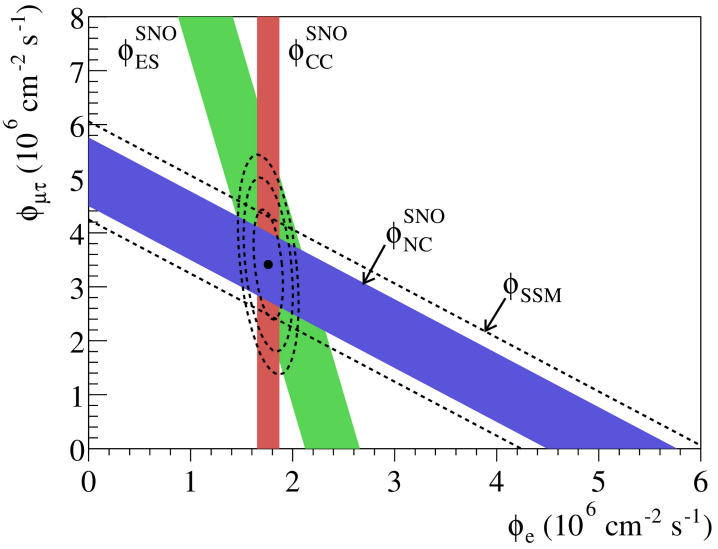

Figure 2.1: ν_e measurement of SNO (red) and the total flux measurement (blue). In green the Super-Kamiokande solar measurements based on ν_e scattering are shown (Ahmad et al., 2002). The measurements all intersect in one point and that is the evidence of the presence of (ν_μ+ν_τ) flux.

- solar neutrinos can be understood in terms of the oscillation $\nu_e \Longleftrightarrow \nu_\mu$ leading to: (Nakamura and Petkov, 2016)

$$\Delta m^2_{21} \simeq \left(7.54^{+0.26}_{-0.22}\right) 10^{-5}\,(\text{eV})^2 \tag{2.4}$$

This brings to two different neutrino mass hierarchy shown in Fig. 2.2.

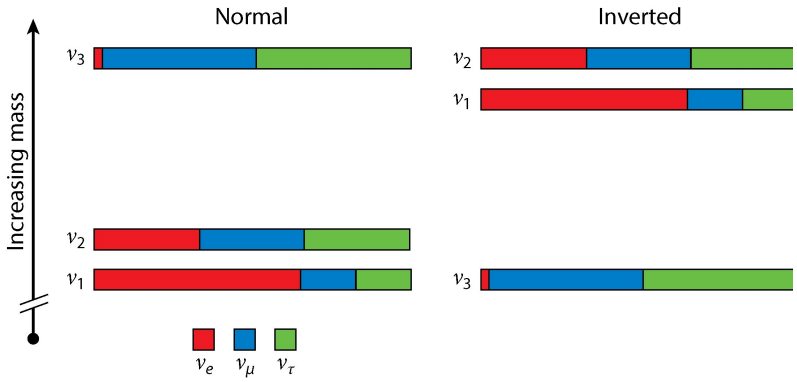

Figure 2.2: Here are shown the two different mass hierarchy: the normal (NH) on the left, and the inverse one (IH) on the right (Patterson, 2015)

The oscillations we have described give information about mass splittings among neutrinos, but we still do not have any bound on the overall mass scale. Actually, the current experimental results are consistent with at least one massless states and two massive ones. The two different hierarchy bring to two different lower bounds for neutrino masses (Esteban et al., 2017):

$$\sum_{i=1}^{3} m_{\nu,i} > 0.056(0.095)\,\text{eV}. \tag{2.5}$$

According to Choudhury and Hannestad (2020), combining data sets from CMB temperature data from Planck 2015, Baryon Acoustic Oscillations measurements from SDSS-III BOSS DR12, the

Type Ia supernovae (SNe Ia) dat aset from Pantheon Sample, the upper bound on neutrino mass in the ΛCDM+$\sum_{i=1}^{3} m_{\nu,i}$ cosmological model with three massive active neutrinos is

$$\sum_{i=1}^{3} m_{\nu,i} < 0.152\,\mathrm{eV} \quad (95\% CL). \tag{2.6}$$

2.2 Massive neutrinos and Cosmology

In the primordial Universe at high temperatures (much higher than the temperatures that are explored in collider experiments) all the particle species are in thermal equilibrium with a thermal bath and the thermalisation is reached through collisions, scattering processes between particles. However, when the temperature of the Universe goes below the mass value of a certain particle, the projected density of that particle is Maxwell-Boltzmann suppressed and that species decoupled from the thermal bath. Quantitatively, the projected density of a particle species i in thermal equilibrium is expressed by Eq. (2.7)

$$n_i = g_i \frac{\zeta(3)}{\pi^2} T_i^3 \begin{cases} 1 & (BE) \\ \frac{3}{4} & (FD) \end{cases} \tag{2.7}$$

whereas the projected density of the same particle species after the decoupling epoch is expressed by Eq. (2.8),

$$n_i = g_i \left(\frac{m_i T_i}{2\pi}\right)^{3/2} exp(-(m_i - \mu_i)/T_i). \tag{2.8}$$

The number of collision N_{coll} is the quantity that makes us understand if a particle is in thermal equilibrium or not:

$$N_{\mathrm{coll}}(T) \simeq \frac{\Gamma(T)}{H(T)}, \tag{2.9}$$

where $H(T)$ is the Hubble constant at a certain temperature T and $\Gamma(T)$ is the collision rate of a particle species. If $N_{\mathrm{coll}} > 1$ the particle species is in thermal equilibrium with a thermal bath and collisions allow the thermalisation, on the contrary if $N_{\mathrm{coll}} < 1$ there are not enough collisions and without thermal equilibrium the particle species decoupled from the thermal bath. In the early stages of the evolution of the Universe, at temperatures above the MeV scales, neutrinos have been continuously produced via weak interactions and scattering processes mediated by weak interactions as well kept them in thermal equilibrium. Neutrino decoupling took place when

$$\Gamma_\nu(T_D) \simeq H(T_D) \tag{2.10}$$

and in this case

$$\frac{\Gamma_\nu(T_D)}{H(T_D)} \simeq \left(\frac{T_D}{1\,\mathrm{MeV}}\right)^3. \tag{2.11}$$

This mean that at a temperature $T_\nu \simeq 1$ MeV neutrinos decoupled from the thermal bath and from that time on they free streamed through the Universe. Neutrinos decoupled when they were still ultra-relativistic particles and their distribution function followed the Fermi-Dirac statistic:

$$f_\nu(p) = \frac{1}{e^{\frac{p}{aT_\nu}} + 1}. \tag{2.12}$$

After that moment the free-streamed until the present time. At T= $T_e \simeq 0.511$ MeV there was the electron/positron decoupling, this moment can be considered a key moment in the evolution history of the Universe. In fact, above T_e photons and neutrinos have the same temperature even if they are decoupled particles, but for $T < T_e$ the effective number degrees of freedom of the

Universe changed and thus also the temperature of the two particle species changed. In particular, we can prove that

$$\frac{T_\nu}{T_\gamma} = \left(\frac{4}{11}\right)^{1/3}, \tag{2.13}$$

and Eq. (2.13) allows the calculation of the present day temperature of neutrino background. The redshift at which neutrinos became non-relativistic particles is:

$$1 + z_\nu(m_{\nu,i}) \simeq 1890 \frac{m_{\nu,i}}{1\mathrm{eV}}, \tag{2.14}$$

and that corresponds to the moment at which the temperature of the Universe dropped below their mass. The neutrino total density today, written in terms of critical density, is

$$\Omega_\nu = \frac{\rho_\nu^0}{\rho_{crit}^0} = \frac{\sum_{i=1}^3 m_{\nu,i}}{93.14 h^2 \mathrm{eV}}, \tag{2.15}$$

here h is the Hubble constant expressed in units of $100\,\mathrm{kms}^{-1}\mathrm{Mpc}^{-1}$.

2.3 The effect of massive neutrinos on structure formation

The discovery of the neutrino flavour oscillation represents the observational evidence that neutrinos have actually a mass that is different from zero; this evidence opens a new scientific investigation toward the measurements of neutrino mass through cosmological observations.

In fact, the common way in particle physics to measure effects of neutrino masses on its mass range Δm_ν is studying β-decays, however this method does not give the hoped results in the small mass range we are considering. Hence the necessity to shift toward cosmological observations, where even the smallest possible mass has a distinguishable impact on the total matter power spectrum. Massive neutrinos leave fundamental imprints on cosmological observations and on cosmic structure formation history that can be used to constrain neutrino properties themselves, in fact finite masses of ν cause a characteristic suppression in the growth of structure formation on scales below the ν free-streaming scale (Lesgourgues and Pastor, 2006, 2012, 2014; Blas et al., 2014).

Generally speaking, cosmology is sensitive to two main neutrino properties: their density, that is related to the number of active species, and their masses (or total mass). The method used to study neutrino properties and their impact on cosmic structure formation is the theory of cosmological perturbation; in this theory each component of the Universe (CDM, baryons and neutrinos) has attached a small value of density contrast δ_i with respect to the cosmological background and this density value is used in the perturbative expansion. Obviously, different values of δ_i mean different evolution.

However, perturbation theory in presence of massive neutrinos can be considered slightly more difficult than perturbation theory in the case of CDM alone; in fact in the case of CDM domination, the expansion parameter is solely the amplitude of the CDM perturbations, whereas in this cosmological model with massive neutrinos added, we have to take into account the combination of CDM and baryons and neutrinos themselves (Saito et al., 2009).

After the moment of thermal decoupling from the thermal bath, neutrinos free-streamed as a collision-less particle fluid with a particular velocity that corresponds to the thermal velocity (Soler et al., 2009):

$$v_{th} = \frac{< p >}{m} \simeq \frac{3T_\nu^0}{m}\left(\frac{a_0}{a}\right), \tag{2.16}$$

where T_ν^0 is the present-day neutrino temperature obtained from Eq. (2.13). The typical scale associated to neutrinos is the free-streaming scale k_{FS}

$$k_{\mathrm{FS}} = 0.82 \frac{\sqrt{\Omega_\Lambda + \Omega_m(1+z)^3}}{(1+z)^2}\left(\frac{m_{\nu,i}}{1\mathrm{eV}}\right) h\mathrm{Mpc}^{-1}. \tag{2.17}$$

From Eq. (2.17) it is possible to recover also the neutrino free-streaming wavelength:

$$\lambda_{\rm FS}(m_{\nu,i}) = a\frac{2\pi}{k_{\rm FS}}. \tag{2.18}$$

For neutrinos becoming non-relativistic during matter domination epoch, $k_{\rm FS,com} = k_{\rm FS}/a$ passes

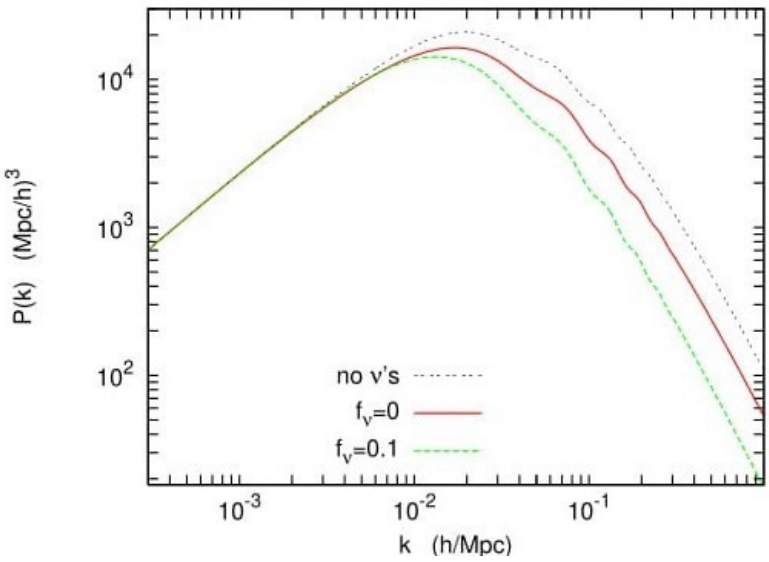

Figure 2.3: Matter power spectrum $P(k)$ in three cases: ΛCDM without neutrinos, a ΛCDM model with massless neutrinos $f_\nu = 0$ and a model $\nu\Lambda$CDM with three massive neutrinos and f_ν=0.1. The impact of the mass of neutrinos on the matter power spectrum is clearly visible: the effect of the shift in the time equality and the reduced Cold Dark Matter fluctuation growth has a consequent attenuation of small-scale perturbations for $k > k_{\rm nr}$ (Lesgourgues and Pastor, 2006).

through a minimum at $k_{\rm NR}$:

$$k_{\rm NR} \simeq 0.018\Omega_m^{1/2}\left(\frac{m_{\nu,i}}{1{\rm eV}}\right)^{1/2} h{\rm Mpc}^{-1}. \tag{2.19}$$

The free-streaming causes a damping of small-scale neutrino density fluctuations but it introduces also a back-reaction effect of damping of metric perturbations too on these scales. At scales larger that $k_{\rm NR}$ neutrinos behave like purely CDM. Coming back to the perturbative approach described in the previous Chapter: the density contrast of the total matter component of the Universe is:

$$\delta_m = \frac{\delta\rho_{\rm CDM} + \delta\rho_\nu + \delta\rho_b}{\bar{\rho}_m}, \tag{2.20}$$

while, if we introduce the corresponding fractional contributions to the matter density f_i, it becomes:

$$\delta_m = f_{{\rm CDM}+b}\delta_{{\rm CDM}+b} + f_\nu\delta_\nu, \tag{2.21}$$

with $f_{{\rm CDM}+b} = (1 - f_\nu)$. The fractional contribution to the density parameter in the case of neutrinos is

$$f_\nu = \frac{\Omega_{\nu 0}}{\Omega_{m0}} = \frac{\sum_{i=1}^{3} m_{\nu,i}}{94.1\Omega_{\nu 0}h^2{\rm eV}}. \tag{2.22}$$

The expression of the total matter power spectrum $P_{mm}(k) =< \delta_m(k)\delta_m(k) >$ in the case of interest will be:

$$P_{mm}(k) = f^2_{{\rm CDM}+b}P_{{\rm CDM}+b}(k) + 2f_{{\rm CDM}+b}f_\nu P^L_{{\rm CDM}+b,\nu}(k) + f^2_\nu P^L_\nu(k), \tag{2.23}$$

or, using the fact that $f_{\mathrm{CDM}+b} = (1 - f_\nu)$:

$$P_{mm}(k) = (1 - f_\nu)^2 P_{\mathrm{CDM}+b}(k) + 2(1 - f_\nu) f_\nu P^L_{\mathrm{CDM}+b,\nu}(k) + f_\nu^2 P^L_\nu(k). \tag{2.24}$$

where the apex "L" means that we are considering just the linear order contribution of massive neutrinos, although they have an impact on the non-linear scale, and $P_{\mathrm{CDM}+b,\nu}$ is the cross spectrum of CDM + b and νs. The factor f_ν in Eq. (2.24) appears to be very small in realistic models. Neutrinos affect the matter power spectrum on the linear growth rate of cosmic structure (Lesgourgues and Pastor, 2006; Saito et al., 2009).

The effect of this scale is that for:

- $k < k_{\mathrm{NR}}$ neutrinos cluster with CDM and baryons;
- $k > k_{\mathrm{NR}}$ the growth rate of CDM is suppressed due to lack of neutrino perturbations (that causes a weaker gravitational force) that at those scales are dumped.

For the scale of the matter power spectrum $P_{mm}(k)$:

$$P_{mm}(k) = \begin{cases} P_{\mathrm{CDM}+b} & k < k_{\mathrm{FS}} \\ (1 - f_\nu)^2 P_{\mathrm{CDM}+b} & k > k_{\mathrm{FS}} \end{cases} \tag{2.25}$$

Fig. 2.3 shows the behaviour of the matter power spectrum $P(k)$ in the case of ΛCDM cosmology without neutrinos, ΛCDM cosmology with massless neutrinos and a νΛCDM cosmology with the three active massive species, highlighting the impact of massive neutrinos on mass distribution.

2.4 Summary of Chapter 2

Neutrinos are considered the most peculiar particles among fermions. At first they were thought to be massless particles, however at the end of the XX century thanks to the observations of SNO the neutrino flavour oscillation was detected. This detection was the direct probe of the massive nature of these particles, so it brought along the necessity of a theory beyond the standard model of particle physics and a theory that takes into account a cosmological model with massive ν. We have taken into account just the linear order contribution of neutrinos to the total matter power spectrum and we have seen how on particular scales neutrinos can influence in a distinguishable way the cosmic structure evolution.

Chapter 3

Gravitational Lensing

Photons travel along null geodesics of the spacetime metric described by ds^2=0, and the presence of sources of mass/energy in their path induces deflections in the direction of the light bundles. This phenomenon of gravitational light deflection is called *Gravitational Lensing* (GL) and it is well described in the context of General Relativity. Light from distant galaxies is deflected on its way toward the observer through an inhomogeneous Universe and light bundles are differentially distorted by tidal fields of the Large Scale Structure components. The interesting property of the gravitational lensing is that it can be considered as a probe of the total matter (ie dark matter and visible matter) content of the Universe without having to take into account dark matter probes.

In this Chapter we introduce the basic concepts of gravitational lensing through a general relativity approach and then we focus on the *Weak Gravitational Lensing* (WL) case in the approximation of weak field and small light deflection angle. In full generality, the main difference between weak gravitational lensing and strong gravitational lensing is that in the first case the net effect is the production of small distortions in the shape of the light sources, whereas in the case of strong gravitational lensing multiple images and Einstein rings of the sources are produced. Moreover, since in the weak field approximation the distortion of the image of a single source is very small, we need a large number of sources in order to be able to detect WL effects. An example of the gravitational lensing effect on the SdSS J 1004+4112 cluster is shown in Fig 3.1 (Sharon et al., 2020).

Figure 3.1: Image showing the cluster SdSS J 1004+4112 (Sharon et al., 2020) with arcs, multiply imaged galaxies and quadruply lensed quasars (Bartelmann, 2010).

3.1 The weak gravitational lensing effect

We have already said that the gravitational lensing by LSS is a probe of the total matter content of the Universe, however it is considered also the most unbiased method that gives a complete picture of the same total matter distribution and its evolution at different redshift values (Van Waerbeke and Mellier, 2003). This is also the reason why this method has been widely used in the course of the last decade for tracing cosmic voids and their evolution history as we will see in Chapter 5. Other techniques such as the ones that use galaxies as tracers or the ones that take into account cosmic velocity fields introduce non-indifferent biases; however the gravitational lensing by LSS is sensible to non-linear power spectrum predictions or to other corrections and that introduces some difficulties in its application.

In Fig. 3.2 a light bundle with two of its light rays is shown; these light-rays L and L' move from a distant source to an observer and are continuously deflected by the inhomogeneities they encounter along their path. First of all we take into account the characteristics of a background homogeneous Universe where the Cosmological Principle is valid. The line element is

$$ds^2 = dt^2 - a(t)^2 \left[\frac{dr^2}{1 - Kr^2} + r^2 d\Omega^2 \right], \tag{3.1}$$

where r is the comoving distance, K is curvature parameter related to the geometry of the space-time and $a(t)$ is the scale factor and it can be written also as

$$a = \frac{1}{1 + z}, \tag{3.2}$$

with z being the redshift value.

Remember that $a_0 = a(t = t_0) = 1$ today.

We can introduce also a new variable χ such that:

$$\chi = \begin{cases} \arcsin(r) & K = +1, \\ \operatorname{arcsinh}(r) & K = -1. \end{cases} \tag{3.3}$$

This way, the expression of the line element can be rewritten as:

$$ds^2 = dt^2 - a(t)^2 \begin{cases} \left(d\chi^2 + \sin^2 \chi d\Omega^2 \right) & K = +1 \\ \left(d\chi^2 + \sinh^2 \chi d\Omega^2 \right) & K = -1 \\ \left(dr^2 + r^2 d\Omega^2 \right) & K = 0 \end{cases} \tag{3.4}$$

And in full generality

$$ds^2 = dt^2 - a(t)^2 \left[d\chi^2 + f_K^2(\chi) d\Omega^2) \right], \tag{3.5}$$

$$ds^2 = a(\eta)^2 \left[-d\eta^2 + d\chi^2 + f_K^2(\chi) d\Omega^2 \right], \tag{3.6}$$

with η conformal time, χ comoving distance and $f_K(\chi)$ angular diameter distance.

As it can be seen in Fig. 3.2 L and L' are two light rays and $d\theta$ is the angular vector between the two. If the Universe at the scales we are considering was homogeneous and there were no cosmic structures, then the physical distance between the two light bundles would be $\xi = f_K(\chi_s) d\theta$, however in their propagation through the cosmic medium photons encounter inhomogeneities such as knots, filaments, voids and cluster of galaxies, that are all fundamental components of the Cosmic Web. Therefore, the expression of the physical distance between the two light rays of the bundle must take into account the presence of these inhomogeneities that causes an infinitesimal relative displacement between L and L'.

In particular, in the presence of inhomogeneities we will have a Newtonian potential Φ different from zero and the line element associated to the spacetime where photons propagate will have a different expression in the presence of local and weak perturbations:

$$ds^2 = a^2(\eta) \left[-(1 + 2\phi) d\eta^2 + (1 - 2\phi)(d\chi^2 + f_K^2(\chi) d\Omega^2) \right], \tag{3.7}$$

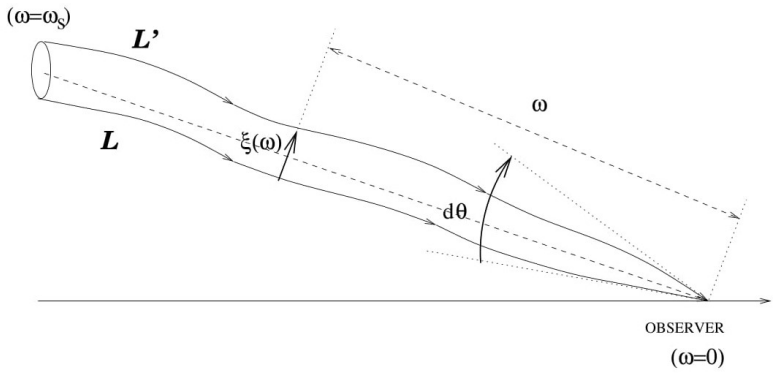

Figure 3.2: Two light rays L and L' moving form a source at $\chi = \chi_s$ toward a distant observer at $\chi = 0$ through a inhomogeneous spacetime (Van Waerbeke and Mellier, 2003).

with

$$\phi = \frac{\Phi}{c^2}, \tag{3.8}$$

(we use natural units, so $c^2 = 1$ and $\phi = \Phi$).

If the perturbations are local they can be considered as embedded in a flat Universe where $f_K(\chi) \sim \chi$.

Thus, the new expression of the line element will be:

$$d\tilde{s}^2 = -(1 + 2\phi)d\eta^2 + (1 - 2\phi)d\vec{\chi}^2. \tag{3.9}$$

Starting from the line element written in Eq. (3.9) it is possible to recover Einstein's equations by mean of the introduction of *vielbeins*, that make the metric of the spacetime *locally* Minkowskian. In this case

$$\theta^0 = (1 + \phi)d\eta, \tag{3.10}$$

$$\theta^i = (1 - \phi)dr^i. \tag{3.11}$$

Through the vielbeins written above we compute the spin connection of the spacetime ω^i, the Riemann tensor or curvature tensor and the Ricci tensor R^{ij} and Ricci scalar R. If we combine homogeneous and local contributions, the inhomogeneous propagation equation of a bundle of light with comoving bundle dimension ξ^i will be:

$$\left(\frac{d^2}{d\chi^2} + K\right)\xi^i = -2\partial^i\phi, \tag{3.12}$$

where K is, as usual, the expression of the curvature. Eq. (3.12) is the equation of the propagation of the light bundle that has to be resolved to obtain the equation for the distortion of the light bundle (Bartelmann, 2010),

$$\xi^i(\chi) = f_K(\chi)\theta^i - 2\int_0^\chi d\chi' f_K(\chi - \chi')\partial^i\phi(\xi^j(\chi'), \chi'). \tag{3.13}$$

In these calculations we use the Born's approximation, this means that we have to introduce an integration along the line of sight of the unperturbed photon path. Although this is just an integration, it seems to well fit the observational data. We integrate from the observer position to the position of a source at coordinate χ_s and defining $\xi^i(\chi_s) = f_K(\chi_s)\beta^i$, from Eq. (3.13):

$$\beta^i = \theta^i - 2\int_0^{\chi_s} d\chi' \frac{f_K(\chi_s - \chi')}{f_K(\chi_s)}\partial^i\phi(f_K(\chi')\theta^j, \chi'). \tag{3.14}$$

The reduced deflection angle is defined as:

$$\alpha^i(\theta^j) := \theta^i - 2\int_0^{\chi_s} dr' \frac{f_K(\chi_s - \chi')}{f_K(\chi_s)} \partial^i \phi(f_K(\chi')\theta^j, \chi'), \tag{3.15}$$

and it is the difference between the angular separation of two light rays in unperturbed and perturbed Universe at comoving distance χ. Combining both equation we obtain the expression of the lens equation:

$$\beta^i = \theta^i - \alpha^i(\theta^j). \tag{3.16}$$

From the definition of reduced deflection angle, it is possible to introduce the concept of *lensing potential*, that is a basic concept of gravitational lensing. First of all we define:

$$\boldsymbol{\alpha}(\theta^j) = \nabla_\theta \psi(\theta^j). \tag{3.17}$$

So the reduced deflection angle is simply the angular gradient on the sphere of the lensing potential, whose expression in:

$$\psi(\theta^j) = 2\int_0^{\chi_s} dr' \frac{f_K(\chi_s - \chi')}{f_K(\chi_s) f_K(\chi')} \phi(f_K(\chi')\theta^j, \chi'). \tag{3.18}$$

Physically, the lensing potential assigns a number to each point of the observer sky $\boldsymbol{S}^2$, it is a map

$$\psi : \boldsymbol{S}^2 \longrightarrow \boldsymbol{R} \tag{3.19}$$

$$p \longmapsto \psi(p) \tag{3.20}$$

where p is a random point in the observer sky.

From the definition of $\boldsymbol{\alpha}$ can recover the convergence κ that is (Bartelmann, 2010):

$$\kappa(\theta^i) = \frac{1}{2} \nabla_\theta \cdot \boldsymbol{\alpha}(\theta^i)\,. \tag{3.21}$$

The process of assigning a value of each point of the sky introduces a map ϕ that sends each point of the observer sky to the surface of a sphere where all the sources are located:

$$\phi : \boldsymbol{S}^2 \longrightarrow \boldsymbol{S}^2 \tag{3.22}$$

$$p \longmapsto \phi(p) \tag{3.23}$$

The differential $D\phi$ describes how a source may change and be deformed by the lens mapping. The elements of these matrix are:

$$D\phi^i_j = A^i_j = \frac{\partial \beta^i}{\partial \theta^j} = \delta^i_j - \frac{\partial \alpha^i}{\partial \theta^j} = \delta^i_j - \frac{\partial^2 \psi}{\partial \theta^i \partial \theta^j}, \tag{3.24}$$

and

$$A^i_j(\theta) = \delta^i_j - 2\int_0^{\chi_s} d\chi' \frac{f_K(\chi_s - \chi')}{f_K(\chi') f_K(\chi_s)} \phi^i_{,j}(f_K(\chi')\theta^j, \chi'), \tag{3.25}$$

with A^i_j *amplification (magnification) matrix*. From a geometrical point of view, the meaning of this matrix can be understood from Fig. 3.3.

The amplification matrix depends on the values of the convergence field κ and the shear field γ and all these quantities contain important cosmological information. Obviously, if there are no inhomogeneities in the path of the photons, then

$$A^i_j = \delta^i_j, \tag{3.26}$$

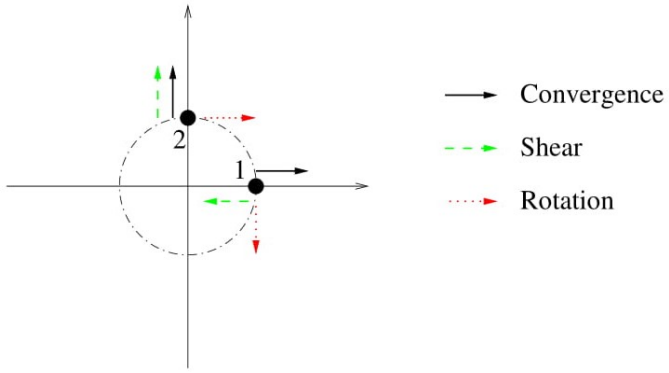

Figure 3.3: Effect of κ (convergence), γ (shear) and ω (rotation) on the displacement of two test particles 1 and 2 placed on a test ring (Van Waerbeke and Mellier, 2003).

with the Newtonian gravitational potential $\Phi = 0$; however, this is not a real description of what happens along the path of a light-bundle. The deformations that occur on to a light bundle can be expressed after an integration along the line of sight as:

$$A^i_j = \begin{pmatrix} 1-\kappa & 0 \\ 0 & 1-\kappa \end{pmatrix} - \begin{pmatrix} \gamma_1 & \gamma_2 \\ \gamma_2 & -\gamma_1 \end{pmatrix} \tag{3.27}$$

$$\kappa = \frac{1}{2} Tr(A^i_j), \tag{3.28}$$

$$\gamma = \gamma_1 + i\gamma_2, \tag{3.29}$$

$$\gamma_1 = \frac{1}{2}(A^1_1 - A^2_2), \tag{3.30}$$

$$\gamma_2 = A^1_2 = A^2_1. \tag{3.31}$$

In the weak field approximation $\kappa << 1$ and $\gamma << 1$. Practically, the convergence κ induces a change in the size of a lensed galaxy, whereas the shear introduces distortions in the shape of the same lensed galaxy, as shown in Fig. 3.4.

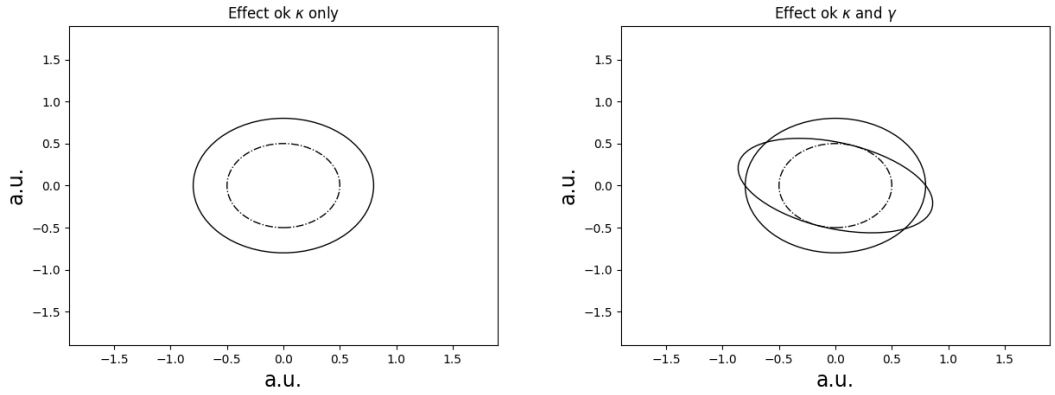

Figure 3.4: Effect of convergence only (left panel) and of the convergence, κ, combined with the shear, γ, (right panel) on the shape of a source of photons. Dot-dashed lines represent the source in its original shape (ie. a circle), while solid lines show the impact of a WL field.

3.2 Convergence and cosmic shear

We have seen that the gravitational lensing phenomenon is a probe of the total matter content of the Universe. From a cosmological point of view the most used method to investigate the structure and the evolution of the Universe is the *cosmic shear* technique of WL, a method based on the measurements of weak distortions induced on background galaxies by photons propagating and interacting with the inhomogeneities of the Cosmic Web, Fig. 3.5 (Refregier, 2003). It is easy to understand what is the main difference between the cosmic shear method and other methods used to probe cosmological properties of the Universe: while the latter relies on the detection of the distribution of luminous sources, the WL based method uses deflections of light-bundles to trace the total matter content of the Universe. And this direct detection of the distribution of matter is useful to constrain cosmological parameters. Coming back to the explicit expression of the

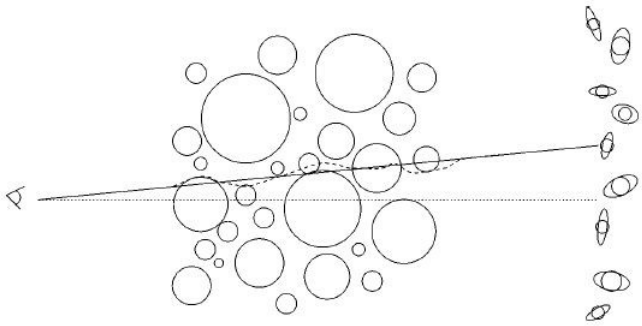

Figure 3.5: Effect of WL by LSS. Light-bundles from distant galaxies (right) travel to an observer (left) as they are deflected by intervening LSS of the Universe (middle). The result is a distortion in the observed shapes of the background galaxies. These distortions are on the order of a few percent in amplitude and can be measured giving a direct map of the distribution of mass in the Universe (Refregier, 2003).

amplification matrix A, we have seen that this matrix depends directly on the convergence κ that physically is the projected mass along the line of sight and it describes the isotropic dilation of the sources; A depends also on the complex shear γ, that quantifies the distortions of the sources along an axis, and it has also a part associated to a rotation ω of the image, but this term vanishes at first order approximation. Moreover, the gravitational potential Φ is related to the fluctuations of the density contrast δ through the Poisson's equation:

$$\nabla^2\Phi = 4\pi G\rho_m, \tag{3.32}$$

with ρ energy density of the Universe. It is possible to introduce the quantity δ that is the density contrast defined as:

$$\delta(\vec{x}) = \frac{\rho(\vec{x}) - \bar{\rho}}{\bar{\rho}}. \tag{3.33}$$

If we recall that the density parameter associated to the total energy density of the Universe is $\Omega_m = \rho/\rho_{crit}$ and that $\rho_{crit} = 3H_0^2/8\pi G = 3H_0^2M_{\rm Pl}^2$, then we can rewrite Poisson's equation as:

$$\nabla^2\Phi = \frac{3}{2}H_0^2\Omega_m(1+z)\delta. \tag{3.34}$$

Combining together the explicit expression of the convergence κ in Eq. (3.28) and the expression of the lensing potential we have that:

$$\kappa(\xi^j) = \int_0^{\chi_s} d\chi' \frac{f_K(\chi')f_K(\chi_s-\chi')}{f_K(\chi_s)}\partial_{\xi^i}\partial^{\xi^i}\phi(\xi^j,\chi'), \tag{3.35}$$

where the partial derivative is done with respect to the comoving radial distance between two light-rays of the bundle and in the direction perpendicular to the line of sight. Finally, combining together Eq. (3.35) and Poisson's equation Eq. (3.32)

$$\kappa(\theta^i) = 4\pi G \int_0^{\chi_s} d\chi' \frac{f_K(\chi') f_K(\chi_s - \chi')}{f_K(\chi_s)} \rho(f_K(\chi')\theta^i, \chi'). \tag{3.36}$$

Using Eq. (3.34) instead:

$$\kappa(z_s) = \frac{3\Omega_m H_0^2}{2} \int_0^{\chi_s} d\chi' \frac{f_K(\chi') f_K(\chi_s - \chi')}{f_K(\chi_s)} (1+z)\delta(\chi'). \tag{3.37}$$

We have shown that the convergence κ is the weighed surface-mass density of the lensing matter inhomogeneities and that WL allows the measurement of the projected density field along the line of sight.

3.3 Summary of Chapter 3

In this Chapter we have introduced the phenomenon of gravitational lensing that can be described in the context of General Relativity. This phenomenon consists in the deviation of light rays as they encounter mass/energy sources along their path, in cosmological context, these sources are simply the structures of the Cosmic Web (cluster of galaxies, filaments, voids). Gravitational lensing can show up in the form of

- Strong Gravitational Lensing, in this case multiple images of the source are seen;
- Weak Gravitational Lensing, in this case we do not see multiple images of one source, but just a distortion of its image.

The values that allow the quantification of this distortion mechanism are the convergence κ that describes the isotropic stretching of the source and the shear γ that describes its distortion along the ξ axis, that is the axis perpendicular to the line of sight.

Chapter 4

Cosmic Voids

The cosmic matter distribution on scales of hundreds of Mpc displays a characteristics foam-like pattern, called *Cosmic Web*. Galaxies and mass on such large scale are arranged in elongated filaments, knots, sheet-like walls and voids, that are vast under-dense regions. A representation of the Cosmic Web can be seen in Fig. 4.1.

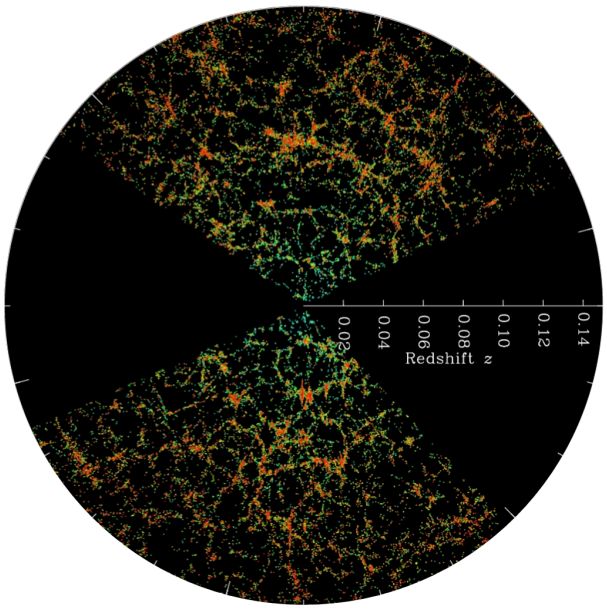

Figure 4.1: SDSS distribution of local galaxies (`www.sdss3.org/science/`). Under-dense regions of galaxies, i.e. cosmic voids, are clearly visible.

The investigation of this spatial distribution of matter can give us information about both the physical forces at work and the conditions under which the Universe evolved in a morphology like the one we observe. In this Chapter we will consider and analyse the properties of Cosmic Voids, that constitute the major component in the galaxy distribution volume.

4.1 Cosmic voids in cosmology

Cosmic voids are under-dense regions of the large scale (from ten up to hundred of Mpc) Universe surrounded by the other components of the Cosmic Web; their property of being a low density environment implies that voids are slightly affected by complicated non-linear gravitational effects, differently to what happens in over-dense regions as the clusters of galaxies. The scientific interest

toward the study of cosmic voids began with the observation and the analysis of the first galaxy surveys and with the discovery of the first dramatic specimen: the *Boötes Void*, the emptiest region in the known Universe (van de Weygaert and Platen, 2011). Since that discovery, voids have been considered among the main interesting features of the Cosmic Web with a key role in the spatial distribution of matter in the Universe (Gruen et al., 2016; Brouwer et al., 2018). It can be wrongly thought that voids are simple vacant spaces, however they contain a complex multi-level hierarchical dark matter substructure that every void finding algorithm should take into account. This means that the fact that voids are objects largely dominated by dark matter, coupled with the fact that voids undergo simple dynamics, make them a unique probe of cosmological parameters as well as interesting regions for studying astrophysical phenomena. In particular matter distribution inside voids is sensitive to the sum of neutrino masses and to different theories of gravity. The latter is caused by the fact that, since voids are low density environments of the Cosmic Web, the screening mechanism associated to modified gravity models does not take place.

4.1.1 Formation and evolution of voids

Studying the matter distribution and evolution in the Universe with voids makes highlights how the moment of formation of the first voids represents the transition scale at which density perturbations have decoupled from the Hubble flow and contracted into the structural features of the Cosmic Web (van de Weygaert and Platen, 2011). One property of cosmic voids found in the first observations of galaxy surveys as well as in the first N-body simulations is a net repulsive force inside them exerted over the surroundings. This property underlines the key role of voids in the evolution of matter distribution and the formation of filaments and sheet-like walls due to squeezing of matter. In Fig. 4.2 it is possible to see snapshots of evolution of a single void in a ΛCDM scenario.

From these snapshots of void evolution history we can recover some of their main properties. First of all, because of the net repulsive force inside voids and the outward flow of matter, they tend to expand with respect to the cosmic background and this expansion is faster than the Hubble flow; as a result, density inside voids decreases until, in a perfect ideal situation of an isolated spherical void, it would reach the value of $\delta = -1$, that corresponds to emptiness in terms of matter content. Secondly, as the mass inside voids continuously moves outward, the mass inside voids becomes more and more uniform, giving rise to a sort of low-density Friedmann-Robertson-Walker Universe inside the void itself. As matter moves toward the exterior of the under-density and accumulates on the boundaries, its peculiar gravitational acceleration decreases, resulting in the formation of the usual Cosmic Web structures: filaments and sheet-like walls. As the outflow of matter increases, substructures inside the void decrease. This means that it is not possible for massive object to form and evolve inside large voids; this fact explains also the reason why we see a shift of the mass spectrum of dark halos toward small masses. Actually, from a physical point of view, we will never encounter an isolated and perfectly spherical void, however this type of approximation leads to a better understanding of the basic concepts of the formation and evolution of real cosmic voids. Therefore, if we consider the evolution of an isolated and spherical voids, it proceeds as described before and the result of this evolution will be an increasingly empty void.

In the context of massive neutrino cosmologies, mainly three-dimensional distribution of voids have been considered, in particular, Massara et al. (2015); Kreisch et al. (2019); Schuster et al. (2019) have probed the effect of different massive neutrino cosmology on cosmic void properties and statistics using the DEMNUNi simulations using the VIDE (Sutter et al., 2015) algorithm to define a void.

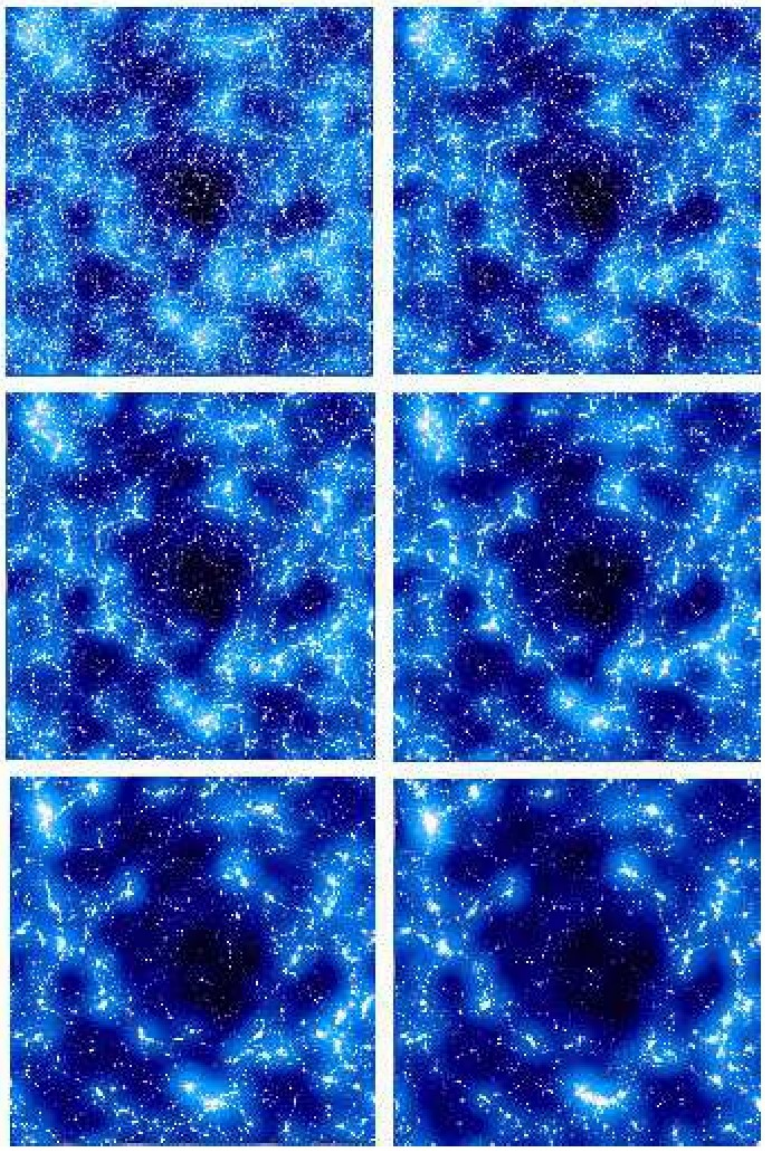

Figure 4.2: Simulation of the evolution of a cosmic void at different time steps (scale factor from top to bottom, $a = 0.05, 0.15, 0.35, 0.55, 0.75$ and 1.0) in a ΛCDM scenario (van de Weygaert and Platen, 2011).

4.2 Algorithms of void finding

We have said that cosmic voids are under-dense regions of the Megaparsec Universe and they are surrounded by an intricate network of DM halos and their galaxies.

Since voids represent a pristine environment of the Universe and their analysis can put constraints on cosmological parameters, several algorithms for the identification of cosmic voids have been introduced.

From a theoretical point of view, voids are simply low density regions in the large-scale matter field. However, because the full mass distribution is not easily observable, observational studies typically identify voids using the galaxy distribution (Davies et al., 2018).

Several void finders can be found in the literature: Voronoi tessellation and Watershed methods (Platen et al., 2007), Delaunay triangulation (Zhao et al., 2016) and others; the majority of them are applied to data obtained from surveys and simulations and they use galaxies with spectroscopic redshifts to define voids.

Beside them, also galaxies with photometric redshifts (photo-z's) have been introduced in the literature. These redshifts are far less precise than the correspondent spectroscopic ones and when they are applied to our data the void-finding process needs to be slightly modified in order to overcome the smearing in the line-of-sight position of the tracer galaxies (Sánchez et al., 2017).

The spectroscopic surveys have the disadvantage that are expensive in terms of time and may be affected by limited depth, incompleteness or they may suffer from selection effects. On the contrary photometric surveys such as SDSS (York et al., 2000) and LSST (Refregier, 2003), for example, are preferable since they are more complete and they are almost unaffected by selection bias; however, due to their limited resolution in the positions of the galaxies on the line of sight, they do not provide a complete 3D information of the galaxy distribution.

What are the main properties of the voids identified from photometric redshift tracers?

If this voids have the size of the photo-z error or if they are even smaller, they will no be seen by the algorithm. Moreover, due to photo-z scatter, it will find spurious voids. It can be deduced that all the algorithms that work with photometric redshift surveys must take into account all these information in order to pursue a complete analysis of voids. The Dark Energy Survey, for example, is a photometric redshift survey that covers about one eight of the sky imaging about 300 million galaxies in 5 broadband filters up to redshift z = 1.4 (Nadathur et al., 2017).

We have seen that the majority of void finders identify voids using galaxies as tracers. However, due to the sparsity of these types of tracers (Neyrinck et al., 2014), there is a complex relation between visible matter and such cosmic voids. In particular, galaxy voids seem to be less underdense than they would be if identified from the total matter distribution. Furthermore, it can be very difficult to test cosmological parameters from voids identified from simulated galaxies in cosmological parameters that could also weaken the lensing signal.

This is the reason why some algorithms of void finding have been introduced in the literature and these void finders identify cosmic void from lensing convergence maps.

During the past decades the gravitational lensing field has been widely studied and various observations have proved the existence of strong, weak and microlensing. It has been observed that matter between the source and the observer acts like a converging lens on light rays leading to an image splitting, magnification and distortion of the source. This is what happens in the case of intervening matter concentration on the photon paths. But, what do we can say in the case of intervening under-dense regions, the so called voids? Actually, voids do affect the propagation of light bundles, so it is possible to use the gravitational lensing as an identification method for voids. In particular, a light ray passing through an under-dense region is deflected away from its center because it is attracted by matter accumulation on the walls, on void boundaries. It is necessary to take into account the effect of voids in lensing since voids are large under-dense regions of the Cosmic Web and they constitute the 70% of the volume of the Universe.

(Krause et al., 2013) demonstrates that the matter density profile of cosmic voids in the redshift range $0.4 < z_l < 0.6$ can be constrained from the average lensing signal of stacked voids, both from the convergence profile $\kappa(r)$ and from the tangential shear signal $\gamma_t(r)$; thus lensing maps play an important role in the analysis of the properties of cosmic voids. The technique of void stacking allows to achieve a larger significance in measuring the lensing signals induced by smaller voids. In Fig.4.3 we see the results obtained by (Krause et al., 2013) with the void stacking method.

These plots show that convergence and shear signals can measure and identify the extent of walls, structures at the boundary of voids.

However, the ellipsoidal shape of individual voids will smooth the over-dense ridges, if each single void has a However, if individual voids have sharp overdense ones.

In this work we will use an algorithm of void finding that identifies cosmic voids from simulated convergence maps; we will also use, among the other CMB-lensing convergence maps, a convergence maps with a Euclid-like photometric redshift distribution that will help us to understand the properties of lensing voids at lower redshifts.

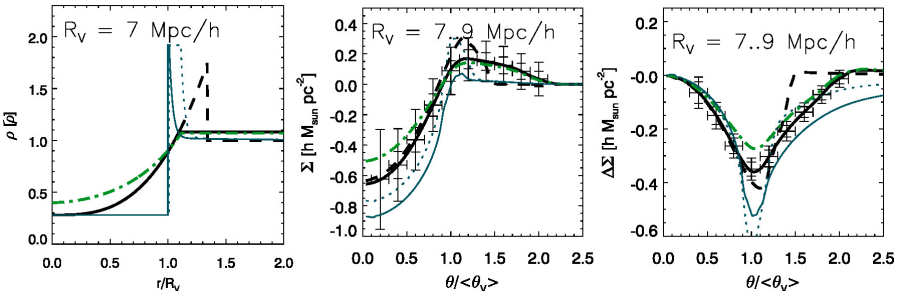

Figure 4.3: Impact of void density profile on lensing signal (Krause et al., 2013).

4.3 Summary of Chapter 4

In this Chapter we have introduced the Cosmic Web and we have presented one of their most prominent elements: cosmic voids. We have said that cosmic voids are regions of the Universe characterised by having a low density environment and this property makes them a unique probe of cosmological parameters as well as interesting elements for the study of the modified gravity theory. We have briefly introduced the basic notions of the evolution history of a void and how in our theory we used to simplify their structure and their interaction with the surrounding environment. Finally we have combined the analysis of cosmic voids with the concept of WL trying to underline from a theoretical point of view what are the main elements that we need to study voids identified in lensing convergence maps.

Chapter 5

Simulated data and analysis pipeline

The goal of this thesis is studying the evolution of number densities and profiles of voids identified in WL maps via the so-called κ-peak statistics. We will consider two different cosmological scenarios: the first one where neutrinos are considered massless particles, which we call the ΛCDM model of the Universe; the second one where neutrinos have a mass different from zero (in our case fixed at M_ν=0.16 eV), which we call the $\nu\Lambda$CDM model of the Universe.

In order to pursue this aim we will use mock data from cosmological simulations, which are able to reproduce the nonlinear evolution of the Universe together with its properties in different cosmological scenarios. In this context we will exploit the Dark Energy and Massive Neutrino Universe (DEMNUni) cosmological simulations (Carbone et al., 2016), and the lensing maps obtained via direct ray-tracing across their dark matter distribution as provided by the Lens2Hat code (Calabrese et al., 2015; Fabbian et al., 2018; Hilbert et al., 2020).

5.1 The DEMNUni cosmological simulations

The DEMNUni simulations have been produced using a modified version of the tree particle mesh-smoothed particle hydrodynamics code GADGET-3 which includes massive neutrinos as a particle component. In particular, this code follows the evolution of CDM alone (ΛCDM scenario) or the evolution of CDM plus massive neutrinos particles ($\nu\Lambda$CDM scenario) treating them as collisionless species. The simulations are characterized by a starting redshift, $z_{in} = 99$, and a comoving volume of $(2h^{-1}\mathrm{Gpc})^3$ filled with 2083^3 CDM particles and 2083^3 massive neutrino particles in the $\nu\Lambda$CDM scenario[(1)].

The baseline cosmology of the DEMNUni suite implements the cosmological parameters from the Planck-13 data analysis (Planck Collaboration et al., 2014), namely a flat ΛCDM model generalised to a $\nu\Lambda$CDM framework by changing only the value of the sum of the three active neutrino masses M_ν:

$$M_\nu = \sum_{i=1}^{3} m_{\nu,i} = (0.0, 0.16, 0.32, 0.53)\,\mathrm{eV}, \tag{5.1}$$

where Ω_m and the amplitude of primordial curvature perturbations, A_s, are kept fixed. In this work we will consider only the cases $M_\nu = 0, 0.16$ eV. For each simulation, 63 particle snapshots have been produced in the redshift range $z = [0, 99]$. From the latter full-sky lightcones have been constructed in order to produce different lensing maps as described in the next section.

(1) Baryon physics is not included in the DEMNUni simulation suite, due to the expensive computational costs. However, recent studies found out that baryon effects are mostly independent of cosmological parameters and from neutrino masses in particular (Mummery et al., 2017).

5.2 Lensing map making procedure

The lensing observable maps are extracted with a post-processing procedure acting on the N-body snapshots to create a full-sky *lightcone*. This procedure was developed to perform high-resolution CMB lensing simulations (Calabrese et al., 2015; Fabbian et al., 2018) in order to implement a multiple lens ray-tracing algorithm in spherical coordinates on the full sky.

The current version of the code reconstructs a full-sky, backward lightcone around an observer placed in the center, using the particle snapshots out to the comoving distance of the highest redshift available from the simulation, following Calabrese et al. (2015). To overcome the finite size of an N-body simulation box, the code replicates the box volume the number of times in space necessary to fill the entire volume between the observer and the source plane. Moreover, the code can randomize the particle positions, as described in (Carbone et al., 2008, 2009), throughout flips and shifts, to minimize any numerical artifacts due to the repetition of the same structures along the line of sight.

The backward lightcone is then sliced into 63 full-sky spherical shells with the following scheme: the median comoving distance spanned by each shell coincides with the comoving distance at the redshift of each N-body snapshot. Any particle inside each of these shells is projected onto 2D spherical maps; the resulting surface mass density Σ on each sphere is thus defined on a two-dimensional grid. For each pixel of the i-th sphere one has

$$\Sigma^{(i)}(\boldsymbol{\theta}) = \frac{n\, m_X}{A_{\rm pix}}\,, \tag{5.2}$$

where n is the number of particles in the pixel, $A_{\rm pix}$ is the pixel area in steradians and m_X is the particle mass of type X (dark matter, or neutrino) from the N-body simulation in each pixel. For this work, the code produces a full-sky convergence map on a HEALPix[(2)] `http://healpix.sourceforge.net` grid (Gorski et al., 1999) with $N_{\rm side} = 4096$, which corresponds to a pixel resolution of 0.85 arcmin. Finally, the lensing convergence of a source plane at redshift $z_{\rm s}$ is computed in the Born approximation as the weighted sum of surfaces mass density, accordingly to the discretized form of Eq.(3.37).

The angular position of the center of each HEALPix pixel coincides with the direction of propagation of the rays in the Born approximation. Several lensing observables can be then constructed simply by changing the source distance (or redshift $z_{\rm s}$), which will affect the geometrical weight in the sum of Eq. (3.37).

For the simulated CMB-lensing signal the integration up to a lens redshift $z = 99$ is able to capture $\sim 99\%$ of the power. In this thesis we will consider different probes, i.e. CMB-lensing convergence maps with $z_{\rm s} = 1100$ and lens-planes up to $z = 99$, weak-lensing convergence maps with sources all located at the same redshift $z_{\rm s} = 2$, as well as a Euclid photometric redshift distribution of galaxies (Laureijs et al., 2011).

In Fig. 5.1 we show some examples of full-sky lensing-convergence maps for these three probes, both in the massless and massive neutrino cases. In the next chapters we will be more quantitative. Here, qualitatively its difficult to appreciate any difference from a first visual inspection. However, we can still infer the suppression of matter perturbations (enclosed in κ) due to free-streaming massive neutrinos, especially at low redshifts where they are non-relativistic. In fact, this is evident from the smaller κ-range in the map color bar for the $\nu\Lambda$CMD scenario as compared to the ΛCMD one, in the case of the WL($z_{\rm s} = 2$) and Euclid convergence maps.

The need of introducing a pixelization technique goes back to the first satellite missions aimed at measuring the CMB anisotropies, such as the NASA Wilkinson Microwave Anisotropy probe (WMAP) (Bennett et al., 2013) and the Planck mission (Planck Collaboration et al., 2018). These missions produced massive data-sets for the construction of full-sky maps of the microwave sky

(2) The Hierarchical Equal Area isoLatitude Pixelisation (HEALPix) of a 2-sphere is a general class of spherical projections, sharing several key properties, which map the 2-sphere to the Euclidean plane

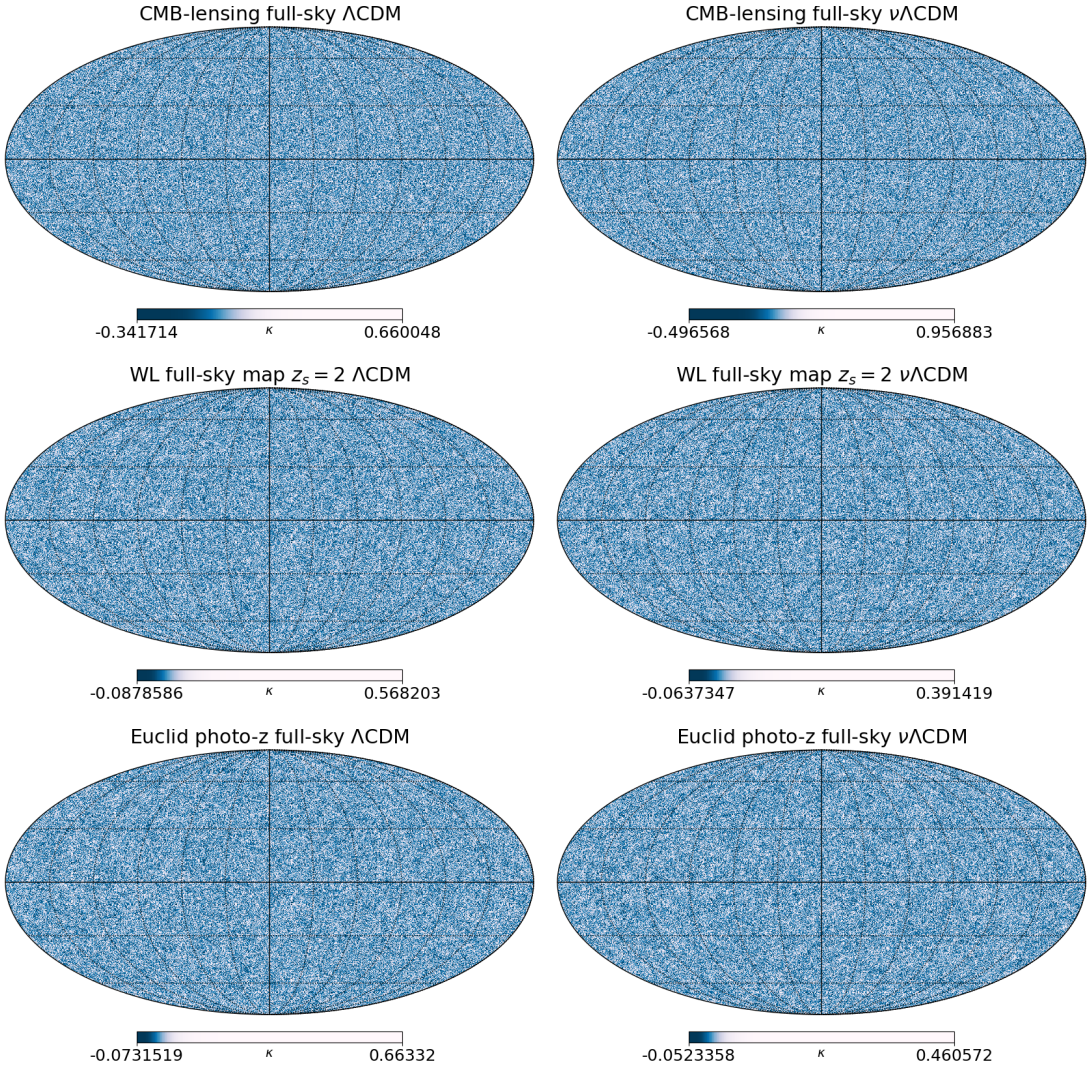

Figure 5.1: Examples of full-sky κ-maps with HEALPix data structure where N_{side}=4096 and a *nest* ordering has been chosen.

with few arcminutes of angular resolution, giving rise to the necessity of creating a mathematical structure able to support a discretization of functions defined on a sphere with a suitable resolution, and able to provide a fast and ready-to-use statistical analysis of cosmological and astrophysical data. Three are the main HEALPix characteristics:

- The sphere is tessellated into quadrilaterals of equal area and the lowest resolution of a HEALPix map consists in the subdivision of the 2-sphere into twelve quadrilaterals. Obviously, the resolution of a pixelization of the sky increases by division of each pixel into other four as can be seen in Fig. 5.2;

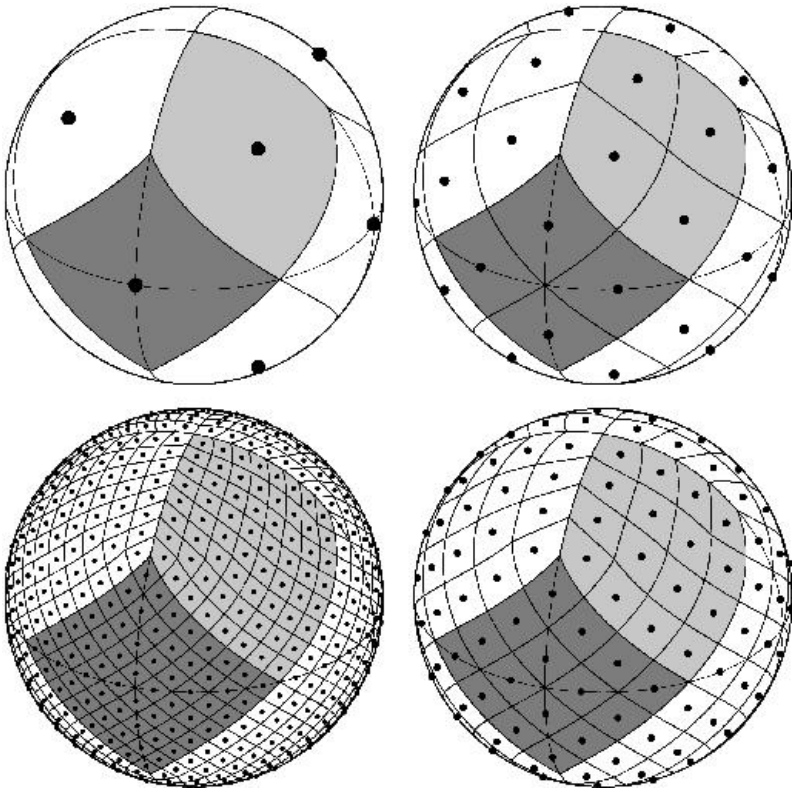

Figure 5.2: A simple image showing how the increasing pixel resolution changes the pixelization of a sphere (Gorski et al., 1999).

- all pixel areas are identical for a given resolution;
- all pixels are distributed on lines of constant latitude.

The resolution of the HEALPix maps is fixed choosing a value of $N_{\rm side}$ which defines the number of divisions along the side of a base-resolution pixel that is needed to reach a desired high-resolution partition. From a geometrical point of view, two are the numbering schemes for the pixels: the *NEST* ordering, where the pixel indices are arranged in twelve tree structures, and the *RING* ordering, where each pixel is placed on the map moving down from the north to the south pole along the iso-latitude ring. Since the NEST ordering with its tree structure allows the user to implement all the computational routines involving nearest-neighbour searches, in this work we will use this type of ordering scheme. The total number of pixels of a HEALPix map is given by $N_{\rm pix} = 12 * N_{\rm side}^2$.

5.3 The VOLEs void finder

There are several types of void finding algorithms that start from different input data and search for voids inside them. In this work we use a new type of void finding algorithm, the so called *VOids from LEnsing* (VOLEs) void finder. As the name suggests, it is used to find cosmic voids starting from lensing maps projected onto 2D Cartesian planes. Weak lensing measurements using upcoming large area and deep imaging surveys such as Euclid (Laureijs et al., 2011) and LSST (Tyson, 2002) will provide the possibility to constraint the profile of voids and to have information about their total matter content and evolution in time.

Why is it interesting to move our investigation from measurements directly performed on the galaxy density field to measurement performed, instead, on the lensing convergence field? As we already mentioned, voids correspond to low density regions in the large-scale matter eld distribution; however, since the full mass distribution is difficult to observe, observational studies typically identify voids using the galaxy distribution. Here there is a problem: due to the sparsity of galaxy tracers and their bias the relation between matter and voids identified by galaxies is quite complicated, with galaxy voids being less under-dense than would be if identied via the full matter density eld (Davies et al., 2018).

The lensing convergence field represents the projected line-of-sight matter density field weighted by the lensing kernel, therefore the identified under-densities correspond to voids in this projected field. As a consequence, using weak lensing maps to identify voids provides the chance of reducing possible galaxy bias effects and, at the same time, maintains the nature of voids of being under-density regions in the total matter field.

The void finder algorithm exploited in this thesis uses flat-sky WL maps as input data, and follows the so-called *tunnel finding algorithm* adapted to this type of data using convergence peaks as tracers. The steps followed by the algorithm are the following:

- First it projects full-sky κ-maps onto 2D cartesian grids;
- Second, it identifies κ-peaks in the projected maps via a function of the *Lenstools* package[(3)] called *LocatePeaks*, providing the location of each κ-peak in the map as well as its amplitude. The found κ-peaks are the tracers of the lensing voids;
- Finally, the core part of the algorithm consists in the identification of the largest circles that are devoid of any κ-peak. These largest circles in the 2D maps correspond to tunnels of the tunnel algorithm applied to 3D maps. The tunnels are from a physical point of view elongated line-of-sight regions that intersect one or more under-dense regions of the space without passing through overdense regions (Cautun et al., 2018). If we project our full-sky maps on to a 2d Cartesian plane, tunnels will we circles devoid of tracers for the voids. The identification of these circles proceeds via a Delaunay tessellation: the vertices of the triangles constructed in the convergence maps are located in the position of the κ-peaks previously identified; by definition, the circumcircle of every Delaunay triangle does not contain any κ-peak. Therefore, each circumcircle is a void candidate, with its radius R being the candidate void radius R_V, and its center being the candidate void center (x_c, y_c).

It is interesting to compare the results obtained by (Davies et al., 2018) using the VOLEs finder with the results from other void finder techniques. In this way we are able to understand the main differences between the identified voids, and why weak lensing can be a prominent method for the cosmic void research field.

In Fig. 5.3 we can see both the κ-profiles and the γ-profiles of voids found with the VOLEs finder. The image on the right of Fig. 5.3 compares the γ-profiles obtained with the VOLEs finder to void profiles obtained via other void finders implemented in previous works, all of them working directly with matter density fields. They are:

(3) `https://lenstools.readthedocs.io/en/latest/`

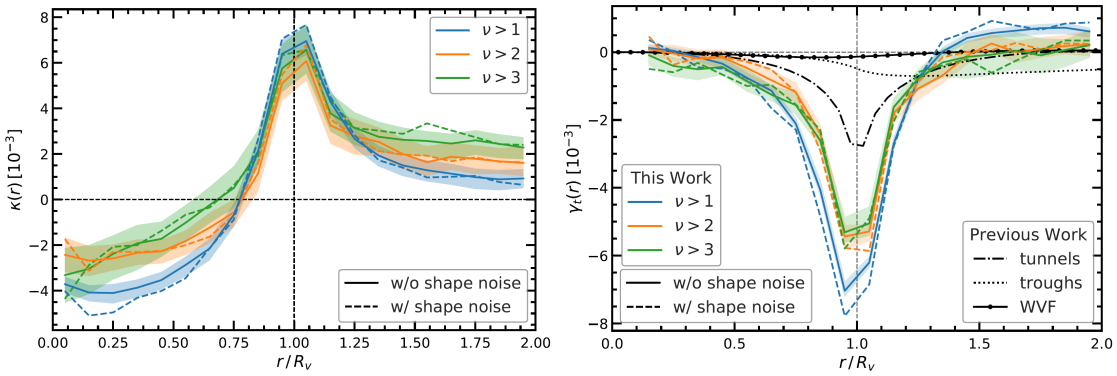

Figure 5.3: LEFT: Stacked κ-profiles of WL voids for different values ($\nu_{\rm cut} = 1, 2, 3$) of the Signal to Noise Ratio (SNR), $\nu \equiv \kappa/\sigma$, where σ is the standard deviation of the smoothed convergence maps. Lines with different colours show the average profile of voids in catalogs with galaxy shape noise (GSN) (solid lines) and without GSN (dashed lines). RIGHT: Stacked γ-profiles of WL voids for different values of the SNR. Lines with different colours show the average profile of voids in catalogs with GSN (solid lines) and without GSN (dashed lines). Other black lines correspond to the shear profile of under-densities identified other void finder strategies, as explained in the text (Davies et al., 2018).

- the 3D Watershed Void Finder (WVF) (Platen et al., 2007): voids are assumed to be simply basins in the large scale density field of matter or matter-tracers, with no a priori assumptions or constraints about their sizes, shapes or minimum value of the under-density. It proceeds via the construction of a Delaunay Tessellation Field Estimator as the tunnel algorithm adapted for voids of the density field, then it constructs a segmentation of the smoothed density field itself into watershed basins, and finally density minima are identified;

- the 2D throughs: 2d throughs have a definition very similar to 2d-tunnels; throughs are represented as elongated line-of-sight under-dense regions, however they have all the same radius and contain a low number of galaxies;

- 2D tunnels: in this case the procedure of void finding is very similar to the one used in this thesis but it has been applied to galaxy fields instead of lensing maps.

It is possible to see that in the case of voids found by the VOLEs finder the maximum value of the tangential shear is larger than the one found with the other algorithms. This is because the shear profile is obtained from lensing maps and, as we said before, the lensing signal is directly related to the total matter distribution along the line of sight.

5.4 From full-sky to flat-sky

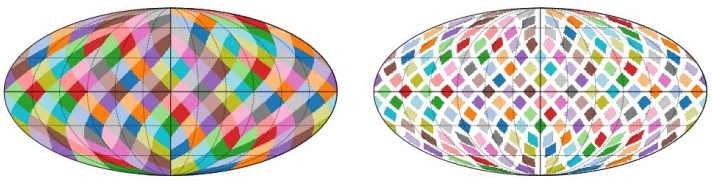

Figure 5.4: Procedure of partitioning full-sky maps into non-overlapping 10x10 deg^2 flat-sky square patches (Davies et al., 2019).

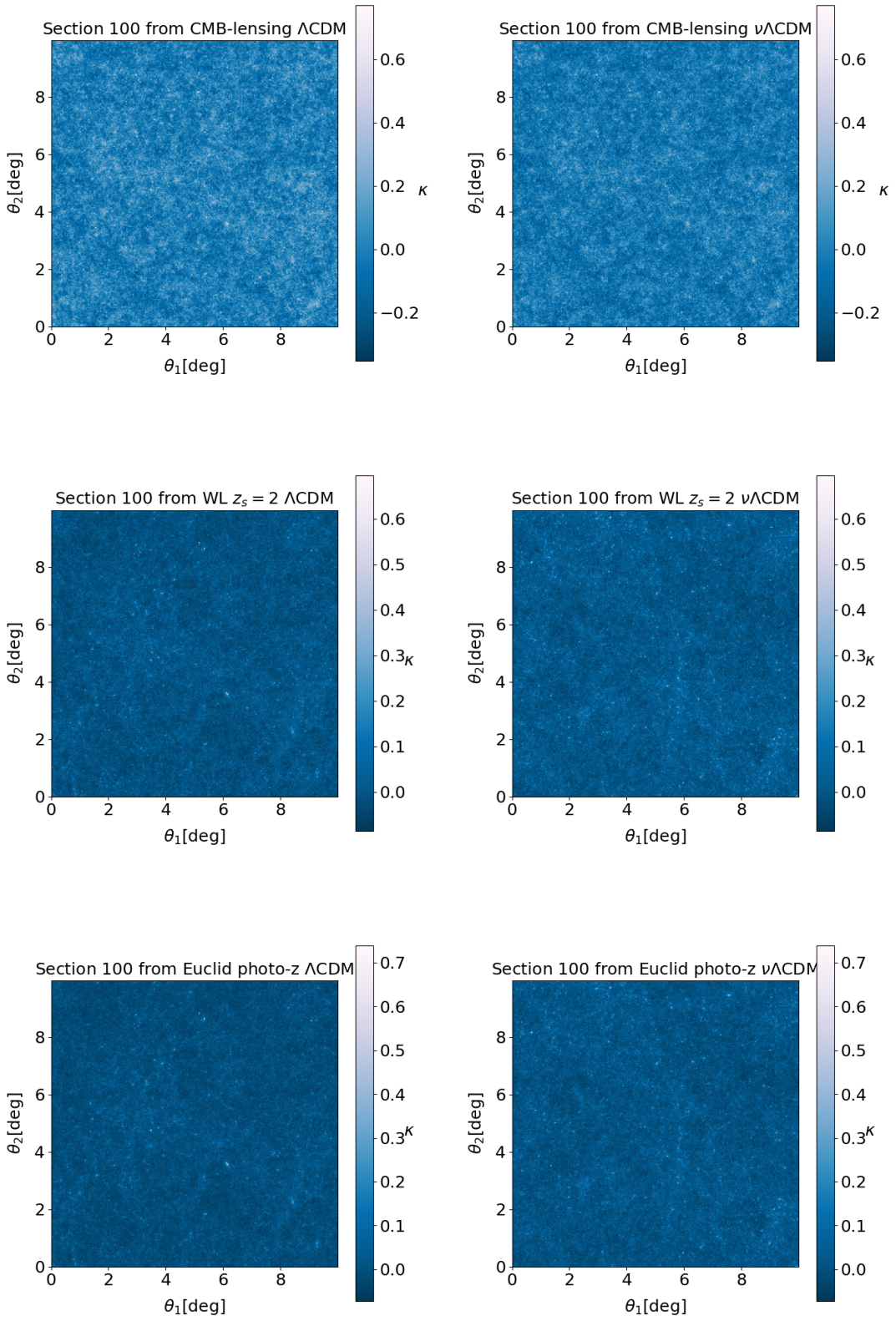

Figure 5.5: Flat-sky projections of convergence full-sky maps from the DEMNUni simulations, for different sources, both in the ΛCDM (left panels) and the $\nu\Lambda$CDM scenarios (right panels). The coordinates are in angular degrees.

The 2D tunnel-finding algorithm of VOLEs uses as input data lensing maps in the flat-sky approximation with a Cartesian pixelization. However, the ray-tracing Lens2Hat code, applied to the DEMNUni simulations, generates full-sky maps with the HEALPix pixelization. As a consequence, we need to perform a partitioning of the HEALPIx full-sky maps into smaller and non-overlapping Cartesian flat-sky maps, in order to be able to apply the VOLEs finder to our simulated data. The procedure is shown in Fig. 5.4. We choose to make the partitioning on $10\text{x}10\,\text{deg}^2$ flat-sky square patches.

To this aim, first a coarse HEALPix vector corresponding to $N_{\rm side} = 4$ is initialized. With this resolution the pixel area is $215\,\text{deg}^2$, and the total number of pixels $N_{\rm pix} = 192$. Next, the algorithm assigns each pixel in the full-sky simulated map to the coarser pixel it is enclosed by. In this way a low resolution map is generated with a number of pixel equal to 192, where each pixel is now the coarse pixel that contains the simulated data of the original map. Then a plane tangent at the center of each coarse pixel is defined, and a Cartesian projection of the data in the coarse pixel onto this tangent plane is performed. Finally, from such projections, flat square maps of $(10\text{x}10)\,\text{deg}^2$ are extracted, with their centers corresponding to the centers of the coarse pixels.

In Fig. 5.5 we show some examples of projected sections obtained from the simulated full-sky maps for the three lensing probes considered in this work: CMB-lensing, WL($z_{\rm s} = 2$), and weak lensing with a Euclid photometric redshift distribution. Contrary to the full-sky maps, here the visual inspection allows us to observe qualitative the effect of massive neutrinos on structure formation. In fact, the maps in the $\nu\Lambda$CDM scenario appear less bright than in the ΛCDM case, which means that perturbations in the κ field are smoother. This is confirmed also from the different κ-ranges in the color bars. Similarly, looking closely at the WL($z_{\rm s} = 2$) and Euclid lensing maps, in the massless neutrino case (left side) we can observe peaks larger and brighter than in the massive neutrino scenario (right).

5.5 Summary of Chapter 5

In this Chapter we have described the simulated data and the numerical procedures needed to perform the analyses presented in this thesis, i.e. pursue a detailed study of lensing voids in the massless and massive neutrino cosmological scenarios.

First of all, we have described the DEMNUni simulations and the Lens2Hat ray-tracing procedure providing the set of full-sky lensing maps, which are our raw data, i.e. the starting point of our void analysis. We also introduced HEALPix, the tool that allows us to easily handle such maps.

As a second step, we have explained the VOLEs finder procedure that we use in our analysis.

Third, we have shown how we move from full-sky maps with Healpix pixelization to flat-sky square patches with a 2D-Cartesian pixelization, thanks to the algorithm implemented by Davies et al. (2019).

Finally, we have shown some examples of full- and flat-sky maps for the three probes considered in this work: CMB-lensing, WL($z_{\rm s} = 2$), and Eulcid weak lensing, stressing the qualitative differences between the massless and massive neutrino cases, that we are able to infer from a first visual inspection of the maps.

Chapter 6

Lensing voids in the massless neutrino scenario

In this chapter we will focus on the analysis of simulated lensing voids in the massless neutrino case. We will study how the different probes considered in this work (CMB-lensing, weak lensing with sources at $z_s = 2$, and Euclid weak lensing) are sensitive to voids of different radius and depth. Furthermore, we will investigate the void redshift evolution. In fact, thanks to our simulated data, we are able to analyse the integrated lensing signal in redshift bins, and understand how κ-peak counts and void profiles evolve in redshift, with different behaviors depending on the considered probe.

6.1 The extraction of convergence peaks

We make use of different full-sky maps as input to our analysis in the ΛCDM cosmology. We consider maps of CMB-lensing, WL($z_s = 2$) maps, and Euclid convergence mock maps. After verifying that the algorithms presented in Chapter 5 work properly, we focus on the scientific exploitation of the produced lensing void catalogs.

Since one of our goals is the study of the void redshift evolution, we consider different redshift bins, and sum up together the full-sky CMB-lensing κ-maps described in Section 5.2. In this way we construct spherical shells around the observer with a thickness in redshift able to provide a fair sample of lensing voids in each redshift bin, and study how they evolve.

The considered redshift ranges are shown in Tab. 6.1. We will make the same choice in Chapter 7, in order to compare the void evolution between the massless and massive neutrino scenarios.

z_1	z_2	z_3	z_4	z_5	z_6
$19 < z < 99$	$12 < z < 15$	$5 < z < 11$	$2.5 < z < 4$	$1 < z < 2$	$0.5 < z < 1$

Table 6.1: Redshift bins chosen for the study of the void redshift evolution.

Convergence peaks are maxima of the lensing convergence, κ, field and in this analysis are used as tracers of local matter under-densities.

Before extracting the peaks, we proceed with the application of a Gaussian smoothing filter on each convergence maps. The peaks number and their spatial distribution are both affected by the smoothing scale we choose to apply, meaning that larger the smoothing scale is, larger is the number of low amplitude peaks washed out by the filter.

We apply a smoothing scale of θ_s=2.5 arcmin on the maps, that Davies et al. (2018) finds to be the optimal Gaussian filter able to suppress the galaxy shape noise without over-smoothing,

and we maintain the same filter throughout our analysis.

As mentioned before, convergence peaks are identified using a *Lenstools* function called *Locate Peaks* (Petri, 2016) that identifies in the maps perturbation in κ whose amplitudes are greater than their eight neighbours. These for us are the so-called κ-peaks.

Using this tool, for a given convergence map we produce several κ-peak catalogs by selecting different values of the threshold for the SNR, ν, defined as:

$$\nu \equiv \mathrm{SNR} \equiv \frac{\kappa}{\sigma}, \tag{6.1}$$

where σ is the standard deviation of the convergence map. In this work we will adopt the following thresholds: $\nu > \nu_{\rm cut} = 1, 2, 3$.

In Tab. 6.2 we report, for the massless neutrino case, the values of the mean standard deviation of the convergence for the three probes considered in this work, averaged over all the 192 projected flat-sky patches. As expected, given the same redshift range covered, its values for Euclid lensing and WL($z_{\rm s}$=2) are very similar, with a difference of $\sim 6\%$ between the two, while for CMB-lensing the mean convergence standard deviation is larger by $\sim 14\%$ with respect to the other probes at lower redshifts.

$\sigma_{\rm CMB}$	0.051
$\sigma_{\rm WL(z_s=2)}$	0.034
$\sigma_{\rm Euclid}$	0.032

Table 6.2: Mean standard deviation of the convergence for CMB-lensing, WL($z_{\rm s} = 2$), and Euclid weak lensing, in the ΛCDM scenario.

$\sigma_{\nu>1}$	0.0169
$\sigma_{\nu>2}$	0.0171
$\sigma_{\nu>3}$	0.0198

Table 6.3: Typical values of the convergence standard deviation for a 10x10 deg^2 map, in the WL($z_{\rm s} = 2$) case, for different SNR values, in the ΛCDM cosmology.

Moreover, in Tab. 6.3 we show, for the WL($z_{\rm s} = 2$) case, how the typical standard deviation of the lensing convergence increases with the value of ν. This is expected, as σ is a proxy of the κ-peak amplitude.

In Fig. 6.1 it is possible to observe how the peak selection criterion affects the number of peaks found in a convergence map, as we change the value of the threshold, $\nu_{\rm cut}$. As expected, we find less κ-peaks as we increase $\nu_{\rm cut}$. From a theoretical point of view, the projected density of κ-peaks as a function of the SNR is one of the most interesting feature to analyse in weak lensing maps. Therefore, we first focus on the analysis of the number of κ-peaks in the CMB-lensing, WL($z_{\rm s} = 2$) and Euclid weak lensing simulated maps, where the photometric redshift distribution, $n(z)$, of lensed galaxies is represented in Fig. 6.2, and given by

$$n(z) \propto \left(\frac{z}{z_0}\right)^2 \exp\left[-\left(\frac{z}{z_0}\right)^{3/2}\right]. \tag{6.2}$$

Here $z_0 = z_m/\sqrt{2}$, with $z_m = 0.9$ being the median redshift. The grey area in Fig. 6.2 shows the redshift range covered by the photometric Euclid survey.

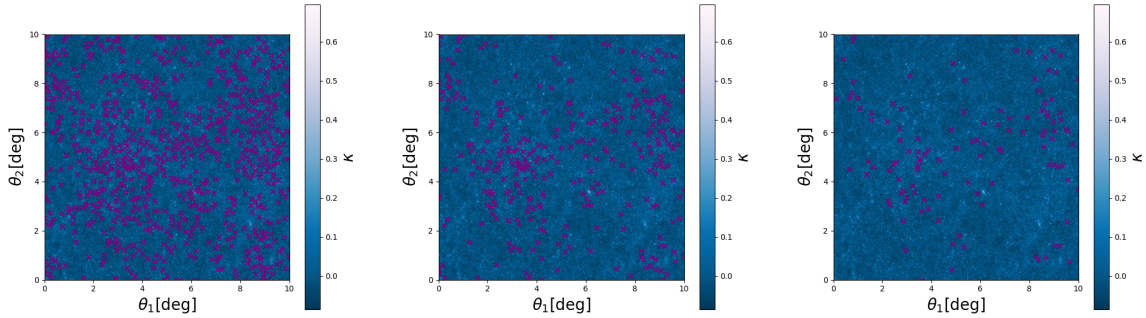

Figure 6.1: Distributions of κ-peaks with different heights (purple crosses) in a the same convergence map. Peaks with amplitudes below the value of $\nu_{\rm cut} = 1, 2, 3$ are removed in the left, middle, and right panels, respectively, in the ΛCDM case. The axes are the θ_1 and θ_2 orthogonal directions. The smoothing scale applied to the maps is θ_s=2.5 arcmin.

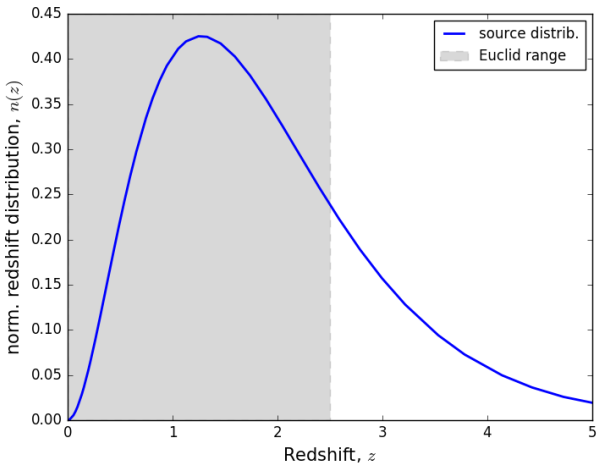

Figure 6.2: Galaxy redshift distribution used for the Euclid mock convergence maps used in this work. The grey area is the redshift range covered by Euclid (Laureijs et al., 2011).

The effective convergence map created with this source distribution and used in this thesis has been computed via the theoretical procedure described in Bartelmann and Schneider (2001).

The first results of our analysis on the convergence maps for the three probes considered are shown in Fig. 6.3, in the ΛCDM scenario. We report the mean cumulative κ-peak abundances for $n(> \nu)$ per unit area, that is the number densities of κ-peaks with SNR greater than $\nu = \kappa/\sigma$, as a function of ν. It is possible to observe that all the analysed probes show the expected behaviour: as ν decreases, $n(> \nu)$ rapidly increases, telling us that κ-peaks with lower heights are more abundant as expected.

Moreover, from Fig. 6.3 we can observe that the weak lensing map with $z_{\rm s} = 2$, along with the Euclid one, present higher peaks with respect to the CMB-lensing map, the difference reaching even one order of magnitude for large ν values. In addition, while CMB-lensing does not present κ-peaks with SNR above $\nu = \kappa/\sigma \sim 5.0$, the other two probes extend up to $\nu \sim 8$ (for WL with $z_{\rm s} = 2$) and $\nu \sim 10.0$ (for Euclid lensing), with a difference between the latter up to a factor of ~ 2. Somehow this behaviour is expected since weak lensing at low redshifts is much more affected by

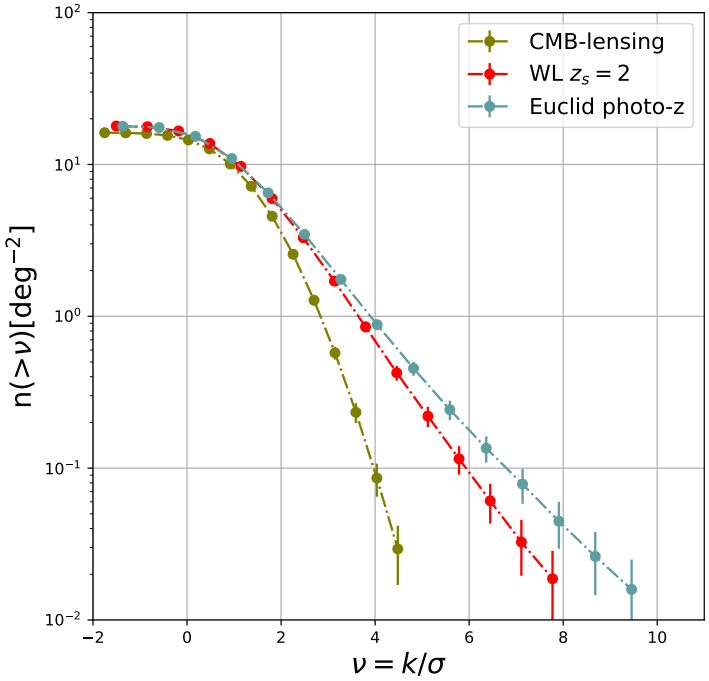

Figure 6.3: Cumulative projected projected density of κ-peaks averaged over 192, 10x10 deg^2, maps, as a function of the SNR, ν, for the three probes considered in this work, assuming a ΛCDM cosmology. Error bars show the Poisson error.

the nonlinear structure evolution than CMB-lensing: the latter is characterized by a convergence kernel peaked at $z \sim 2$, where linear structure formation is still important, while the former have a kernel peaked at $z \sim 0.5$ where the nonlinear growth of cosmic structures is dominant.

Finally, let us notice that there exit negative SNR values down to $\nu = \kappa/\sigma = -2$. For such values the κ-peak number densities converge to the same values as expected. In fact, κ-peaks are local maxima in the convergence field, so there exist certainly many of them with SNR larger than a negative value, independently of the particular probe considered. As we can observe from Fig. 6.3, the variation of the peak number densities vanishes for negative values of ν, therefore we can infer that positive κ-peaks dominate, and negative ones (considered as local maxima inside under-dense regions) are very rare.

After discussing the κ-peak abundance of the total maps, we now focus on its redshift evolution. To this aim, we consider the different redshift bins defined in Tab. 6.1 for the CMB-lensing case. These slices of convergence maps represent different lens regions along the light-cone from the observer back to the last scattering surface. Tab. 6.4 shows the convergence standard deviations, σ_z, associated to such maps, averaged over 192, 10x10 deg^2, flat-sky patches. We see that σ_z increases with decreasing redshift, due to the nonlinear structure evolution.

In Fig. 6.4 we show the corresponding mean cumulative projected densities of κ-peaks. As before, all the curves present the characteristic decreasing behaviour as the SNR, ν, increases. Moreover, not only the κ-peak projected density hugely increases with decreasing redshift, but it also extends up much larger values of ν. In fact, at e.g. $\nu \sim 4$, it changes from $n(>\nu) \sim 3 \cdot 10^{-2}$, in the bin $19 < z < 99$, up to $n(>\nu) \sim 1$ in $0.5 < z < 1$, i.e. by a factor of ~ 30. In addition, the cumulative projected density extends by a factor of ~ 2 toward higher SNR values. Such increases arise especially when the nonlinear structure formation starts to become dominand, i.e.

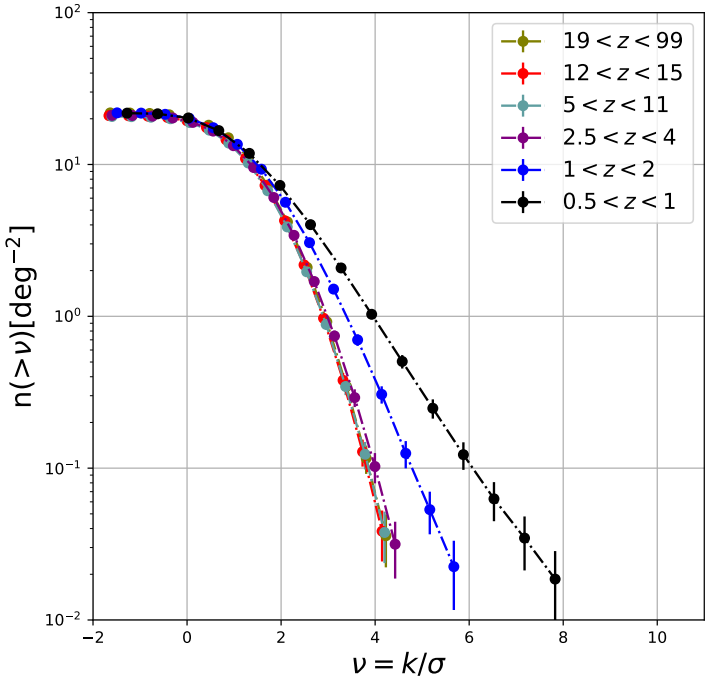

Figure 6.4: Cumulative projected density of κ-peaks as a function of the SNR $\nu = \kappa/\sigma$, in different redshift bins, averaged on the 192 10x10 deg^2 patches in the CMB-lensing case, as extracted via our ray-tracing procedure in the ΛCDM cosmology. Error bars show the Poisson error.

$19 < z < 99$	$12 < z < 15$	$5 < z < 11$	$2.5 < z < 4$	$1 < z < 2$	$0.5 < z < 1$
σ_{z_1}	σ_{z_2}	σ_{z_3}	σ_{z_4}	σ_{z_5}	σ_{z_6}
0.0041	0.0038	0.0041	0.0059	0.0062	0.0060

Table 6.4: Mean values of the standard deviation associated to the simulated CMB-lensing maps for different redshift ranges, as extracted from our ray-tracing procedure in the ΛCDM case.

at $z < 1$, as it is evident from Fig. 6.4. Again this is expected, as nonlinear structure evolution produces more and higher κ-peaks as redshift decreases.

6.2 Void identification and counts

The next step in the analysis is the identification of voids in the κ maps. It proceeds via the algorithm called tunnel finding (Cautun et al., 2018), as explained in Chapter 5, adapted to search for voids in lensing convergence maps. The tunnel finding algorithm identifies voids in the projected distribution of galaxies that does not contain any galaxy, similarly its modified version uses convergence peaks as tracers and it defines a void as the region of the convergence map that does not contain any κ-peak. Clearly it is a very idealised situation since it considers not only perfectly spherical voids, but also voids that do not contain any κ-peak in their inside.

In Fig. 6.5 we provide a visualisation of the spherical voids found for our three probes in the massless case: the lensing map with sources located at $z_s = 2$, the CMB-lensing map, and the map with the Euclid photometric redshift distribution. In particular, the three horizontal panels show

how the number of voids changes as we increase the SNR selection criterion. The dependence of

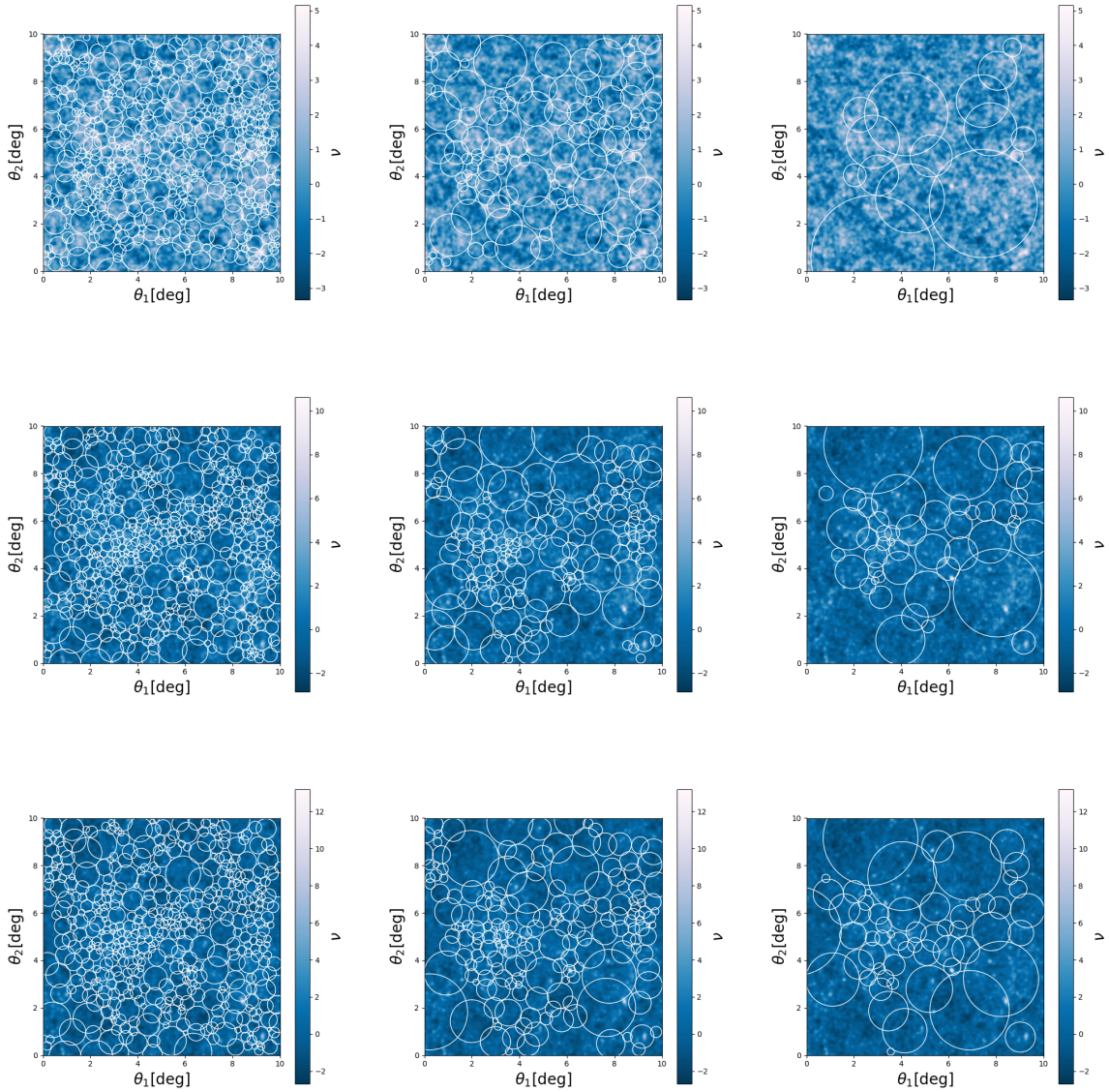

Figure 6.5: Visualisation of voids found in one of square projected sections fro CMB-lensing (TOP), WL($z = 2$) (MIDDLE), and Euclid weak lensing (BOTTOM) in the ΛCDM scenario. The three images show the voids found for three convergence peak selection criteria: $\nu > 1$ (LEFT), $\nu > 2$ (MIDDLE) and $\nu > 3$ (RIGHT). In the background we show the SNR, $\nu = \kappa/\sigma$.

void size from the peak selection criterion is clearly visible: as ν increases, also the void radius R_V increases. This means that, imposing a higher signal to noise ratio, $\nu = \kappa/\sigma$, the tunnel algorithm identifies voids with larger radii. This is expected since, as the threshold $\nu_{\rm cut}$ increases, the void finder looks for higher κ-peaks, which are also rarer (with lower density) than peaks exceeding a lower threshold. Therefore, since voids are defined as regions devoid of κ-peaks, larger $\nu_{\rm cut}$, i.e. rarer peaks, corresponds to larger void radii.

In Fig. 6.5 we can actually observe such behavior: the left panel, representing the case with $\nu > 1$, has a very large number of small circular voids which are the regions devoid of κ-peaks with $\nu > 1$ as shown in the left panel of Fig. 6.1. This is the case where we can find the smallest lensing voids. In the middle panel of Fig. 6.5, corresponding to SNR>2, the number of voids

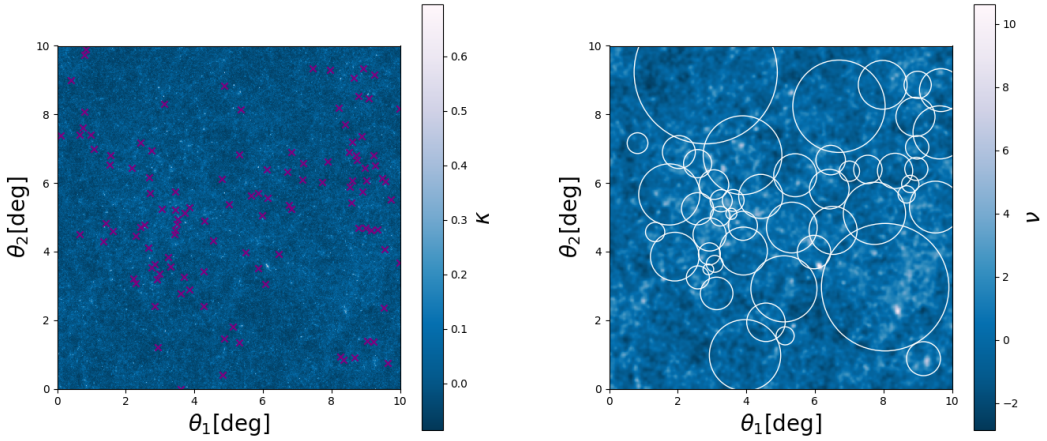

Figure 6.6: Visual comparison between the κ-peak distribution for SNR>3 and the void distribution identified by the VOLEs finder in a typical 10x10 deg^2 convergence patch for WL($z_s = 2$), in the ΛCDM case.

decreases and their radii R_V increase. However, we can still observe lensing voids with small radii as κ-peaks with SNR>2 are not so rare. Finally, the right panel show the number of voids identified for SNR>3.

Also in this case we find a very good correspondence between the κ-peak distribution and the size and distribution of voids, as it is clear from a visual inspection of the left and right panels in Fig. 6.6 for the WL($z_s = 2$) case.

For what concerns the differences between the three probes, as expected, the WL($z_s = 2$) and Euclid lensing patches show a similar void distribution, while the CMB-lensing patch is characterized by a smaller number of voids, especially for the catalog $\nu > 3$, typically with larger values of R_V. This is due to the fact that the CMB-lensing probe is the most linear between the three and it has a smaller number of lensing peaks, as shown in Fig. 6.3, as compared to the other two probes.

It is interesting to analyse more quantitatively how the total number of voids changes with the source redshift, and as a function of the three thresholds $\nu > 1$, $\nu > 2$ and $\nu > 3$.

In Fig. 6.7 we show the histograms of the total number of lensing voids as a function of their radius R_V in the case of the CMB-lensing map, the WL map with sources located at redshift $z_s = 2$, and the convergence map with a Euclid source distribution. These are extracted combining together the 192 10x10 deg^2 square patches for each of the three lensing probes, with different SNR thresholds.

In particular, for the three thresholds, we report the total number of voids, N_V in Tab. 6.5:

From Tab. 6.5 it is possible to observe that, the CMB-lensing catalogs have the smallest number of voids among the three probes considered, and that such difference increases with the threshold ν, starting from comparable numbers for $\nu > 1$, and ending with differences by factors of $\sim 3 - 6$ for $\nu > 3$. This is a further confirmation tha CMB-lensing probes a more linear evolution with respect to the low redshift probes, not only for what concerns peaks in the convergence field, but also for voids: more linear the structure evolution is, lower the number of voids is. Interestingly, for $\nu > 3$, the Euclid-lensing catalog presents a total number of voids larger by a factor ~ 1.5 with respect to the WL($z_s = 2$) catalog, meaning that a realistic source redshift distribution is more sensitive to the non linear structure evolution. This result agrees with the

	$N^{\max}_{\mathrm{V,CMB}}$	$N^{\max}_{\mathrm{V},z_s=2}$	$N^{\max}_{\mathrm{V,Euclid}}$
$\nu > 1$	21775	26558	24427
$\nu > 2$	3772	6213	6146
$\nu > 3$	379	1380	2150

Table 6.5: Total number of lensing voids for CMB-lensing, WL($z_s = 2$), and Euclid lensing catalogs, in the case of $\nu > 1$, $\nu > 2$ and $\nu > 3$ for the ΛCDM scenario.

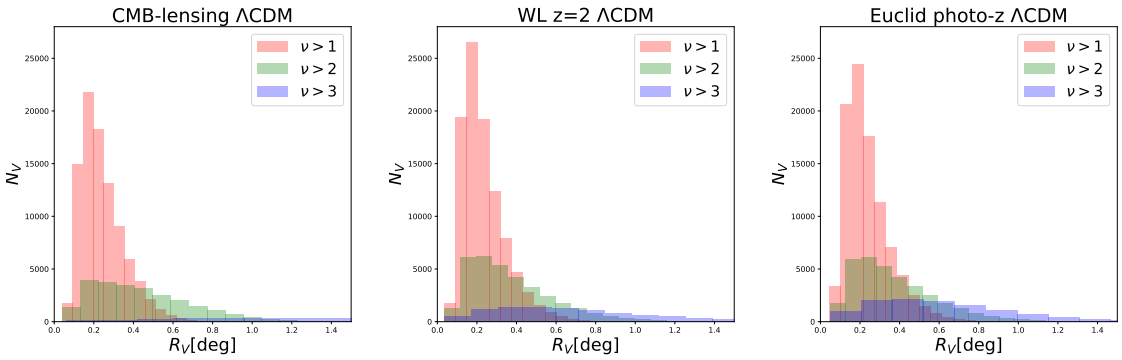

Figure 6.7: Histograms of the total number of voids, summed over the 10x10 deg^2 patches, as a function of their radii R_V for different SNR values ($\nu > 1$ in red, $\nu > 2$ in olive and $\nu > 3$ in blue), and different probes: CMB-lensing (LEFT) WL($z_s = 2$) (MIDDLE) and Euclid lensing (RIGHT), in the ΛCDM cosmology.

cumulative projected density of peaks in Fig. 6.3, and is also confirmed from the histograms of the void total number in Fig. 6.7.

The cumulative void projected density as a function of the void radius, R_V, shown in Fig. 6.8 confirms such trend. First, small voids, e.g. $R_V < 0.5$ deg, always dominate in density with respect to larger ones. However, as we increase the SNR thresholds, $\nu > 2$ and $\nu > 3$, we can observe that, voids start to extend to larger radii, up to $R_V = 3.5$ deg for the CMB-lensing case. Voids in CMB-lensing catalogs extend to larger radii with respect to weak lensing probes at low redshifts. This can be understood again in terms of the particular structure evolution which the different probes are sensitive to. Since for WL($z_s = 2$) and Euclid lensing nonlinear structure formation dominates, especially for higher SNR threshold, there will be more κ-peaks than in CMB-lensing maps, and therefore (for the same sky area) there will be more but smaller regions devoid of κ-peaks in the former with respect to the latter. This trend with the imposed SNR threshold is expected and there is concordance with what we see qualitatively in Fig. 6.5.

Second, it can be interesting to notice that for small radii the curves corresponding to catalogs with $\nu > 1$ and $\nu > 2$ of the three probes mostly overlap, in particular for the Euclid lensing map and the WL($z_s = 2$) map, given their same redshift coverage. This is because we have learned that the void size is strictly linked to the κ-peak density, and in fact the number densities of κ-peaks, for $\nu < 3$, are very similar for the three probes. They begin to separate one from the other just for $\nu \gtrsim 2$, as shown in Fig. 6.3. Consequently, from Fig. 6.8, we can observe that, for $\nu > 3$, also the void densities of the three probes start to separate one from the other, extending to larger radii. This separation is smaller between the Euclid lensing and the WL($z_s = 2$) void catalogs, as they trace a very similar structure distribution in the Universe. But the CMB-lensing void catalog, probing different stages of structure evolution, looks quite different from the other two: at small radii the CMB-lensing map has a projected density of voids a factor of ~ 3 smaller than the other two probes, implying a lower number of smaller voids enclosed by high significant κ-peaks.

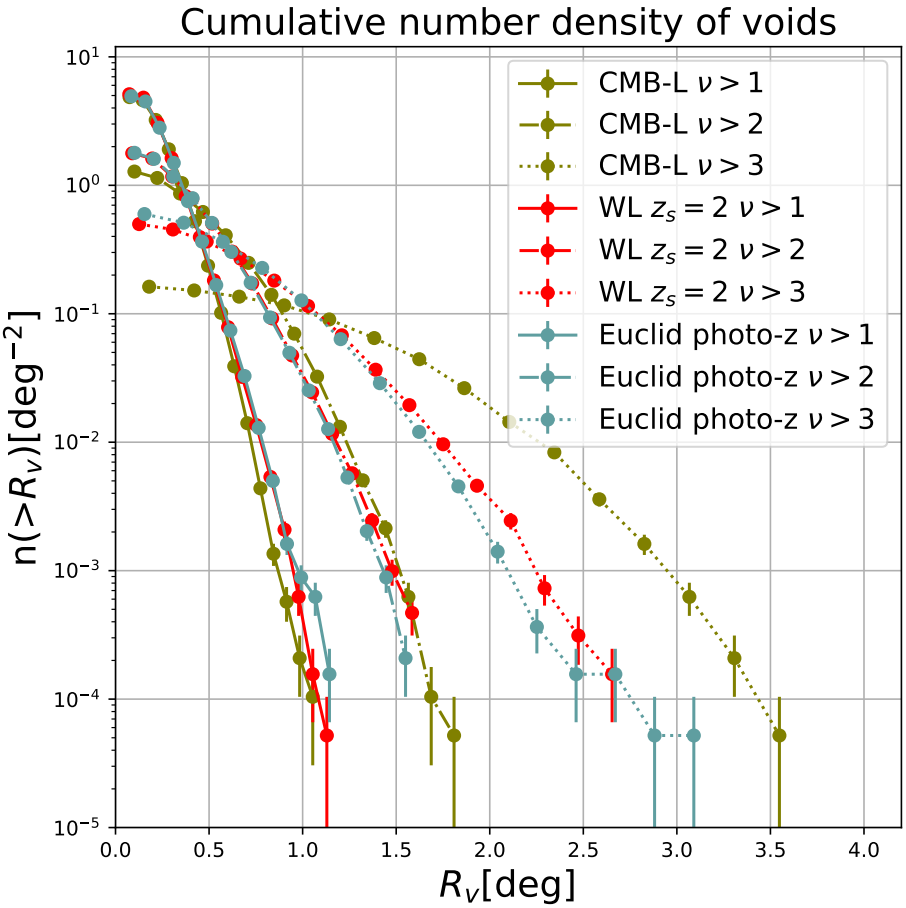

Figure 6.8: Cumulative projected density of voids as a function of the void radius R_V for CMB-lensing (olive), WL(z_s = 2) (red), and Euclid lensing (blue), in the ΛCDM cosmology. Each curve is averaged over all the 192 10x10 deg^2 patches. The curves represent three different void catalogs created starting from κ-maps where three different SNR thresholds are applied: $\nu > 1$ (solid), $\nu > 2$ (dash-dotted) and $\nu > 3$ (dotted). The smoothing scale applied to all the three maps is θ_s=2.5 arcmin. Each curve is averaged over all the 192 10x10 deg^2 patches. Error bars show the Poisson error.

This behavior reverses at large R_V, where among the three probes the CMB-lensing map has the largest projected density of voids enclosed by high significant κ-peaks with $\nu > 3$. This difference is more than one order of magnitude. We think that such behavior of CMB-lensing voids for $\nu > 3$ is understandable inspecting again at the projected density of κ-peaks in Fig. 6.3. In fact, for $\nu > 3$ the CMB-lensing curve decreases much more steeply than the other two, becoming one order of magnitude smaller than for low redshift probes for $\nu \gtrsim 4$, and then negligible. In other words, in the CMB-lensing convergence maps peaks with $\nu > 3$ are spatially very rare, with respect the other two probes, and therefore the VOLEs finder, which identifies void as empty regions, at a fixed large radius, finds much more voids in the CMB-lensing κ-maps than in the WL(z_s = 2) and Euclid maps. In some sense, given the void definition in the VOLEs finder, void catalogs behaves as the "negative image" of κ-peak catalogs.

This is confirmed if we have a look at the void distribution in the third column of Fig 6.5, where the number of large voids seems to dominate in the CMB-lensing catalog with respect to the other two. Further investigation on this behavior will be performed in the next future.

Now, we want to carry a similar analysis on the CMB-lensing lens shells in different redshift

z_i	$N_{\rm V}^{\nu>1}$	$N_{\rm V}^{\nu>2}$	$N_{\rm V}^{\nu>3}$
19<z<99	27832	6716	402
12<z<15	32066	6451	378
5<z<11	27566	4095	359
2.5<z<4	28914	8048	508
1<z<2	29316	7008	1088
0.5<z<1	26528	8379	2206

Table 6.6: Total number of voids $N_{\rm V}$ for CMB-lensing, as a function of redshift and κ-SNR threshold, obtained by combining together the 192 10x10 deg^2 patches, in the ΛCDM cosmology.

bins, as defined in Tab. 6.1. This will allow us to study the redshift evolution of the lensing void projected density as a function of the radius, $R_{\rm V}$.

Fig. 6.9 shows the histograms of the total number, $N_{\rm V}$, of CMB-lensing voids as a function of $R_{\rm V}$, for different redshift bins; as usual, we analyse the three void catalogs with the κ-peak SNR $\nu > 1$, $\nu > 2$ and $\nu > 3$.

For completeness, the the total number of voids, $N_{\rm V}$ in each redshift bin, for the void catalogs with $\nu > 1$, $\nu > 2$ and $\nu > 3$, are reported in Tab. 6.6. We can observe that, as the imposed value of the threshold on the SNR increases, the number of lensing voids decreases. This can be related to the fact that the algorithm of void finding identifies a mach lower number of convergence peaks when we impose higher $nu_{\rm cut}$ in our data. Since we use these convergence peaks as tracer for the identification of the under-densities in the κ-maps, we therefore find less numerous lensing voids. Moreover, as the redshift decreases, the lensing voids associated to catalogs with $\nu > 2$ and $\nu > 3$ become more numerous. The redshift range $19 < z < 99$ has a number of lensing voids $N_{\rm V}^{\rm nu>2} = 6716$ and $N_{\rm V}^{\rm nu>2} = 402$, however, when we consider lower redshift values as, for example, the bin $0.5 < z < 1$, it is characterized by $N_{\rm V}^{\rm nu>2} = 8379$ and $N_{\rm V}^{\rm nu>3} = 2206$. This clearly highlights how the formation of voids increases as the Universe evolves. Finally, from Fig. 6.9 and Tab. 6.6 we see that in the CMB-lensing catalogs the presence of voids devoid of κ-peaks with SNR>3 starts to increase and become non negligible, as compared to the other thresholds, only at redshifts $z < 1$, when the nonlinear evolution starts to dominate. Again this can be associated to the evolution of the projected peak density shown in From Fig. 6.4: thanks to the nonlinear structure evolution, only for $z < 1$ the peak projected density extends appreciably above $\nu > 3$, so that regions devoid of peaks with such SNR can be found in a non negligible amount only for $z < 1$.

In Fig. 6.10 we show the projected void cumulative number densities as a function of the void radius. For different redshifts, all the plots show the usual decreasing behaviour with the increasing threshold: catalogs with $\nu > 2$ and $\nu > 3$ seem to have much more larger voids than catalogs with $\nu > 1$. This confirms what we have already seen from the plot of the cumulative projected density of κ-peaks as a function of the SNR: high SNR peaks correspond to massive structures or more structures aligned along the line of sight that is a rare event; thus, the number of peaks decreases with the threshold as well as the number of voids for each catalog. At the same time if we increase the $R_{\rm V}$ values, the number of voids with that radius decreases. This means that for each catalog and for each redshit range, we find much more voids with smaller radii than voids with larger ones. This for each fixed redshift bin. However, if we compare different redshift bins together, in order to understand the evolution of the void projected density and size for different thresholds, on the one hand we notice that for the $\nu > 3$ void catalog, lower redshifts have a larger density of very small voids. The same is true for the catalog with $\nu > 2$, although it is less evident. For $\nu > 2$ he void density peak changes from $n(> R_{\rm V}) \sim 0.2[deg^{-2}]$ at $19 < z < 99$ to $n(> R_{\rm V}) \sim 0.8[deg^{-2}]$ at $0.5 < z < 1$. This is expected if we think that lensing maps at lower redshift are more affected by the evolution of nonlinear structures.

On the other hand we notice the opposite behaviour for very large voids. In fact, in perfect agreement with the redshift evolution of the peak density in Fig. 6.4, we can observe that as $n(\nu > 3)$ increases from high to low redshifts due to nonlinear evolution, the void density decreases and extends down to lower R_V values. Such differences can reach even some orders of magnitude if compared between the highest and the lowest redshift bins, depending on the value of large radii considered. Again, we can say that the void distribution is the "negative image" of the κ-peak distribution, therefore larger the number of κ-peak with SNR>3 is at low redshifts (because of nonlinear evolution), smaller is the size of void devoid of such peaks. And, smaller the number of κ-peaks with SNR>3 is at high redshift (since linear evolution is still dominating) larger is the size of voids devoid of such peaks.

6.3 The convergence profile inside voids

Now that we have analysed the projected density of voids as a function of their radius, and how it changes with SNR threshold and redshift, for the three different probes considered in this work, we can now study their convergence and shear profiles.

Following previous works on the analysis of voids from lensing maps such as (Davies et al., 2018), we calculate the convergence profiles of lensing voids by using annuli of thickness R_V/N_{bin} with R_V being the radius of the lensing voids of our flat-sky patches and $N_{bin} = 15$ being the number of bins that we find to be the best one to analyse our data. We stack all the voids from each of the 192 flat-sky patches, and plot the κ-profiles as a function of their scaled radial distance R/R_V. Then, we average over our 192 patches in order to have better statistics.

First, we focus on the convergence void profiles, for the CMB-lensing catalog, the WL($z_s = 2$) catalog, and Euclid lensing catalog. Fig. 6.11 shows the obtained stacked convergence void profiles.

All the profiles are plotted up to the radius $R = 1.86R_V$ because we are interested in showing and checking that for larger values of the radial distance R/R_V these curves converge to the background value of κ, i.e. its mean that we have set to be zero.

In all three cases it is possible to observe that for $R < 0.75R_V$ we have negative convergence values, this points out that voids are truly under-dense regions in the κ-maps within their profile. Moreover what we see is that catalogs with $\nu > 3$ show interestingly to be less under-dense on average than for the other thresholds, and are characterized by the smallest depth at R=0; this particular behaviour is expected because, as we increase the SNR value of κ-peaks tracing the void profile, we increase also the sizes of voids we find in that particular region. The fact is that these larger voids may contain κ-peaks with $\nu < 3$, leading to less under-dense voids.

On the contrary, at larger values of R/R_V we see a common decreasing behaviour in absolute value of the κ-profile curves; they behave similarly to one another, all going toward the background value of zero.

The maximum, the so-called "wall", is reached for all curves at $R = R_V$ as expected; however the amplitude of the walls are slightly different depending on which lensing probe we are considering, and at which catalog we are referring to in terms of the threshold ν. The same is true for the void depth at $R = 0$. In particular, for higher SNR values both the depth and the wall high decrease as the threshold ν increases, independently of the kind of probe considered.

In fact, for $\nu > 1$, the lensing map with Euclid redshift distribution shows a maximum κ-value at the wall much similar to the one of the WL $z_s = 2$: $\kappa_{max}^{Euclid} = 0.0019$ and $\kappa_{max}^{z_s=2} = 0.0022$, while $\kappa_{max}^{CMB} = 0.0061$; at the same time it contains the least under-dense voids with respect to CMB-lensing and WL at $z_s = 2$: $\kappa_{min}^{Euclid} = -0.0071$ and $\kappa_{min}^{z_s=2} = -0.0083$, while $\kappa_{min}^{CMB} = -0.0272$. We observe a similar trend among the three probes also for $\nu > 2, 3$.

We see that the CMB-lensing map has both the largest absolute values of κ_{min} and κ_{max}, which differs by one order of magnitude from the other two probes. Therefore it seems that CMB-lensing, being integrated up to larger redshifts with respect to the other two probes, traces voids

with the largest fluctuations in κ, which in turns means deepest voids.

In order to quantitatively show the main differences between $\kappa_{\rm max}$, the value of the convergence κ on the wall, and $\kappa_{\rm min}$, the value of the convergence κ at the maximum depth of the lensing void, for the three probes and three peak SNR threshold, we report these values in Tab. 6.7.

	$\kappa_{\rm max}^{\rm CMB}$	$\kappa_{\rm max}^{\rm WL(z_s=2)}$	$\kappa_{\rm max}^{\rm Euclid}$	$\kappa_{\rm min}^{\rm CMB}$	$\kappa_{\rm min}^{\rm WL(z_s=2)}$	$\kappa_{\rm min}^{\rm Euclid}$
$\nu > 1$	0.0061	0.0022	0.0019	-0.0272	-0.0083	-0.0071
$\nu > 2$	0.0050	0.0018	0.0017	-0.0168	-0.0057	-0.0051
$\nu > 3$	0.0027	0.0013	0.0013	-0.0067	-0.0040	-0.0035

Table 6.7: Maximum $k_{\rm max}$ and minimum $k_{\rm min}$ of the stacked void profiles traced by the three probes considered in this work, for the κ-SNR thresholds $\nu > 1$, $\nu > 2$ and $\nu > 3$, in the ΛCDM cosmology.

Moreover, from Fig. 6.11 we notice one common property for all three κ-profiles: as we follow the void profile from $R = R_{\rm V}$ down to its center $R = 0$, the corresponding convergence values decrease as well, showing a particular concavity. The convergence profiles of our probes have a finite value of κ at the maximum depth of the stacked voids, however the behaviour of the curves is not flat. If we extrapolate their asymptotic trend it seems that our voids have not a fixed *basin*, since they look concave rather than convex. These results are very different from the ones obtained in Davies et al. (2018), which find void convex void profile. We believe that this characteristic profile could be due to the native resolution of the full-sky lensing maps we have analysed in this work. Even if a full-sky resolution of $N_{\rm side} = 4096$ is extremely large, when projected to 10x10 deg^2 patches, it translates into a lower resolution when compared to the one usually adopted in flat-sky analyses. This means that we smooth out small scale structures with respect to the latter case, which is e.g. considered in Davies et al. (2018). In fact, works in preparation (Vielzeuf et al. 2021, in prep.), that cross-correlate our same set of simulated CMB-lensing maps with void catalogs obtained applying the 2D void finder from Sánchez et al. (2017); Vielzeuf et al. (2019) directly to the DM halo light-cones constructed from the DEMNUni simulations, show that CMB-lensing void profiles start to become convex as the smoothing scale in the void-finder is decreased. This could also explain the fact that the profile concavity gets slightly mitigated when we consider voids with SNR>3 thresholds, as in this case the smoothing effect of the size of the HEALPix pixels has a lower impact on larger κ-peaks than on lower ones. We have performed further checks on the κ-profiles of the CMB-lensing map and the WL map($z_{\rm s} = 2$) in the ΛCDM cosmology that are shown in Appendix A.

Now, we want analyze how the void converge profile evolves in redshift. We show these results in Fig. 6.12.

From Fig. 6.12 we recover that the curves show all the usual expected behaviour: convergence values increase with $R/R_{\rm V}$, they reach the maximum at $R = R_{\rm V}$ and then decrease rapidly toward the zero, that is the background value. Beside that, also in the case of summed lensing maps at different redshift ranges, the curves show a negative concavity as R approaches the zero value, concavity that tends to flatten, again, when we consider the void catalogs with higher SNR.

All the panels in Fig. 6.12 help us understand how the convergence void profiles change with the redshift.

In particular, it is possible to see that, as the redshift ranges decrease they seem to be more and more under-dense (i.e. there are much less structures on their inside), this is valid for all the catalogs; in fact the value of $\kappa_{\rm min}$ decreases by about 23% for $\nu > 1$ from the highest to the lowest redshift bin. At the same time, we find that the walls on the boundary of the basins seem to be richer in structures (i.e. the density increases) and, as a consequence, they show higher values of $\kappa_{\rm max}(r)$ with a percent variation of $\sim$ 40% for $\nu > 1$ from the highest to the lowest redshift bin. Evidently we are tracing, for the first time in the literature, the evolution of the lensing void profiles, observing how less devoid regions become more and more devoid of matter perturbations

inside their profile as the Universe evolves. At the same time, from Fig. 6.10, we observe that the projected density of smaller voids increases (independently of the SNR threshold) as the redshift decreases. Looking at the underdensity contrast in absolute value, this is similar to what happen to DM halos in mass: as the Universe evolves more and more massive DM haloes form.

The values of $\kappa_{\rm max}$ and $\kappa_{\rm min}$ are shown in Tab. 6.8 and Tab. 6.9.

	$\kappa_{\rm max}^{z_1}$	$\kappa_{\rm max}^{z_2}$	$\kappa_{\rm max}^{z_3}$	$\kappa_{\rm max}^{z_4}$	$\kappa_{\rm max}^{z_5}$	$\kappa_{\rm max}^{z_6}$
$\nu > 1$	0.0006	0.0005	0.0006	0.0008	0.0010	0.0010
$\nu > 2$	0.0004	0.0003	0.0004	0.0005	0.0007	0.0007
$\nu > 3$	0.0001	0.0001	0.0001	0.0002	0.0003	0.0004

Table 6.8: Maximum $\kappa_{\rm max}$ of the stacked void profiles for the CMB-lensing void catalogs for different redshifts and thresholds $\nu > 1$, $\nu > 2$ and $\nu > 3$, in the ΛCDM cosmology.

	$\kappa_{\rm min}^{z_1}$	$\kappa_{\rm min}^{z_2}$	$\kappa_{\rm min}^{z_3}$	$\kappa_{\rm min}^{z_4}$	$\kappa_{\rm min}^{z_5}$	$\kappa_{\rm min}^{z_6}$
$\nu > 1$	-0.0023	-0.0019	-0.0024	-0.0032	-0.0036	-0.0030
$\nu > 2$	-0.0010	-0.0009	-0.0011	-0.0016	-0.0018	-0.0017
$\nu > 3$	-0.0002	-0.0002	-0.0004	-0.0005	-0.0008	-0.0008

Table 6.9: Minimum $\kappa_{\rm min}$ of the stacked void profiles for the CMB-lensing void catalogs for different redshifts and thresholds $\nu > 1$, $\nu > 2$ and $\nu > 3$, in the ΛCDM cosmology.

6.4 The shear profile inside voids

We have shown in the previous section the κ-profiles of stacked lensing voids for different probes in the ΛCDM cosmology, and we have analyzed their evolution with redshift. The last step in our analysis is the study of the tangential shear profiles of the same lensing voids both for different probes and for different redshift ranges. We focus in this section on the ΛCDM cosmology, in the next Chapter we will include also the effects of massive neutrinos.

We calculate the tangential shear profile of voids, $\gamma_{\rm t}(r)$, from the convergence profile using Eq. (6.3) (Davies et al., 2018):

$$\gamma_{\rm t}(r) = \bar{\kappa}(< r) - \kappa(r)\,, \tag{6.3}$$

where $\kappa(r)$ corresponds to the value of the convergence profile at the radial distance r and $\bar{\kappa}(< r)$ is the mean enclosed convergence within r. As for the convergence profile, we average over all the 192 10x10 deg^2 flat-sky maps, in order to have better statistics.

Fig. 6.13 show the stacked tangential shear profiles of lensing voids for the CMB-lensing void catalog, the WL($z_{\rm s} = 2$) void catalog, and the Euclid lensing void catalog. As throughout the rest of the analysis we consider the three κ SNR thresholds: $\nu > 1$, $\nu > 2$ and $\nu > 3$.

First of all, it is possible to observe that the maximum value of the tangential shear $\gamma_{\rm t}^{max}$ is at distances from the void center slightly smaller than $R = R_{\rm V}$; since the shear profile of voids is only sensitive to the shape of the correspondent convergence profile, this result might be caused by the concavity that characterizes the κ void profiles.

The maximum signal of the shear is at negative values, this enforces the idea that voids acts as diverging lens as found by (Davies et al., 2018).

As for the convergence profiles, we observe that the position of the maximum is independent of the catalog we choose, although the value of $\gamma_{\rm t}^{\rm max}$ largely changes as we change the void catalog, as it happens for the κ-profiles. Quantitatively, we report in Tab. 6.10 for the three probes,

the values of γ_t^{max}, i.e. the maximum (in terms of its absolute value) of the tangential shear on the wall, and γ_t^{min}, i.e the minimum (in terms of its absolute value) of the tangential shear at the maximum depth of the lensing voids.

	γ_{max}^{CMB}	$\gamma_{max}^{WL(z_s=2)}$	γ_{max}^{Euclid}	γ_{min}^{CMB}	$\gamma_{min}^{WL(z_s=2)}$	γ_{min}^{Euclid}
$\nu > 1$	-0.0175	-0.0058	-0.0051	-0.0079	-0.0024	-0.0020
$\nu > 2$	-0.0116	-0.0042	-0.0038	-0.0050	-0.0016	-0.0014
$\nu > 3$	-0.0055	-0.0029	-0.0027	-0.0015	-0.0011	0.00010

Table 6.10: Maximum γ_{max} and minimum γ_{min} values (in terms of its absolute value) of stacked void profiles, for the three probes and κ-SNR thresholds considered in this work, in the ΛCDM cosmology.

Similarly to what we have found in the analysis of the convergence profiles, the void shear profiles for the Euclid and WL($z_s = 2$) catalogs present a similar behaviour. In fact their γ_{max} differs by ∼12% and their γ_{min} by ∼17% if we consider the catalog with $\nu > 1$. The tangential shear profile of the CMB-lensing void catalog seems, again, to be the one that shows the largest fluctuations in γ_t; in fact, $\gamma_{max}^{CMB} = -0.0175$ is one order of magnitude larger than γ_{max}^{Euclid} and $\gamma_{max}^{WLz_s=2}$, as reported in Tab. 6.10.

We recover the behaviour found also by (Davies et al., 2018), the γ_t-profiles decrease with the stacked radial distance, reach their maximum negative value near $R = R_V$, and the increase again toward the background level $\gamma_t = 0$.

We are also interested in the study of the redshift evolution of stacked tangential shear, γ_t, profiles of lensing voids. In Fig. 6.14 we show the γ_t-profiles of lensing voids for the CMB-lensing void catalogs at different redshift bins.

The γ_t-profiles show the expected behaviour: the value of the shear γ_t decreases as the radial stacked distance R/R_V increases, it reaches its maximum negative value at $R \sim 0.8R_V$ and then it increases again toward the background value. Again, the fact that the maximum of the tangential shear is not reached at $R = R_V$ might be due to the presence of a concavity in the correspondent convergence profile.

The behaviour of these curves can be thought as the dual of the κ-profiles and they show also the same properties: the height of the (negative) peaks change with the void catalogs we are considering, whereas their positions remain unchanged also if we change the value of the SNR ν applied to the original data. To better understand the main differences between these maps, we show in Tab. 6.11 and Tab. 6.12 the values of γ_t^{max} and γ_t^{min} for each map.

	$\gamma_{max}^{z_1}$	$\gamma_{max}^{z_2}$	$\gamma_{max}^{z_3}$	$\gamma_{max}^{z_4}$	$\gamma_{max}^{z_5}$	$\gamma_{max}^{z_6}$
$\nu > 1$	-0.0016	-0.0013	-0.0017	-0.0023	-0.0026	-0.0023
$\nu > 2$	-0.0008	-0.0007	-0.0009	-0.0012	-0.0015	-0.0015
$\nu > 3$	-0.0002	-0.0002	-0.0003	-0.0004	-0.0003	-0.0007

Table 6.11: Maximum γ_{max} values (in terms of its absolute value) of stacked void profiles, for the CMB-lensing catalogs at different redshifts thresholds $\nu > 1$, $\nu > 2$ and $\nu > 3$, in the ΛCDM cosmology.

If for the convergence profiles of lensing voids we see an increase in the wall height at lower redshifts, for the tangential shear profiles we see a decrease (with sign), i.e. an increase in its absolute value of the γ_t maximum a lower redshifts; it goes from $\gamma_{max}^{z_1} = -0.0016$ for $19 < z < 99$ to $\gamma_{max}^{z_6} = -0.0023$ for $0.5 < z < 1$.

	$\gamma_{\rm min}^{z_1}$	$\gamma_{\rm min}^{z_2}$	$\gamma_{\rm min}^{z_3}$	$\gamma_{\rm min}^{z_4}$	$\gamma_{\rm min}^{z_5}$	$\gamma_{\rm min}^{z_6}$
$\nu > 1$	-0.0006	-0.0005	-0.0006	-0.0009	-0.0010	0.0008
$\nu > 2$	-0.0003	-0.0003	-0.0003	-0.0005	-0.0005	-0.0005
$\nu > 3$	-0.00005	-0.00005	-0.0001	-0.0001	-0.0002	-0.0002

Table 6.12: Minimum $\gamma_{\rm min}$ values (in terms of its absolute value) of stacked void profiles, for the CMB-lensing catalogs at different redshifts thresholds $\nu > 1$, $\nu > 2$ and $\nu > 3$, in the ΛCDM cosmology.

6.5 Summary of Chapter 6

In this Chapter we present quantitative results for the analysis of κ-peak and lensing void statistics in the massless neutrino case.

We have considered three different probes: the CMB-lensing convergence map, the WL($z_{\rm s}$=2) convergence map and the Euclid lensing convergence map, in order to understand how the properties of lensing voids change when we consider different lensing source distributions. We have also focused on understanding the evolution with redshift of κ-peak counts and lensing void counts and profiles. To this aim, we have considered the CMB-lensing probe, analyzing lens regions in the following redshift ranges: $19 < z < 99$, $12 < z < 15$, $5 < z < 11$, $2.5 < z < 4$, $1 < z < 2$ and $0.5 < z < 1$.

For each map, we have created three different catalogs imposing a threshold, $\nu_{\rm cut}$, on the SNR, $\nu = \kappa/\sigma$, of κ-peaks: $\nu > 1$, $\nu > 2$ and $\nu > 3$; these catalogs allow us to analyze the properties of convergence peaks and lensing voids in terms of the non linear structure evolution, understanding how the peaks and voids are related. this respect, we find that, when we impose a higher threshold ν, we select voids with larger radii, $R_{\rm V}$, i.e. voids with a larger volume. We explain this property considering the definition of lensing void in the adopted void finder: they are region devoid of κ-peaks beyond a certain SNR threshold, therefore, as we increase the SNR, we find in the convergence maps rarer κ-peaks, and consequently larger voids, kept fixed the area of the analyzed maps.

Moreover, we recover the expected behaviour of the mean cumulative projected density of κ-peaks, $n(>\nu)$, as a function of the SNR for the three probes used. We observe that $n(>\nu)$ decrease as expected, as we increase the value of ν. In the CMB-lensing case, $n(>\nu)$ decreases much more rapidly with ν with respect to the other two probes. This is due to the different sensitivity of the three probes to the nonlinear structure evolution, being low redshift WL probes more sensitive to the latter than CMB-lensing. This explains also the reason why the CMB-lensing maps present the smallest total number of voids, even if for $\nu > 3$ the projected void number density dominates at large radii with respect the other two probes.

Concerning the evolution in redshift of κ-peak counts and void counts and size, first we notice that for $\nu > 2, 3$, lower redshift bins present a larger density of very small voids. However, the opposite happens for very large voids. In fact, in agreement with the redshift evolution of the κ-peak density, we observe that as $n(\nu > 3)$ increases from high to low redshifts, the void density decreases and extends down to lower $R_{\rm V}$ values. Such differences can reach even some orders of magnitude, depending on the redshifts and radii considered. We can say that the void distribution is the "negative image" of the κ-peak distribution, and the trends that we observe are perfectly explained within the framework of the nonlinear structure evolution.

Finally, we have analyzed the behavior of the stacked convergence and the tangential shear profile of of lensing void in our catalogs, as function of the stacked radial distance $R/R_{\rm V}$.

For the three probes we find that the Euclid-lensing and the WL($z_{\rm s}$=2) void catalogs show, as expected, a very similar behavior, whereas the CMB-lensing catalog presents large differences with respect to the other two, with void profiles characterized by the largest fluctuations between the wall (at $R = R_{\rm V}$) and the depth(at $R = 0$). Concerning the void profile evolution, we observe

that their walls and depth both increase with decreasing redshifts. Summarizing, we can say that, as the Universe evolves, lensing voids become more numerous, smaller and deeper, independently of the ν threshold considered. However, let us note that the void finder adopted in this analysis does not account for void mergers, therefore smaller voids could actually reside in larger ones.

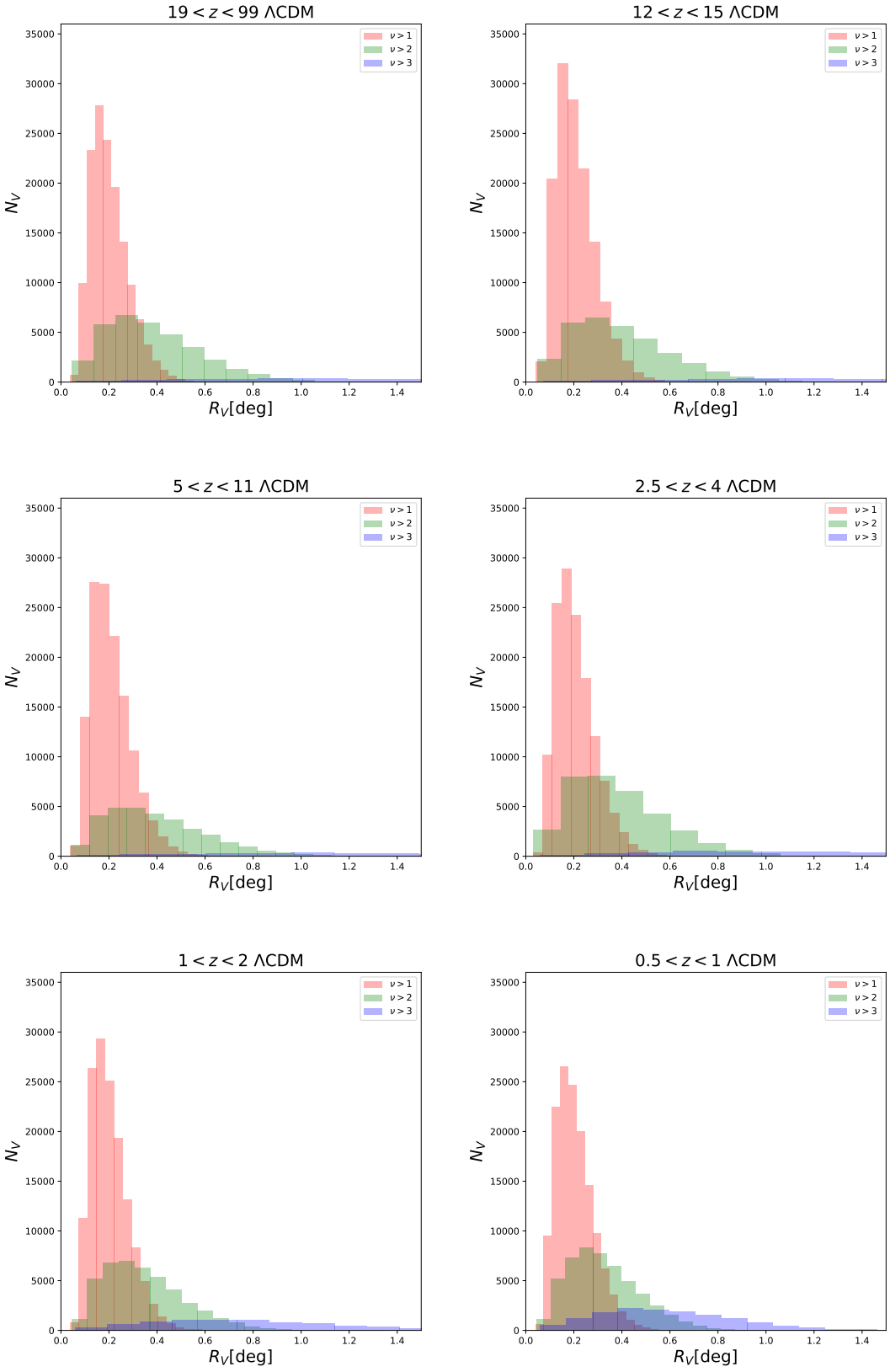

Figure 6.9: Histograms of the total number of voids as a function of their radii R_V for CMB-lensing convergence maps at different redshift ranges in the ΛCDM cosmology. We consider the three void catalogs with κ-SNR thresholds: $\nu > 1$ (red), $\nu > 2$ (olive) and $\nu > 3$ (blue).

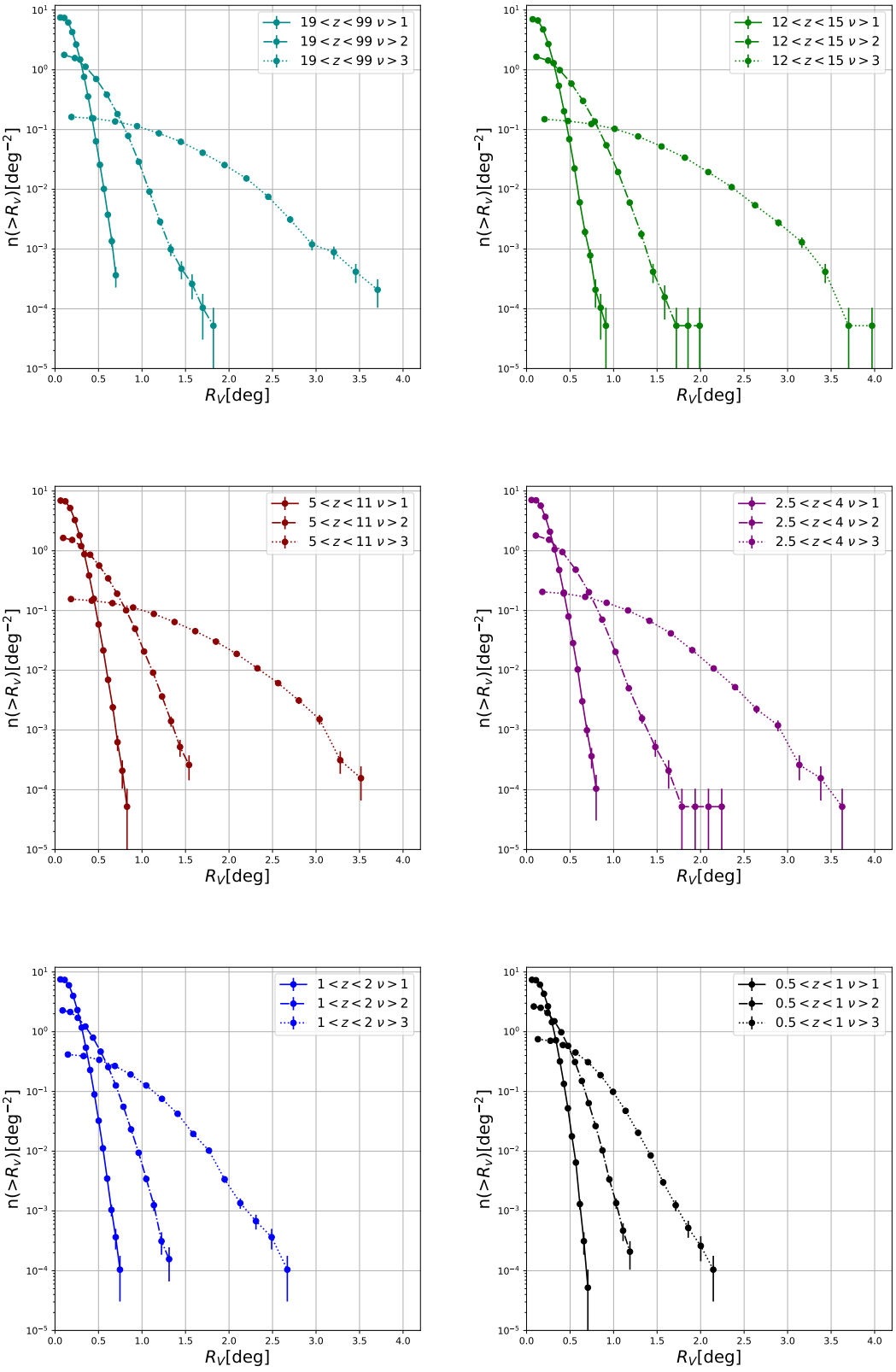

Figure 6.10: Cumulative projected density of voids as a function of their radius R_V at different redshift bins, in the ΛCDM cosmology. The curves represent three different catalogs obtained applying three different peak selection criteria: $\nu > 1$ (solid), $\nu > 2$ (dash-dotted) and $\nu > 3$ (dotted). The smoothing scale applied to all maps is θ_s=2.5 arcmin. Each curve is averaged over all the 192 10x10 deg^2 patches. Error bars show the Poisson uncertainties of the data.

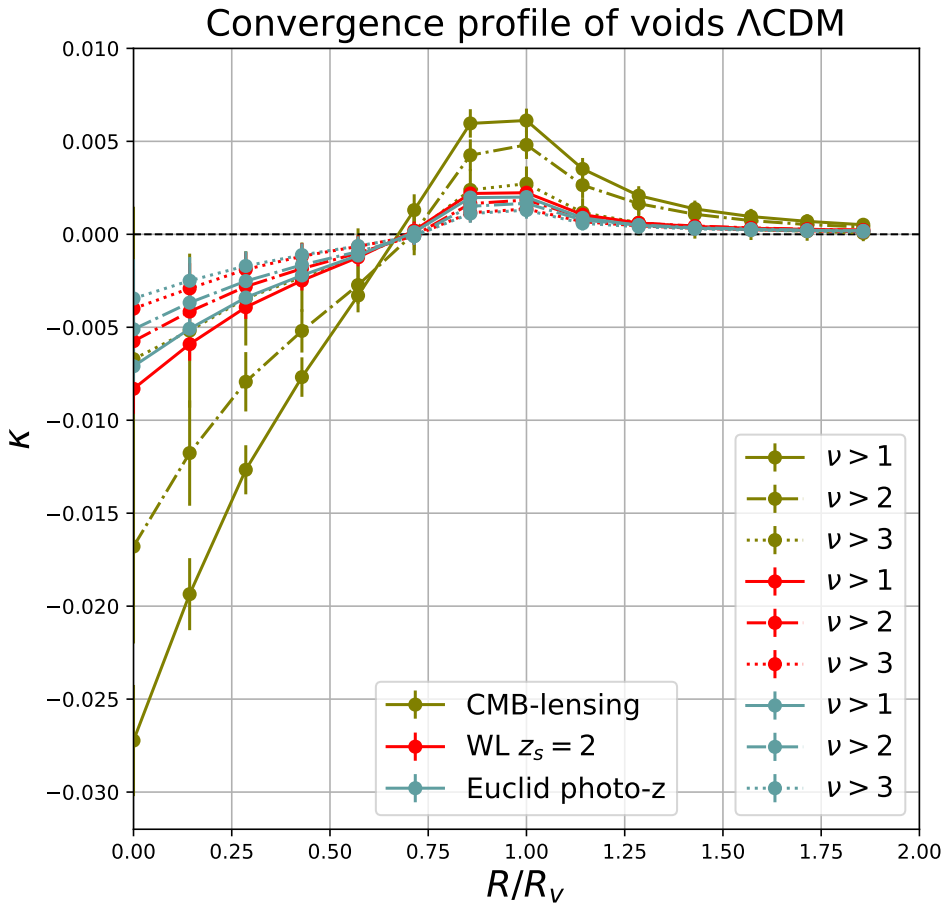

Figure 6.11: Stacked convergence profile of voids from the CMB-lensing catalog (olive), the WL(z_s = 2) catalog (red), and Euclid-lensing catalog (blue), in the ΛCDM cosmology. Different line styles correspond to different voids catalogs: $\nu > 1$ (solid), $\nu > 2$ (dash-dotted), $\nu > 3$ (dotted). Each curve is averaged over all the 192 10x10 deg^2 patches. Error bars represent the mean standard deviation.

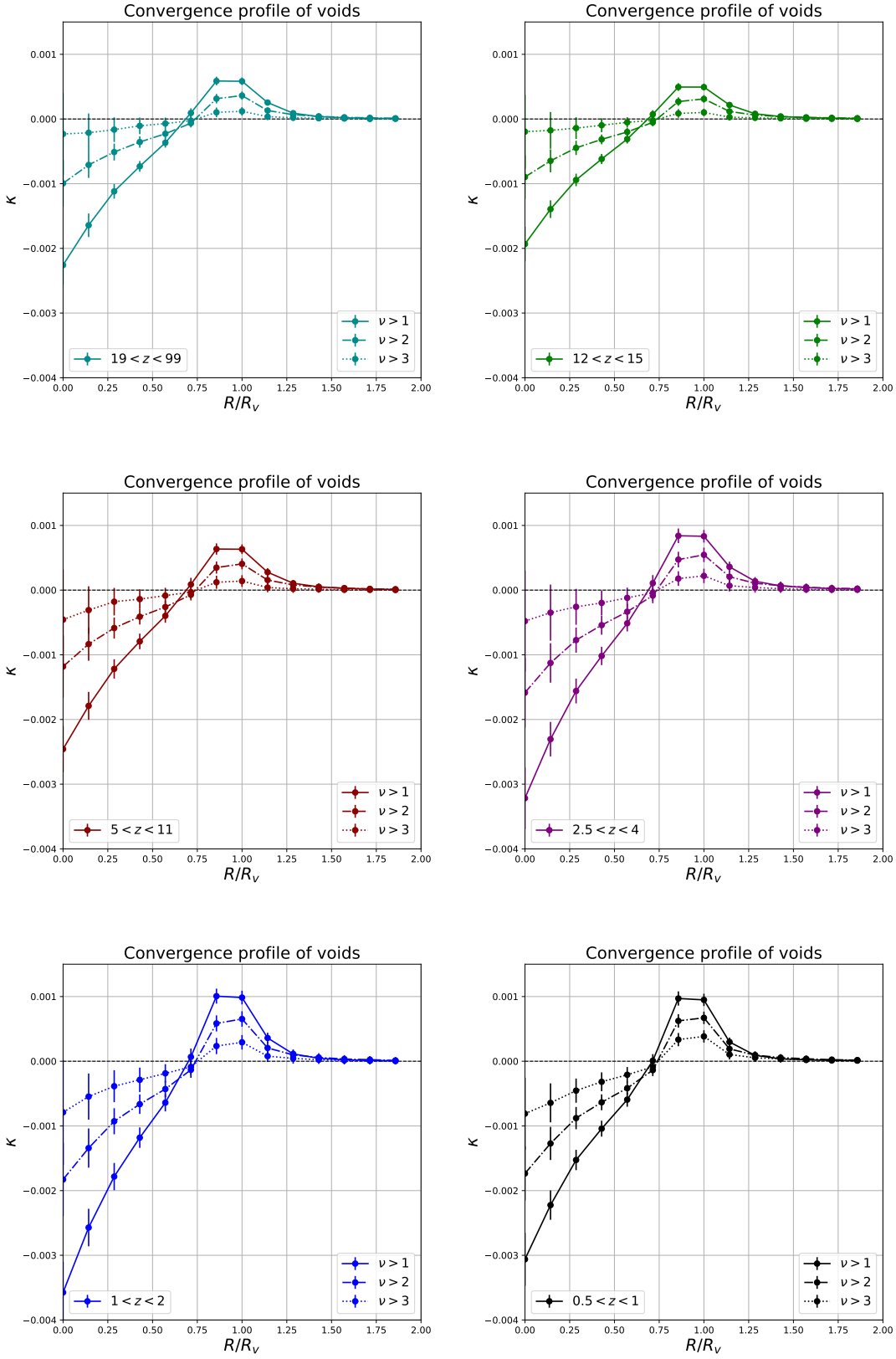

Figure 6.12: Stacked convergence profiles of lensing voids for CMB-lensing maps at different redshift ranges, in the ΛCDM cosmology. Different line styles correspond to different voids catalogs: $\nu > 1$ (solid), $\nu > 2$ (dash-dotted), $\nu > 3$ (dotted). Each curve is averaged over all the 192 10x10 deg^2 patches. Error bars show the mean standard deviation.

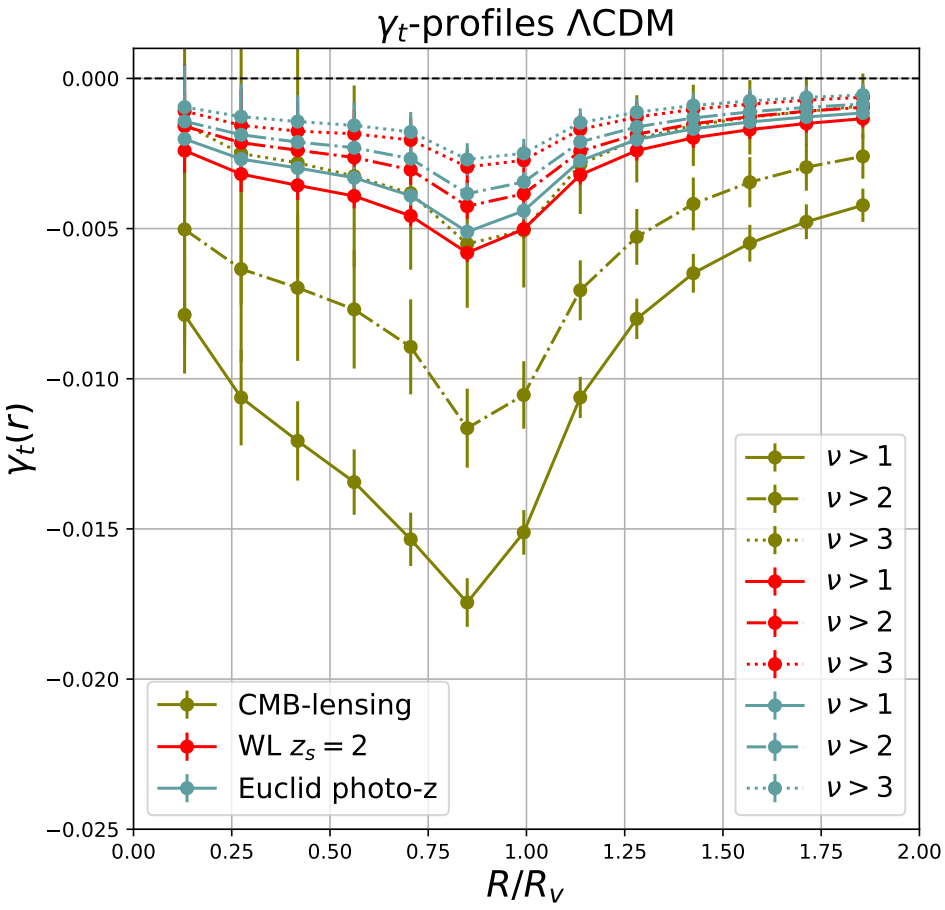

Figure 6.13: Stacked shear profile of lensing voids in the CMB-lensing catalog (olive), the WL($z_s = 2$) catalog (red), and the Euclid lensing catalog (blue) for the ΛCDM cosmology. Each curve is averaged over all the 192 10x10 deg^2 patches. Different line styles correspond to different voids catalogs: $\nu > 1$ (solid), $\nu > 2$ (dash-dotted), $\nu > 3$ (dotted). Error bars show the mean standard deviation.

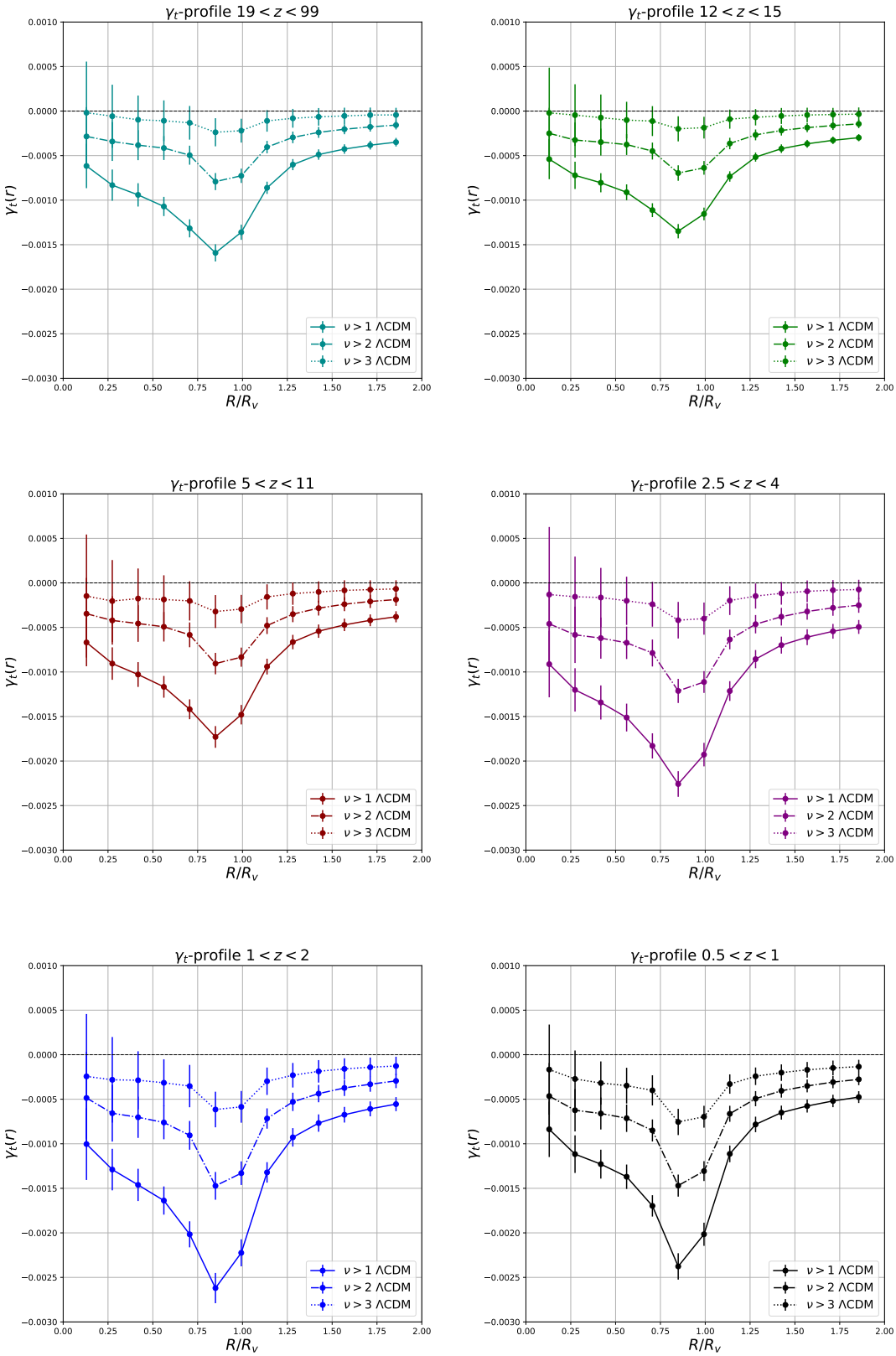

Figure 6.14: The stacked shear profile of lensing voids from the CMB-lensing catalogs at different redshift, in the ΛCDM cosmology. The coloured lines show the average profile for the three void catalogs: $\nu > 1$ (solid), $\nu > 2$ (dash-dotted) and $\nu > 3$ (dashed). Each curve is averaged over all the 192 10x10 deg^2 patches. Error bars show the mean standard deviation.

Chapter 7

Lensing voids in the presence of massive neutrinos

In the previous Chapter we have analysed lensing voids and their main properties and evolution starting from simulated lensing maps in massless neutrino scenario, for three different probes: CMB-lensing, WL($z_s = 2$), and Euclid lensing. Now we focus on the massive neutrino case, using the $\nu\Lambda$CDM counterpart of these simulated lensing maps obtained via ray-tracing from the DEMNUni simulations. We consider the case of a total neutrino mass $M_\nu = 0.16\,\mathrm{eV}$.

For the first time in the literature, we will study lensing voids in the presence of massive neutrinos and understand how their free-streaming impacts their properties and evolution.

7.1 Convergence peaks in the $\nu\Lambda$CDM scenario

As said in the previous Chapter, one of our goals is the study of the evolution with redshift of κ-peak statistics and lensing voids. To this aim, we consider again different redshift bins, and sum up together the full-sky CMB-lensing κ-maps described in Section 5.2. In this way we construct spherical shells around the observer with a thickness in redshift able to provide a fair sample of lensing voids in each redshift bin, and study how they evolve in the presence of massive neutrinos with $M_\nu = 0.16\,\mathrm{eV}$. The considered redshift bins are shown in Tab. 7.1 and coincide with the one chosen in the ΛCDM analysis.

z_1	z_2	z_3	z_4	z_5	z_6
$19 < z < 99$	$12 < z < 15$	$5 < z < 11$	$2.5 < z < 4$	$1 < z < 2$	$0.5 < z < 1$

Table 7.1: Redshift bins chosen for the study of the void redshift evolution.

The procedure of κ-peak extraction is the same followed in the case of the ΛCDM model: we first identify the κ-peaks that are maxima of the convergence field. Again, we apply a Gaussian filter with a smoothing scale $\theta_s = 2.5$ arcmin, and use the *Locate Peaks* package to produce κ-peak catalogs from the simulated lensing maps.

In Fig. 7.1 the convergence difference map for the WL($z_s = 2$) case, obtained subtracting two corresponding 10x10 deg^2 patches, one in the $\nu\Lambda$CDM cosmology, the other ΛCDM model. We have considered the weak lensing map with sources located at $z = 2$ since we expect that the effect of massive neutrinos starts being more important at lower redshift values, when they thermal velocities become non relativistic. We have used the Log-scale in order make more visible the structures inside the section. We expect to see a suppression of the perturbations in the convergence field due to the presence of free streaming massive neutrinos. Comparing with Fig. 5.5, we can observe that the difference in κ are 1-2 orders of magnitude smaller than κ itself,

as it should be. This maps represents the difference in the projected dark matter distribution due to the presence of massive neutrinos.

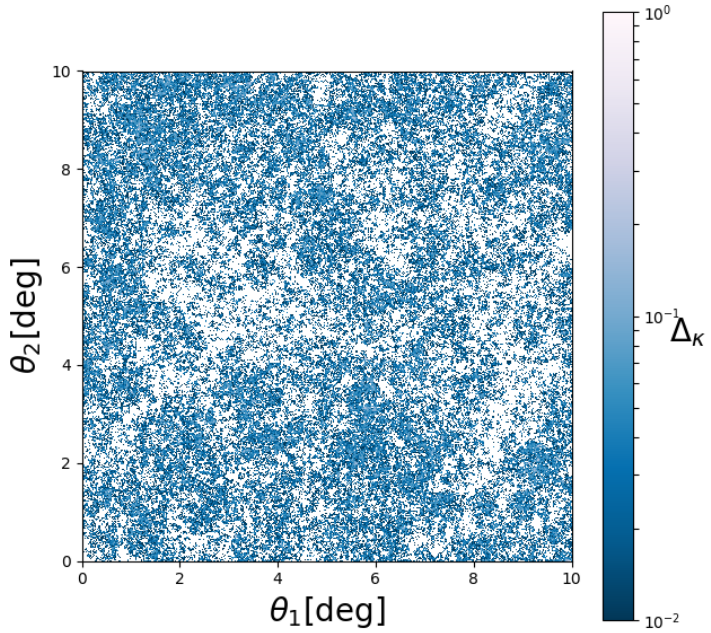

Figure 7.1: Example of a convergence difference Δ_κ map between the $\nu\Lambda$CDM and the ΛCDM scenarios, for the WL(z_s=2) case. Color scale is logarithmic, coordinates on x- and y-axis in deg on a flat patch.

Fig. 7.2 shows the cumulative projected density of convergence peaks for the CMB-lensing map, the WL(z_s = 2) map and the Euclid lensing map, as a function of the signal to noise ratio $\nu = \kappa/\sigma$ with sigma being the standard deviation associated to the smoothed maps. In Tab. 7.2 we report the values of the mean standard deviations for the three probes in both the cosmologies.

	$\nu\Lambda$CDM	ΛCDM
$\sigma_{\rm CMB}$	0.050	0.051
σ_{z_2}	0.025	0.034
$\sigma_{\rm Euclid}$	0.023	0.032

Table 7.2: Averaged standard deviations computed on the convergence CMB-lensing map, the WL(z_s = 2), and Euclid-like lensing map, in the $\nu\Lambda$CDM cosmology (left column) and the ΛCDM one (right column).

From Tab. 7.2, we observe that the CMB-lensing case presents only a 2% decrease in the value of σ_k w.r.t. the massless neutrino case. The other two lensing maps, WL(z_s=2) and Euclid lensing one, present a much smaller value of σ_k (26% and 28%, respectively) than in the massless neutrino cosmology. This confirms the suppression of matter perturbations due to the presence of massive neutrinos, especially at low redshifts.

From the cumulative projected density of convergence peaks in Fig. 7.2 we recover that the number of peaks is greater for small SNR as in the ΛCDM case, in this sense we recover the expected behaviour also for the massive neutrino scenario. It is interesting to notice that the

behaviour of the three curves in the $\nu\Lambda$CDM scenario is similar to the one of the ΛCDM one, with the CMB-lensing map having the smallest significant κ-peaks associated.

For what concerns the differences of each probe between the two cosmologies, we can refer to the top-left, the bottom-left and the bottom-right panel of Fig. 7.2, where we show the mean cumulative projected density of κ-peaks, obtained averaging over all the cumulative projected density of κ-peaks extracted from the 192 flat-sky sections we have projected and divided the original full-sky maps onto. In addition, in all cases we have added a sub-panel showing the values of the percent residuals of the projected density of κ-peaks between the two cosmologies. In particular, to quantify the difference between the massless and massive neutrino case, both for the κ-peak and void statistics, we have evaluated the following percent residuals for the projected peaks density as a function of $\nu = \kappa/\sigma$, and for the projected void density as a function of $R_{\rm V}$:

$$\Delta_{R_{\rm V}/\nu}(\%) = \left(\frac{n_{\nu\Lambda{\rm CDM}}}{n_{\Lambda{\rm CDM}}} - 1\right) * 100 \tag{7.1}$$

We adopt a similar notation also for the percent residuals of the convergence and shear stacked void profiles, as a function of $R/R_{\rm V}$, as we discuss in the next Sections. It is this percent residual that highlights the main differences between the two cosmologies and manifests the effects of the presence of massive neutrinos.

In Tab. 7.3 we report the mean values of $\Delta_\nu(\%)$ for each probe. In this case we are interested in the analysis of how the projected density of κ-peaks changes with the neutrino mass. The values of $\Delta(\%)$ as a function of ν can be found in Tab. B.1

	$\bar{\Delta}_\nu(\%)$
CMB-L	-2
$z_{\rm s} = 2$	-3
Euclid	-4

Table 7.3: Mean values of $\Delta_\nu(\%)$ (as defined in Eq. (7.1)) for the CMB-lensing map, the WL($z_{\rm s} = 2$) map, and the Euclid-like lensing map.

From Tab. 7.3 and Fig. 7.2, we can observe that the presence of massive neutrinos decreases as expected the projected κ-peak density. However, given the small value of the total neutrino mass considered, $M_\nu = 0.16$ eV, such suppression is of few %, being the Euclid lensing map the most affected, since it is characterized by a source distribution extending down to $z = 0.5$ and therefore more sensitive to the free streaming scale of neutrinos which affects more nonlinear scales as the redshift decreases.

More specifically, for the CMB-lensing peaks counts, where we recover $\bar{\Delta}(\%)\nu = -2\%$. The WL($z_{\rm s} = 2$) and Euclid lensing cases show instead some discrepancies for higher ν threshold, in fact we find: $\bar{\Delta}(\%)_\nu^{\rm Euclid} = -3\%$ and $\bar{\Delta}(\%)_\nu^{z_{\rm s}=2} = -4\%$.

Again, we recover that the CMB-lensing map has the smallest ν associated to the κ-peaks, it does not go above $\kappa/\sigma \sim 5$, whereas the Euclid and the WL($z_{\rm s} = 2$) cases have values of ν much larger, with the maximum $\kappa/\sigma \sim 9$.

The discrepancies between the two cosmologies are more visible for the Euclid-like map and the WL($z_{\rm s}$=2) map at large ν; from a physical point of view we expect, indeed, that massive neutrinos are effective for maps that cover lower redshift ranges, where they are less relativistic. This is the case for the two probes above. The discrepancies of the two κ-peak catalogs between the massless and massive neutrino case are very similar as we can observe from Fig. 7.2, and reaching a difference of $\sim 20\%$ at larger ν values, $\nu \gtrsim 6$. Larger values of the signal to noise ratio means imply larger values of the convergence κ and, as a consequence, we are looking at high density structures. The mean values of $\Delta(\%)$ are negative, so in the $\nu\Lambda$CDM case the cumulative projected density of κ-peaks gets slightly smaller with respect to the massless neutrino scenario.

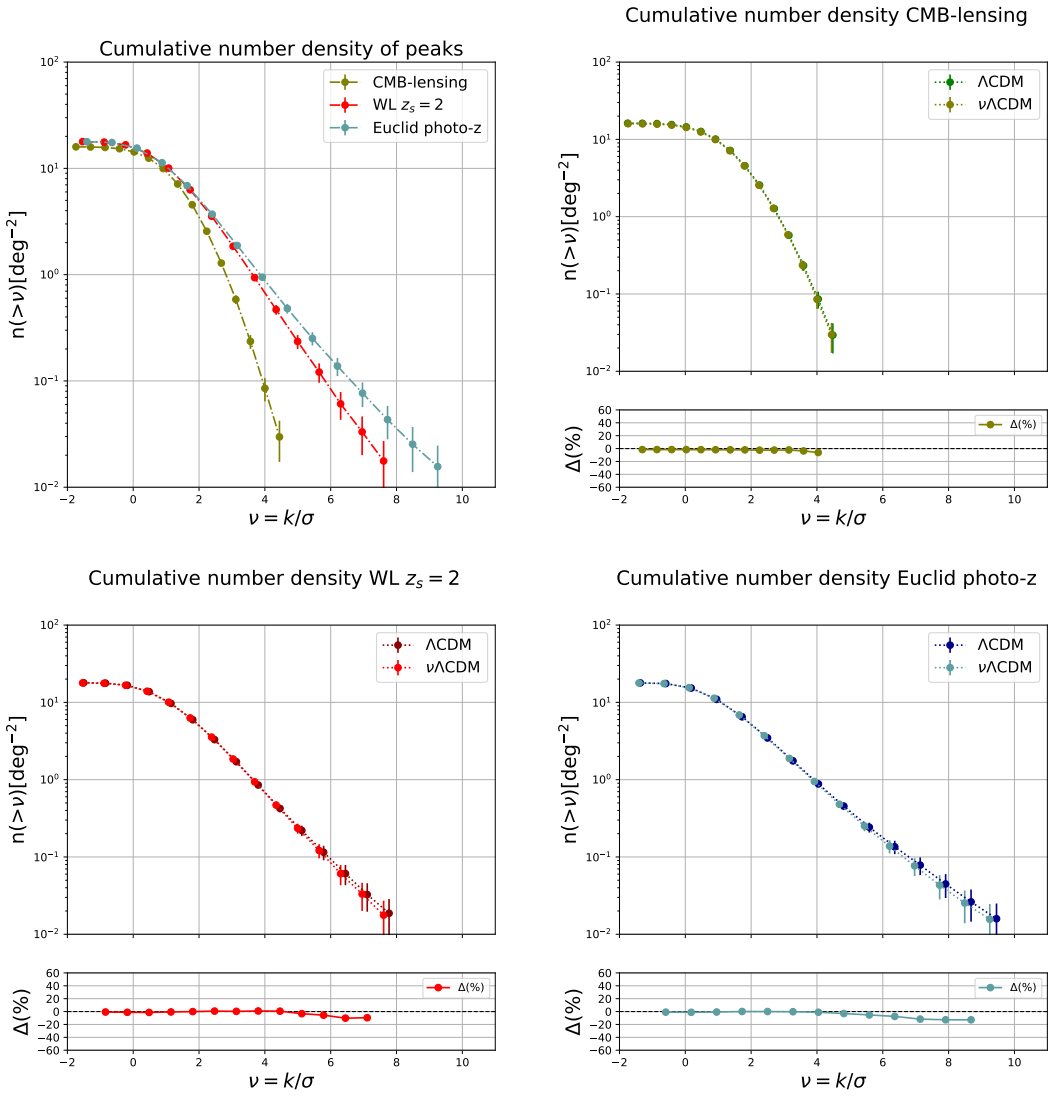

Figure 7.2: TOP-LEFT: cumulative projected density of convergence peaks as a function of $\nu = \kappa/\sigma$ for the three probes in the $\nu\Lambda$CDM cosmology: CMB-lensing (TOP-RIGHT), WL($z_s = 2$) (BOTTOM-LEFT), Euclid lensing (BOTTOM-RIGHT). In the latter panels different colors refers to the $\nu\Lambda$CDM and standard ΛCDM cosmology. The sub panels show the $\Delta_\nu(\%)$ (as defined in Eq. (7.1)) of the cumulative projected density of κ-peaks between the $\nu\Lambda$CDM scenario and the ΛCDM one. Error bars represent Poisson noise.

Now, we want to check what happens to the cumulative projected density of the convergence peaks when we consider lensing maps at different redshift ranges in the $\nu\Lambda$CDM cosmology.

Fig. 7.3 shows $n(> \nu)$ as a function of κ/σ, for the CMB-lensing partial maps with redshifts reported in Tab. 7.1. The corresponding mean values of the standard deviation of the smoothed maps are reported in Tab. 7.4. As expected, we can observe that the difference between the two scenarios start to be visible only at low redshits, in the fith and sixth redshift bin, i.e. at $z < 1$, reaching 3% at maximum.

	σ_{z_1}	σ_{z_2}	σ_{z_3}	σ_{z_4}	σ_{z_5}	σ_{z_6}
$\nu\Lambda$CDM	0.0041	0.0040	0.0041	0.0060	0.0060	0.0058
ΛCDM	0.0041	0.0038	0.0041	0.0059	0.0062	0.0060

Table 7.4: Mean standard deviations of the convergence field, for the the CMB-lensing maps integrated in different redshift range in the $\nu\Lambda$CDM cosmology.

Also in this case, Fig. 7.3 shows the expected decreasing behaviour and the projected density of κ-peaks as the SNR increases, while, as the redshift decreases, the algorithm finds a larger number of convergence peaks with greater ν values.

In order to analyse the main differences between the ΛCDM and the $\nu\Lambda$CDM cosmologies, we show in Fig.7.3 the plots of the mean cumulative projected density of κ-peaks as function of the SNR associated to each map with a sub-panel showing the percent residuals $\Delta_\nu(\%)$ between the two cases.

Again, we refer to Tab. 7.5 where we report the mean value of $\Delta_\nu(\%)$ for each redshift range. The values of $\Delta_{\rm nu}(\%)$ at each $\nu = \kappa/\sigma$ can be found in Tab. B.2.

z_i	$\bar{\Delta}_\nu(\%)$
$19 < z < 99$	15
$12 < z < 15$	-2
$5 < z < 11$	1
$2.5 < z < 4$	0.4
$1 < z < 2$	-2
$0.5 < z < 1$	-5

Table 7.5: Mean values of $\Delta_\nu(\%)$ (as defined in Eq. (7.1)) for the κ-peak catalogs extracted from the partial CMB-lensing maps in different redshift bins.

The cumulative projected density at $19 < z < 99$ is the one that shows the largest discrepancies between the two cosmologies. These discrepancies are clearly visible for ν, where the $\nu\Lambda$CDM case has a value of $n(> \nu)$ greater with respect to the massless scenario, in fact $\Delta_\nu(\%)$ goes up to $\sim 80\%$, and its average is $\sim 15\%$. On the contrary, for lower significant κ-peaks, the two cosmologies behave almost the same. However, such behavior is not representative of the matter perturbation suppression due to massive neutrinos, since at these very high redshift neutrinos with $M_\nu = 0.16$ eV are still relativistic. These fluctuation could be due to the rescaling technique used to produce the initial condition of the DEMNUni simulations, which produces artificially more power spectrum in the presence of massive neutrinos at very high redshifts, in order to match the correct matter power spectrum at lower redshifts.

The κ-peak projected densities at redshifts $12 < z < 15$, $5 < z < 11$ and $2.5 < z < 4$ have a $\bar{\Delta}_\nu(\%)$ equal to -2%, 1%, and 0.4%, respectively, so there are very small discrepancies between the two cosmological models. Again, we expect that the effect of massive neutrinos starts being detectable at lower redshift ranges, namely smaller that $z \sim 1$.

From Tab. 7.5, we can observe how catalogs at lower redshifts are the one that show again some discrepancies at higher $\nu = \kappa/\sigma$: $\bar{\Delta}_\nu(\%)$ for the maps at $1 < z < 2$ and $0.5 < z < 1$, in fact, corresponds to -2% and -5%. The discrepancies, although being still very small, acts on higher significant peaks. So this means that the maps with massive ν are smoother with respect to the corresponding massless case and that the peaks we find inside each section are qualitatively less brighter. Finally, from Fig.7.3 we can appreciate how the percent difference between the κ-peak projected densities in the two cosmological scenarios reach $\sim 20\%$ at $\nu > 6$ for $0.5 < z < 1$. This is because nonlinear structure evolution is suppressed in the presence of massive neutrinos.

7.2 Void counts in the $\nu\Lambda$CDM scenario

We produce three different κ-peak catalogues in the $\nu\Lambda$CDM cosmology imposing different thresholds $\nu_{\rm cut} = 1, 2, 3$ to the simulated lensing maps of the three probes considered, and applying the tunnel finding algorithm (Davies et al., 2018) to such catalogues, we identify the lensing voids.

We follow the same procedure described in Chapter 6 for the analysis of lensing voids in the ΛCDM scenario. Thus, as a first step it can be interesting to show the histograms of the total number of lensing voids $N_{\rm V}$ as a function of their radius $R_{\rm V}$. In this section we are interested in the identification of the effects that massive neutrinos have on different probes and on maps that cover a wide redshift range.

In Fig. 7.4 on the left column we show the histograms of the total number of lensing voids $N_{\rm V}$ found in the CMB-lensing, the WL map($z_{\rm s} = 2$) and the Euclid lensing catalogs as a function of $R_{\rm V}$. On the right column we show the histograms obtained considering the corresponding catalogs in the massless neutrino case.

We report the total number of voids $N_{\rm V}$ for the three thresholds in Tab. 7.6.

	$N^{\nu\Lambda\rm CDM}_{\rm V,CMB}$	$N^{\Lambda\rm CDM}_{\rm V,CMB}$	$N^{\nu\Lambda\rm CDM}_{\rm V,z_s=2}$	$N^{\Lambda\rm CDM}_{\rm V,z_s=2}$	$N^{\nu\Lambda\rm CDM}_{\rm V,Euclid}$	$N^{\Lambda\rm CDM}_{\rm V,Euclid}$
$\nu > 1$	22168	21775	25700	26558	24428	24427
$\nu > 2$	3880	3772	6448	6213	6400	6146
$\nu > 3$	293	379	1266	1380	1655	2150

Table 7.6: Total number of voids $N_{\rm V}$ in the void catalogs of CMB-lensing, WL($z_{\rm s} = 2$), and Euclid-like lensing map in the massive and massless neutrino cosmological scenarios.

We can observe that for the catalog with $\nu > 1$ there are not particular differences in the total number of lensing voids between the two cosmologies. Instead, looking at larger thresholds and therefore larger void sizes, i.e. at catalogues with $\nu > 3$, we clearly see that the total number of lensing voids in the presence of massive neutrinos is smaller than in the ΛCDM scenario, in which higher κ-peaks are rarer and therefore voids devoid of them are also rarer but of larger size. The number of voids for the CMB-lensing case shows a variation of $\sim -23\%$, whereas the WL($z_{\rm s}$=2) and the Euclid catalogs show variation of $\sim -8\%$ and $\sim 23\%$, respectively, as compared to the massless neutrino case.

Then we study the redshift evolution of void counts in the case of CMB-lensing, focusing on differences between the massive and massless neutrino case.

In Fig. 7.5 we show the histograms of the total number of voids as a function of their radius $R_{\rm V}$. We consider the following redshift bins: $2.5 < z < 4$, $1 < z < 2$ and $0.5 < z < 1$; being low redshifts, these are the most interesting catalogs to take into account in order to observe the effects of the presence of massive neutrinos in the simulated data. On the left we show the $\nu\Lambda$CDM scenario, on the right the the ΛCDM one.

Moreover in Tab. 7.7 we report the total number of lensing voids for the two cosmologies. For what concerns the differences between the two cosmologies, the maximum number of voids found

in all the projected section is slightly lower with respect to the scenario with massless neutrinos, this is valid especially for $\nu > 3$. In fact, for the lensing map that covers a redshift range of $1 < z < 2$ we see a decreasing of the total number of identified voids of about the 9%, the map at $0.5 < z < 1$ shows a $\Delta(\%)$ of $\sim -9\%$, in agreement with our idea of the suppression effect of the perturbations in the convergence field at larger signal to noise ratios at lower values of z.

From Tab. 7.7 and Fig. 7.5 we infer that the total number of voids decreases as we increase the value of SNR from $\nu > 1$ to $\nu > 2$. This is due to the fact that high signal to noise ratio values imposed (with $SNR = \kappa/\sigma$ as in the ΛCDM case) imply selecting voids with larger radii that are statistically less numerous than smaller voids.

Both the catalogues with $\nu > 2$ and $\nu > 3$ present a smaller number of lensing voids in the massive neutrino scenario with respect to the massless neutrino case. If we take, for example, the lensing catalog with redshift range $0.5 < z < 1$, $N_{\rm V}$ decreases by $\sim -2\%$ for $\nu > 2$ and by $\sim -9\%$ for $\nu > 3$. We are detecting the neutrino effect of smoothing the convergence field, and therefore reducing the identified lensing void number, as expected at low redshifts.

	$N^{\nu\Lambda\rm CDM}_{\rm V,z_4}$	$N^{\Lambda\rm CDM}_{\rm V,z_4}$	$N^{\nu\Lambda\rm CDM}_{\rm V,z_5}$	$N^{\Lambda\rm CDM}_{\rm V,z_5}$	$N^{\nu\Lambda\rm CDM}_{\rm V,z_6}$	$N^{\Lambda\rm CDM}_{\rm V,z_6}$
$\nu > 1$	27915	28914	2788	29316	28794	26528
$\nu > 2$	5637	8048	7128	7008	8224	8379
$\nu > 3$	513	508	990	1088	2012	2206

Table 7.7: Total number of voids $N_{\rm V}$ in different redshift bins extracted from the CMB-lensing probe.

We now analyze the behavior of the cumulative projected density of lensing voids as a function of $R_{\rm V}$ in the $\nu\Lambda$CDM cosmology.

In particular we consider the cumulative projected void densities $n(> R_{\rm V})$, as a function of the void radius, for CMB-lensing, WL($z_{\rm s} = 2$), and for Euclid lensing catalogs, as shown in Fig. 7.6. All the curves quantitatively confirm the dependence of the void sizes on the signal to noise ratio ν: the projected density of voids decreases as the value of their radii increases. In particular, for the CMB-lensing case, catalogs with $\nu > 1$ have more small voids and fewer larger voids with none above $R_{\rm V} = 1.2\,$deg, whereas all the catalogs with $\nu > 3$ present less smaller voids but more large voids with radii larger than $R_{\rm V} = 3.0\,$deg.

The other panels in Fig. 7.6 show the cumulative projected void densities $n(> R_{\rm V})$, as a function of the void radius,for the three probes, both for the ΛCDM and the $\nu\Lambda$CDM scenarios. Since our purpose is underlying the main difference between these two cosmologies, we have added for each probe a sub-panel showing the $\Delta_{R_{\rm V}}(\%)$ between the two number densities. Similarly to the previous analysis we have considered three different κ-SNR thresholds.

In Tab. 7.8 we report the mean values of $\Delta_{R_{\rm V}}(\%)$, while in Tab. B.3 we report all the values of $\Delta_{R_{\rm V}}(\%)$ as a function of $R_{\rm V}$.

	$\bar{\Delta}_{R_{\rm V}}(\%)_{\nu>1}$	$\bar{\Delta}_{R_{\rm V}}(\%)_{\nu>2}$	$\bar{\Delta}_{R_{\rm V}}(\%)_{\nu>3}$
CMB-Lensing	19	10	1
WL($z_{\rm s} = 2$)	33	10	9
Euclid photo-z	13	11	13

Table 7.8: Mean values of $\Delta_{R_{\rm V}}(\%)$ as defined in Eq.(7.1) for the cumulative projected density of lensing voids for the CMB-lensing map, the WL($z_{\rm s} = 2$) map and the Euclid-like map for the three different catalogs $\nu > 1$, $\nu > 2$ and $\nu > 3$.

For what concerns the CMB-lensing void catalog in the top-right panel of Fig. 7.6 we see that all catalogs show a $\Delta(\%) \sim (0 - 5)\%$ for small values of $R_{\rm V}$; however, as we move towards large

values of R_V, and we consider voids with larger sizes for each threshold, the percent difference with respect to the massless neutrino case are evident and positive for all the three SNR catalogs, as the radius increases. For the $\nu > 1$ catalog, $\Delta(\%) \sim 40\%$ at $R_V = 0.65\,\mathrm{deg}$; for the $\nu > 2$ catalog, $\Delta(\%) \sim 40\%$ at $R_V = 1.7\,\mathrm{deg}$ and for the $\nu > 3$ catalog, $\Delta(\%)$ reaches the 20% at $R_V = 3.0\,\mathrm{deg}$. The catalog with $SNR = \nu > 3$ is the one that does not show particular deviations at large R_V.

The cumulative projected void density $n(> R_V)$ associated to the WL($z_s = 2$) catalog is shown in the bottom-left panel of Fig. 7.6. What we observe in this case is the presence of a spike in the value of $\Delta(\%)$ for the $\nu > 1$ catalog at $R_V = 1.0\,\mathrm{deg}$, where the two cosmologies differ by 245%, this means that at this particular value of the radius the projected density of voids is very different between the two cases in analysis, but it is not related to the presence of massive neutrinos, especially because the other two catalogues do not show the same spikes for larger R_V and they have a more continuous behavior. We attribute this spike to statistical fluctuations between the catalogs in the different cosmologies.

The bottom-right panel in Fig. 7.6 shows the Euclid lensing case. As expected, this presents the most significant deviations between the two cosmologies. The catalog with $\nu > 1$ at a large fluctuation at $R_V \sim 0.9\,\mathrm{deg}$ where $\Delta(\%) = 76\%$ and then it goes rapidly towards negative values. Also the catalog $\nu > 3$ shows the same behavior.

In general, as concerns the cumulative projected void density as a function of the void radius, the difference between the massive and massless neutrino cases can be inferred from Tab. 7.8, which reports the mean values of $\Delta_{R_V}(\%)$. We can observe that for all the probes and all the SNR thresholds, the void densities in the $\nu\Lambda$CDM cosmologies are larger on the average with respect to the ΛCDM case. This is again explained considering that free streaming massive neutrinos suppress structure formation, so for a given threshold, the number of κ peaks decreases, and consequently the number of voids with a given size increases when massive neutrinos are present.

Now, we focus on the evolution of void counts and investigate differences between the massive and massless neutrino scenarios. Fig. 7.7 shows the cumulative projected density of lensing voids at different redshifts extracted from the partial CMB-lensing catalogs.

We also report in Tab. 7.9 the values of $\Delta(\%)$ mean found for each redshift bin and each SNR threshold. All the data can be found in Tab. B.4 and Tab. B.5.

z_i	$\bar{\Delta}_{R_V}(\%)_{\nu>1}$	$\bar{\Delta}_{R_V}(\%)_{\nu>2}$	$\bar{\Delta}_{R_V}(\%)_{\nu>3}$
$19 < z < 99$	2	2	-6
$12 < z < 15$	3	-1	11
$5 < z < 11$	-1	11	19
$2.5 < z < 4$	-2	-17	13
$1 < z < 2$	6	12	4
$0.5 < z < 1$	42	19	6

Table 7.9: Mean values of the percent residuals, $\Delta_\nu(\%)$ (as defined in Eq.(7.1)), as a function of the void radius, between the massive and massless neutrino cases, for the void cumulative projected density as measured in the partial CMB-lensing maps at different redshift bins

.

Inspecting Tab. 7.9 and the sub-panels in Fig. 7.7 we see that the catalogs with threshold $\nu > 3$ are the ones with larger deviations for large R_V, so for larger void sizes. In fact, these catalogs show a mean value of $\Delta(\%)$ larger if compared to the other two catalogs. For example, the map with $5 < z < 11$ has a $\bar{\Delta}_{R_V}(\%)_{\nu>3} = 19\%$, whereas $\bar{\Delta}_{R_V}(\%)_{\nu>1} = -1\%$ and $\bar{\Delta}_{R_V}(\%)_{\nu>2} = 11\%$.

The maps at lower redshift ranges shows differences between the two cosmologies for the catalogs $\nu > 1$ and $\nu > 2$, as well. In particular, the void catalog at $0.5 < z < 1$ has a $\bar{\Delta}_{R_V}(\%)_{\nu>1} =$

42% with a large fluctuation at $R_V \sim 0.6\,\mathrm{deg}$.

Overall, from Tab. 7.9 we can infer that on the average the massive neutrino scenario presents a larger number of voids with respect to the massless case, at a given void radius. This difference is present at each redshift, even if it doe not evolve monotonically with z, due probably to noise effects present in the catalogs.

7.3 Void convergence profiles in the $\nu\Lambda$CDM scenario

At this point of the analysis we are interested in the study of the stacked κ-profiles of lensing voids identified from convergence maps in the case of $\nu\Lambda$CDM cosmology, focusing on the identification of the main differences between the two cosmologies. We expect that the free-streaming of massive neutrinos slightly modifies the κ-profiles both for different probes and at different redshifts, especially at lowones.

As for in the massless neutrino case, we compute convergence profiles of lensing voids by using annuli of thickness R_V/N_{bin}, with R_V being the radius of the lensing voids of our flat-sky patches and $N_{bin} = 15$ being the number of bins that we find to the be the best one to analyse our data. We stack all the voids and plot the κ-profiles in terms of their scaled radial distance R/R_V. Then, we average over all the 192 10x10 deg^2 flat-sky patches in order to have better statistics.

We follow the same steps of the previous analysis, and we first analyze the convergence profiles of the CMB-lensing, the WL($z_s = 2$), and the Euclid lensing void catalogs. Fig. 7.8 shows the obtained stacked convergence profiles of lensing voids.

As for the ΛCDM cosmology, the curves show the radial distance up to $R = 1.86R_V$ and, as expected, we see that the convergence κ for larger R/R_V decreases toward the zero value, that is set as the background level. In all cases for $R < 0.75R_V$ we have negative convergence values, this implies that we are inside an under-dense region in that radial range, therefore we are inside a void. Moreover, as in the ΛCDM case, the catalogs with $\nu > 3$ have the less under-dense voids, and present the smallest value of κ_{max}; this is caused by the tiny over-densities that lay inside larger voids when we impose a larger threshold to the κ-peaks.

Once we have highlighted the main features of the κ-profiles of cosmic voids in the $\nu\Lambda$CDM cosmology, now we want to underline the main differences between the cosmology with massless and the massive neutrinos.

In Eq. (7.2) we define the percent residuals for the κ and γ stacked void profiles, $\Delta^{\kappa}_{R/R_V}(\%)$ and $\Delta^{\gamma}_{R/R_V}(\%)$, as a function of R/R_V:

$$\Delta^{\kappa}_{R/R_V}(\%) = \left(\frac{\kappa_{\nu\Lambda CDM}}{\kappa_{\Lambda CDM}} - 1\right) * 100,$$
$$\Delta^{\gamma}_{R/R_V}(\%) = \left(\frac{\gamma_{\nu\Lambda CDM}}{\gamma_{\Lambda CDM}} - 1\right) * 100, \tag{7.2}$$

where $\kappa_{\nu\Lambda CDM}$ and $\kappa_{\Lambda CDM}$ are the values of the convergence, while $\gamma_{\nu\Lambda CDM}$ and $\gamma_{\Lambda CDM}$ are the values of the tangential shear profile, in the two cosmologies respectively.

In Fig. 7.8 we have inserted a top-left panel showing the κ-profiles associated to the three maps for the catalogs $\nu > 1$, $\nu > 2$ and $\nu > 3$ with the aim of identifying the differences between the three probes in the case of massive neutrinos. The other panels show the κ-profiles of the two cosmologies with a sub-panel with the $\Delta(\%)$ of the κ values between the $\nu\Lambda$CDM cosmology and the ΛCDM one for the usual catalogs.

In Tab. 7.10 it is possible to see the mean $\Delta_{R/R_V}(\%)$ values and how they change with the ν thresholds imposed. In Tab. B.6 it is possible to find the values of $\Delta_{R/R_V}(\%)$ found for each R/R_V.

What we recover from the sub-panels in Fig. 7.8 is that the CMB-lensing curves show a very similar behaviour between the two cosmologies, in fact we recover $\bar{\Delta}_{R/R_V}(\%)^{CMB}_{\nu>1} = -4\%$,

	$\bar{\Delta}^{\kappa}_{R/R_V}(\%)_{\nu>1}$	$\bar{\Delta}^{\kappa}_{R/R_V}(\%)_{\nu>2}$	$\bar{\Delta}^{\kappa}_{R/R_V}(\%)_{\nu>3}$
CMB-Lensing	-4	-1	-3
WL($z_s = 2$)	-30	-31	-32
Euclid photo-z	-29	-30	-30

Table 7.10: Mean values of $\Delta^{\kappa}_{R/R_V}(\%)$ (as defined Eq. (7.2)) for the voids κ profiles, for CMB-lensing, WL($z_s = 2$), and the Euclid lensing, for the three catalogs with κ-SNR thresholds $\nu > 1$, $\nu > 2$ and $\nu > 3$.

$\bar{\Delta}_{R/R_V}(\%)^{CMB}_{\nu>2} = -1\%$ and $\bar{\Delta}_{R/R_V}(\%)^{CMB}_{\nu>3} = -3\%$, with a spike correspondent to the point where κ from negative becomes positive for the $\nu > 2$ and $\nu > 3$ catalogs with $\Delta_{R/R_V}(\%)^{CMB}_{\nu>2,3} \sim 35\%$. These spikes highlight some statistical fluctuations between two even smaller values of the convergence field κ.

The other two lensing probes show, instead, some differences. In fact, the WL($z_s = 2$) and the Euclid map present important differences between the two scenarios for all the catalogs $\nu > 1$, $\nu > 2$ and $\nu > 3$, with $\bar{\Delta}_{R/R_V}(\%)^{Euclid,z_s}_{\nu>1,2,3} \sim -30\%$. We indeed expect the effects of free-streaming of massive neutrinos being more significant at lower redshifts where they are less relativistic. In fact the WL map with $z_s = 2$ and the Euclid-like map cover lower redshift ranges if compared to the CMB-lensing.

Furthermore, for all the probes, we see that the ΛCDM scenario is the one with more underdense voids, in fact if we see the values of $\Delta_{R/R_V}(\%)$ found for each R/R_V in Tab. B.6 are negative until κ are negative; when the values of the convergence become positive at $R = 0.75R_V$ the ΛCDM curves have a bigger over-dense boundaries and the values of $\Delta_{R/R_V}(\%)$ are again negative. If we take for example the WL($z_s = 2$) map, $\kappa^{WL(z_s=2)}_{\nu>1,max} = 0.0022$ in the ΛCDM cosmology, whereas $\kappa^{WL(z_s=2)}_{\nu>1,max} = 0.0021$ in the νΛCDM one.

Another thing that emerges from the plots in Fig. 7.8 is that even at larger values of the stacked radial distance R/R_V $\Delta(\%)$ differs a lot between the two cosmologies analyzed although the plots in the corresponding panel do not show the same behaviour. The values of the convergence κ differs from the νΛCDM and the ΛCDM scenarios, but these differences are not clearly visible because we are taking into account data of the order of $10^{-5} - 10^{-6}$.

Following the steps of the analysis of lensing voids in the ΛCDM cosmology, now it can be interesting to show the κ-profiles at different redshift ranges both in the ΛCDM cosmology and in the massive neutrino scenario. Our aim in this section is to highlight the main differences that arise in the presence of massive neutrinos and to analyse the evolutionary κ-profile of voids when we we place ourselves in a νΛCDM cosmology.

In Fig. 7.9 we show the convergence profiles associated to the two scenarios we are considering: the ΛCDM scenario with massless neutrinos and the νΛCDM scenario with massive neutrinos. All the sub-panels show instead the $\Delta(\%)$ in the two cosmologies.

Beside the expected behaviour of the κ-curves, that we recover also in this scenario, we want to underline what are the main differences between the convergence profiles in the two cosmology. In order to better quantify these differences we write in Tab. 7.11 the mean values of $\Delta_{R/R_V}(\%)$ found for all the redshift ranges in analysis, in Tab. B.7 and Tab. B.8 we insert the single values of $\Delta_{R/R_V}(\%)$ found for each R/R_V.

The flat-sky patches containing information about the convergence field in the redshift range $19 < z < 99$ shows a quasi total overlap with $\bar{\Delta}_{R/R_V}(\%)_{\nu>1} = -3\%$ and $\bar{\Delta}_{R/R_V}(\%)_{\nu>2}$=-1%, although for big values R/R_V values we see some deviations between the two scenarios for the catalog $\nu > 3$, that is the one that contains the less number of voids and the more rich in overdensities due to its higher threshold. For what concerns the map in the $12 < z < 15$ redshift range the deviations between the two cosmologies are still small ($\bar{\Delta}_{R/R_V}(\%)_{\nu>1} = -3\%$ and $\bar{\Delta}_{R/R_V}(\%)_{\nu>2} = -3\%$); again, for the $\nu > 3$ catalog, we see an oscillatory trend of $\Delta_{R/R_V}(\%)$,

z_i	$\bar{\Delta}^{\kappa}_{R/R_V}(\%)_{\nu>1}$	$\bar{\Delta}^{\kappa}_{R/R_V}(\%)_{\nu>2}$	$\bar{\Delta}^{\kappa}_{R/R_V}(\%)_{\nu>3}$
$19 < z < 99$	-3	-1	15
$12 < z < 15$	-3	-3	5
$5 < z < 11$	5	1	32
$2.5 < z < 4$	-3	-2	8
$1 < z < 2$	11	5	6
$0.5 < z < 1$	-14	-10	-11

Table 7.11: Mean values of $\Delta^{\kappa}_{R/R_V}(\%)$ (as defined Eq. (7.2)) for void κ profiles extracted from the catalogs of the partial CMB-lensing maps in different redshifts bins with κ-SNR thresholds: $\nu > 1$, $\nu > 2$ and $\nu > 3$.

we can think that the differences might be caused by the intrinsic nature of the catalog. The differences between the massive and massless neutrino scenarios start being more visible below the redshift $2.5 < z < 4$.

We can see that as the redshift ranges of our maps decrease, the differences between the two cosmologies become slightly more visible, especially for the catalogs $\nu > 1$ and $\nu > 2$, although they are still very small; for small radii, the ΛCDM case has a slightly bigger $\kappa_{\rm min}$ with respect to the values of the minimum of the convergence κ found in the $\nu\Lambda$CDM cosmologies as already seen for the three probes in Fig. 7.8.

7.4 Void shear profile in the $\nu\Lambda$CDM scenario

The last step in our analysis of lensing voids with peak statistics is the study of the stacked tangential shear profiles of the same lensing voids both for different probes and for maps at different redshift ranges with the purpose of identifying the main differences with respect to the massless neutrino scenario.

We calculate the tangential shear profile of voids $\gamma_t(r)$ from the convergence profile using the same equation of the previous Chapter Eq. (7.3) (Davies et al., 2018):

$$\gamma_t(r) = \bar{\kappa}(< r) - \kappa(r), \tag{7.3}$$

where $\kappa(r)$ corresponds to the value of the convergence profile at the radial distance r and $\bar{\kappa}(< r)$ is the mean enclosed convergence within r. As for the convergence profile we average over all the sections we have divided the original full-sky maps into in order to have better statistics.

In Fig. 7.10 it is possible to see the plots of the stacked tangential shear profiles of the three probes (CMB-lensing, WL($z_s = 2$) and map Euclid-like) for the usual thresholds in the top-left panel, the other panels show the stacked tangential shear profile of each lensing map with a sub-panel associated of the $\Delta_{R/R_V}(\%)$ between the ΛCDM and the $\nu\Lambda$CDM cosmology, with $\Delta(\%)$ being calculated via Eq. (7.2).

It can be interesting to notice that, following the correspondent κ-profiles of Fig. 7.8, the CMB-lensing γ_t-profile shows very small discrepancies between the two scenarios; whereas the effects of the presence of massive neutrinos are visible for the WL map with $z_s = 2$ and for the Euclid-like redshift distribution map.

From a quantitative point of view, the mean differences between the two cosmologies of the three probes are inserted in Tab. 7.12; Tab. B.9, instead, contains all the $\Delta_{R/R_V}(\%)$ for each value of the stacked radial distance R/R_V .

We see that, beside some random spikes, the cosmology with massless neutrinos present bigger negative value of the tangential shear, in fact almost all the values of $\Delta_{R/R_V}(\%)(\%)$ are negative, especially for the catalogs $\nu > 1$ and $\nu > 3$.

	$\bar{\Delta}^{\gamma}_{\mathrm{R/R_V}}(\%)_{\nu>1}$	$\bar{\Delta}^{\gamma}_{\mathrm{R/R_V}}(\%)_{\nu>2}$	$\bar{\Delta}^{\gamma}_{\mathrm{R/R_V}}(\%)_{\nu>3}$
CMB-Lensing	-4	-4	3
WL(z_s = 2)	-30	-31	-33
Euclid photo-z	-29	-30	-26

Table 7.12: Mean values of $\Delta^{\gamma}_{\mathrm{R/R_V}}(\%)$ (as defined Eq. (7.2)) of the stacked tangential shear of the CMB-lensing map, the WL(z_s = 2) map and the Euclid-like redshift distribution map for the three catalogs $\nu > 1$, $\nu > 2$ and $\nu > 3$.

The two lensing maps that show the major evidences are the WL(z_s = 2) and the Euclid-like redshift maps, both have a $\Delta_{\mathrm{R/R_V}}(\%) \sim -30\%$ for all the thresholds. The CMB-lensing map, as major fluctuations in $\gamma_t(r)$, however the differences between the two scenarios are very difficult to identify and lay in the error bars. Now, similarly to what we have done in the previous section, we want to see how the stacked tangential shear profiles of lensing voids evolve at different redshifts z. We plot these γ_t-profiles in Fig. 7.11.

Two are the main things we notice from this plot. First of all the behaviour of the curves in the case of massive neutrinos is similar to the behaviour of the correspondent curves in the ΛCDM cosmology: as the redshift we are looking at decreases, also the absolute value of the maximum γ_t increases, as we expect if we think to the evolutionary history of cosmic voids. Moreover these curves show relatively small discrepancies with respect to the ones of the massless neutrino scenario. If for the κ-profiles we have found $\Delta(\%) \sim -30\%$, for the tangential shear profile $\Delta(\%) \sim -(5-6)\%$ for the lensing maps at lower redshifts as it can be seen in Tab. 7.13.

z_i	$\bar{\Delta}^{\gamma}_{R/R_V}(\%)_{\nu>1}$	$\bar{\Delta}^{\gamma}_{R/R_V}(\%)_{\nu>2}$	$\bar{\Delta}^{\gamma}_{R/R_V}(\%)_{\nu>3}$
$19 < z < 99$	-0.5	-3	28
$12 < z < 15$	-3	-3	80
$5 < z < 11$	-3	-9	-37
$2.5 < z < 4$	-5	-8	-2
$1 < z < 2$	-4	-4	-9
$0.5 < z < 1$	-4	-8	10

Table 7.13: Mean values of $\Delta^{\gamma}_{\mathrm{R/R_V}}(\%)$ (as defined in Eq. (7.1)) mean of the tangential shear of lensing maps z_1, z_2, z_3, z_4, z_5 and z_6 for the catalogs $\nu > 1$, $\nu > 2$ and $\nu > 3$.

7.5 Summary of Chapter 7

In this Chapter we present quantitative results obtained from the analysis of cosmic voids in the $\nu\Lambda$CDM model, and identify the differences between the massless and massive neutrino cases.

We have considered the three probes with different redshift distributions: CMB-lensing, WL(z_s=2), and the Euclid-lensing, all full-sky for simplicity.

Using CMB-lensing partial catalogs in redshifts bins $19 < z_1 < 99$, $12 < z_2 < 15$, $5 < z_3 < 11$, $2.5 < z_4 < 4$, $1 < z_5 < 2$ and $0.5 < z_6 < 1$, we study also how the evolution of κ counts, as well as of void counts and profiles changes in the presence of massive neutrinos.

From each map we have, again, identified three different catalogues imposing three κ-SNR thresholds ν_{cut}: $\nu > 1$, $\nu > 2$ and $\nu > 3$.

In particular, first we have recovered the behaviour of the mean cumulative projected density of κ-peaks as function of the signal to noise ratio $\nu = \kappa/\sigma$. We have computed for each probe

the values of the percent residuals $\Delta(\%)$, that highlight the differences between the two cosmological scenarios considered in this work. We observe that the cumulative projected density of convergence peaks presents the same behavior as for the massless neutrino case.

Interestingly, when we inspect catalogs with large values of the signal to noise ratio ν, we observe how massive neutrinos smooth out the perturbations on the convergence field and make higher ν peaks rarer.

The same happens when we analyze the partial CMB-lensing catalogs as a function of redshifts. As expected, we observe the main differences at low redshift, although they are only few %, given the small neutrino mass considered in this work, $M_\nu = 0.16$ eV.

Then, we have build void catalogs applying the 2D tunnel finding algorithm to the κ-peak catalogs used as void tracers.

We notice how the total number of voids in each catalog changes with the value of the radius R_V and how, for high SNR thresholds, and low z, the total number of voids, N_V, as a function of the void radius, increases as with decreasing redshift. However, considering the difference with respect to the massless neutrino case, we can observe that N_V decreases for fixed radius, and this is explained by structure suppression due to free streaming neutrinos, especially at low redshifts.

Finally we have studied the behavior of the stacked void convergence profile, κ, and the stacked void tangential shear profile γ_t, as a function of the stacked radial distance R/R_V.

For the three probes we have recovered also in this different model that the Euclid-lensing and the WL(z_s=2) void catalogs have a very similar trend between the two, whereas the CMB-lensing catalog shows larger fluctuations in the convergence profiles, and in the tangential shear profiles as well.

Moreover we have found that, even if the CMB-lensing profiles do not show significant variations in the convergence and shear profiles between the massless and massive neutrino scenarios, for the low redshift lensing probes, void profiles tend to be much less under-dense at the depth, especially for large thresholds values. This can be related to the presence of massive neutrinos, suppressing structure formation especially at low redshifts (where they are non relativistic) and at nonlinear scales. The same effect can be seen on the boundaries of these voids, where massive νs make the accumulation of matter on the walls smoother, as expected. When we take into account the partial CMB-lensing catalogs at different redshifts, we observe that, as expected in the $\nu\Lambda$CDM scenario, the redshift evolution of lensing voids is similar to the ΛCDM case. However, we can notice that, at lower redshifts, the smoothing effect due to the presence of neutrinos is more evident, as expected.

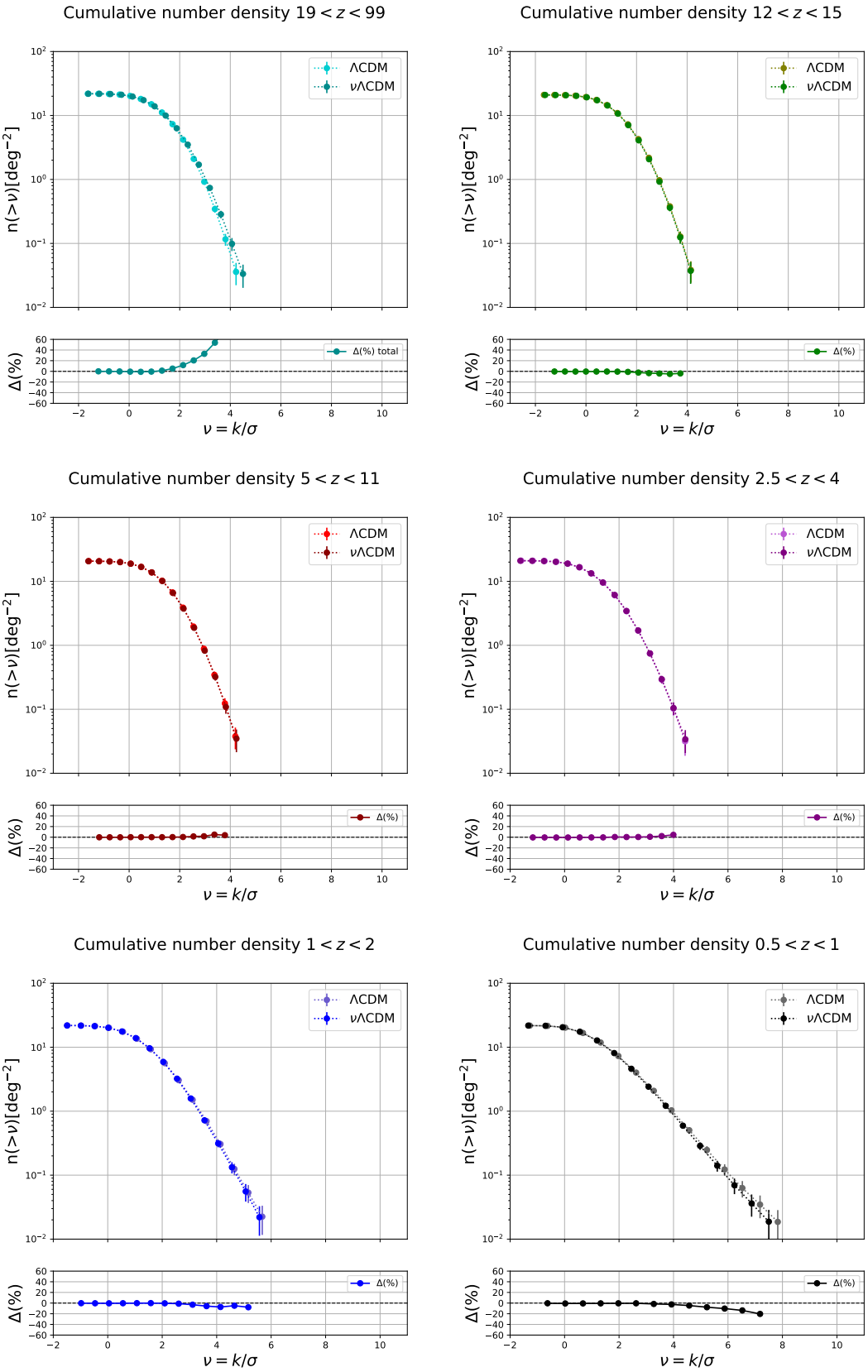

Figure 7.3: Cumulative projected density of convergence peaks as a function of $\nu = \kappa/\sigma$ in the $\nu\Lambda$CDM cosmology for the partial CMB-lensing convergence maps in the redshift bins: $19 < z < 99$, $12 < z < 15$, $5 < z < 11$, $2.5 < z < 4$, $1 < z < 2$ and $0.5 < z < 1$. The sub-panels show the $\Delta_\nu(\%)$ (as defined in Eq. (7.1)) of the the projected density between the $\nu\Lambda$CDM scenario and the ΛCDM one.

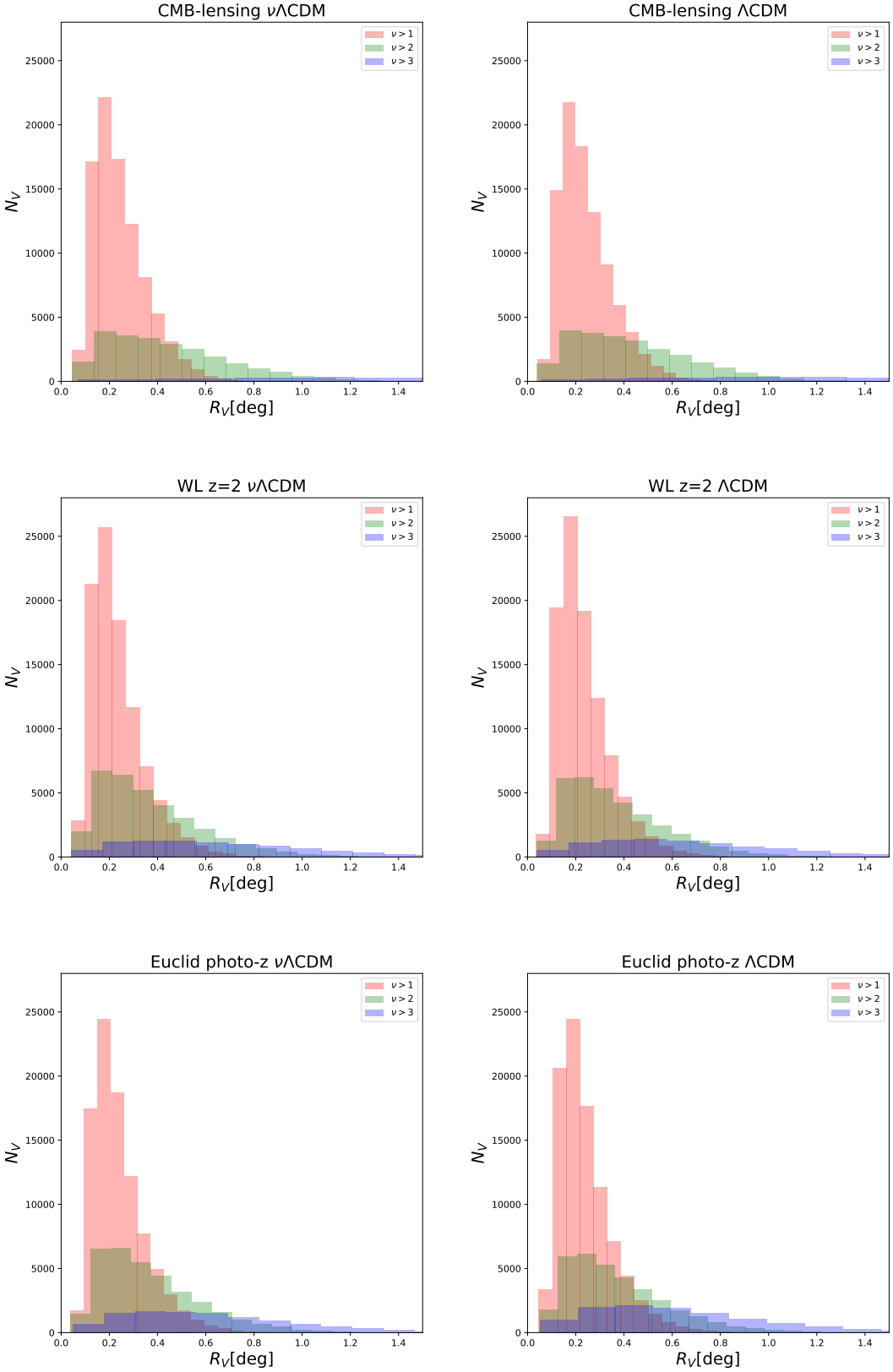

Figure 7.4: LEFT panels: histogram of the total number of voids as a function of their radius R_V for the CMB-lensing, the WL ($z_s = 2$), and the Euclid lensing void catalogs in the $\nu\Lambda$CDM cosmology. RIGHT panels: the same as in the left panels, but in the massless neutrino scenario. In all cases we consider the κ-peak catalogs with SNR thresholds: $\nu > 1$, $\nu > 2$, $\nu > 3$, shown as different color bars (red, green, and blue respectively).

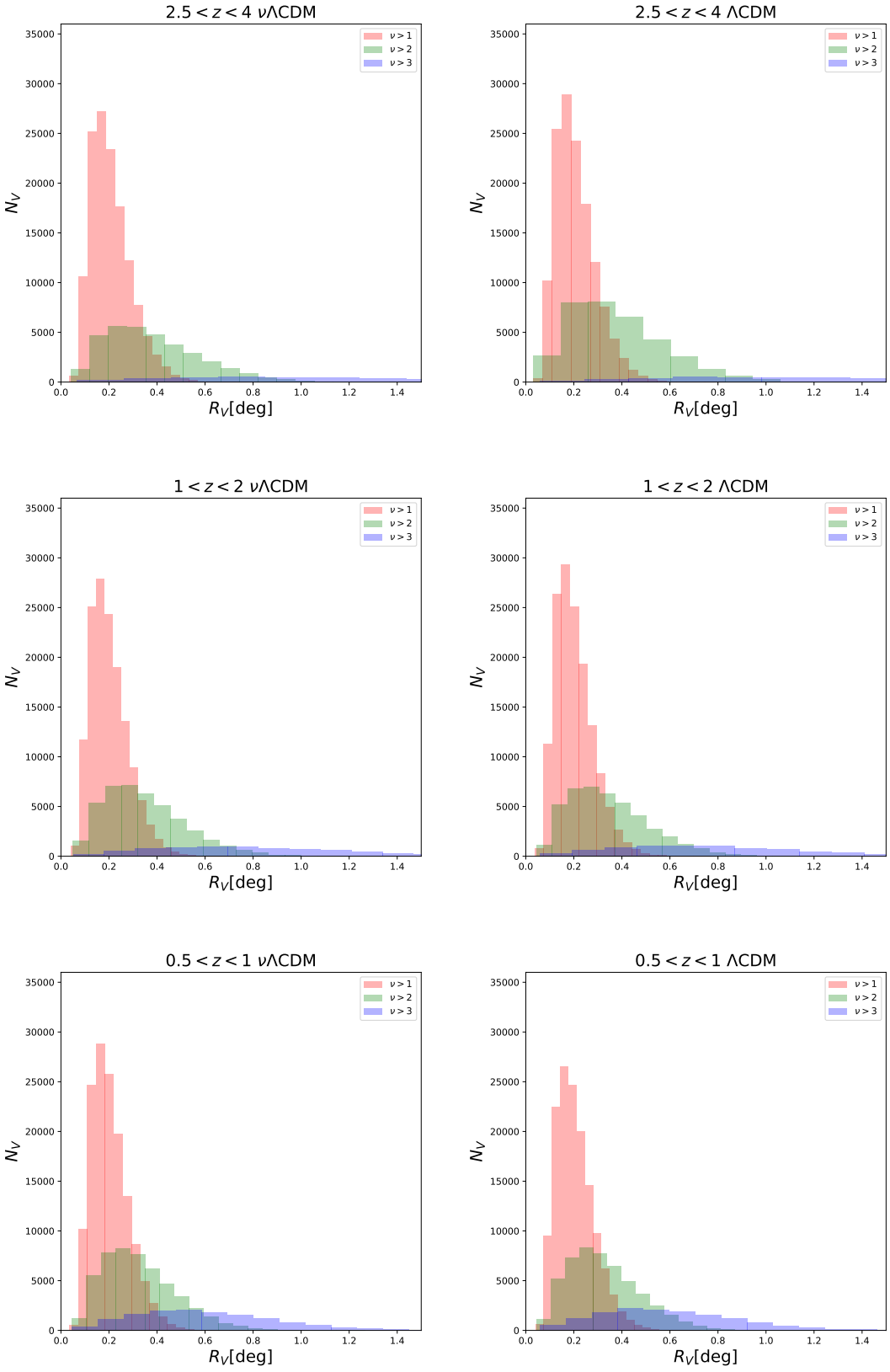

Figure 7.5: Number of voids as a function of their radius R_V at different redshift bins in the $\nu\Lambda$CDM (LEFT panels) and ΛCDM (RIGHT panels) cosmologies from CMB-lensing partial catalogs in the redshift bins defined in Tab. 7.1. Color bars are the same as Fig. 7.4.

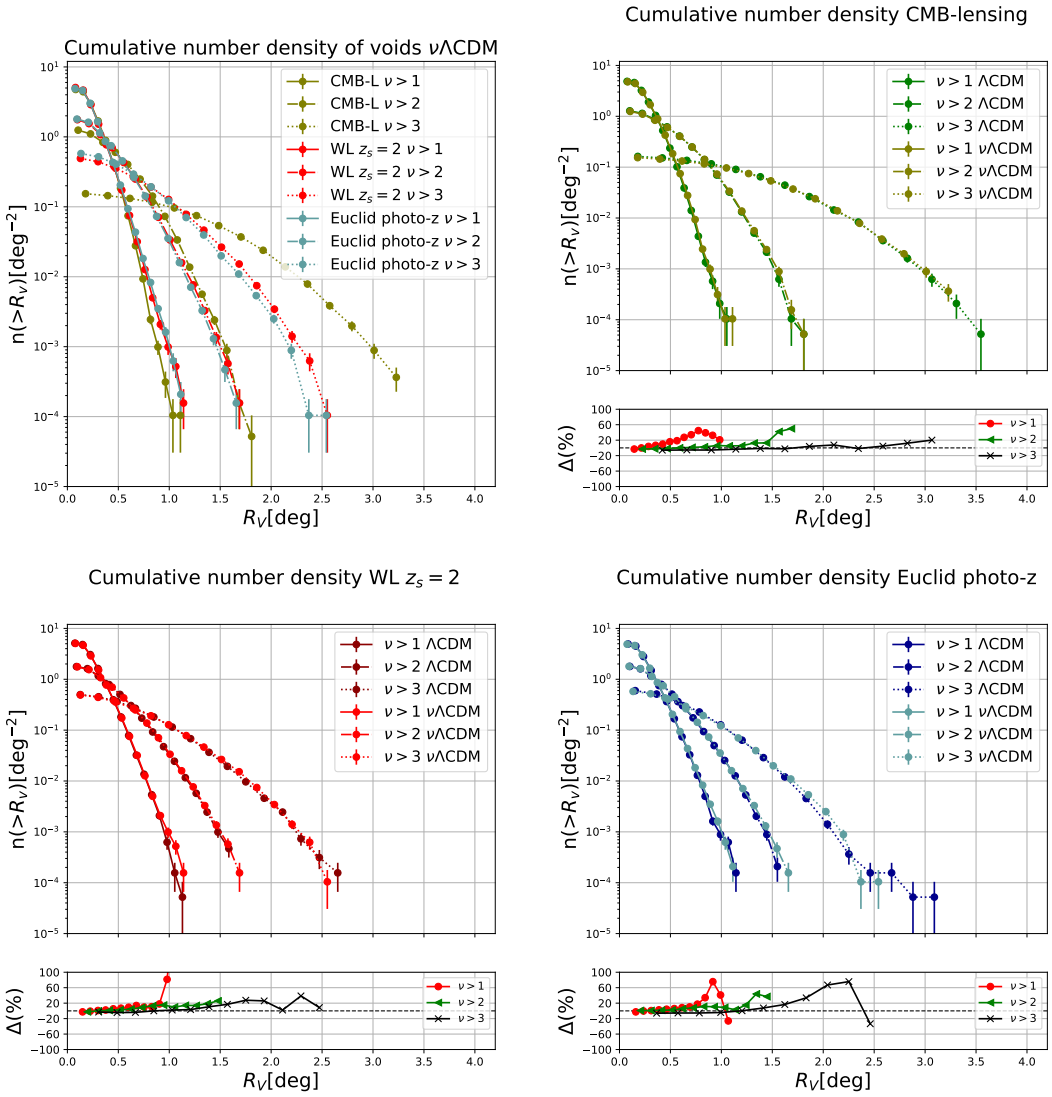

Figure 7.6: TOP-LEFT: Cumulative projected density of voids from the CMB-lensing map (olive), the WL map($z_s = 2$) (red) and the lensing map with Euclid-like redshift distribution (blue) in the $\nu\Lambda$CDM cosmology. Different line-styles correspond to different void catalogs identified in this work: $\nu > 1$ (solid), $\nu > 2$ (dash-dotted), $\nu > 3$ (dotted). TOP-RIGHT: Cumulative projected density of lensing voids as function of their radius R_V for the CMB-lensing map; the sub-panel shows the $\Delta(\%)$ between the $\nu\Lambda$CDM scenario and the ΛCDM one for the three catalogs analyzed. BOTTOM-LEFT: Cumulative projected density of voids as function of their radius R_V for the WL($z_s = 2$) map; the sub-panel shows the $\Delta(\%)$ between the $\nu\Lambda$CDM scenario and the ΛCDM one for the three catalogs analyzed. BOTTOM-RIGHT: Cumulative projected density of voids as function of their radius R_V for the lensing map with Euclid-like redshift distribution; the sub-panel shows the $\Delta(\%)$ between the $\nu\Lambda$CDM scenario and the ΛCDM one for the three catalogs analyzed. $\Delta(\%)$ are defined in Eq. (7.1).

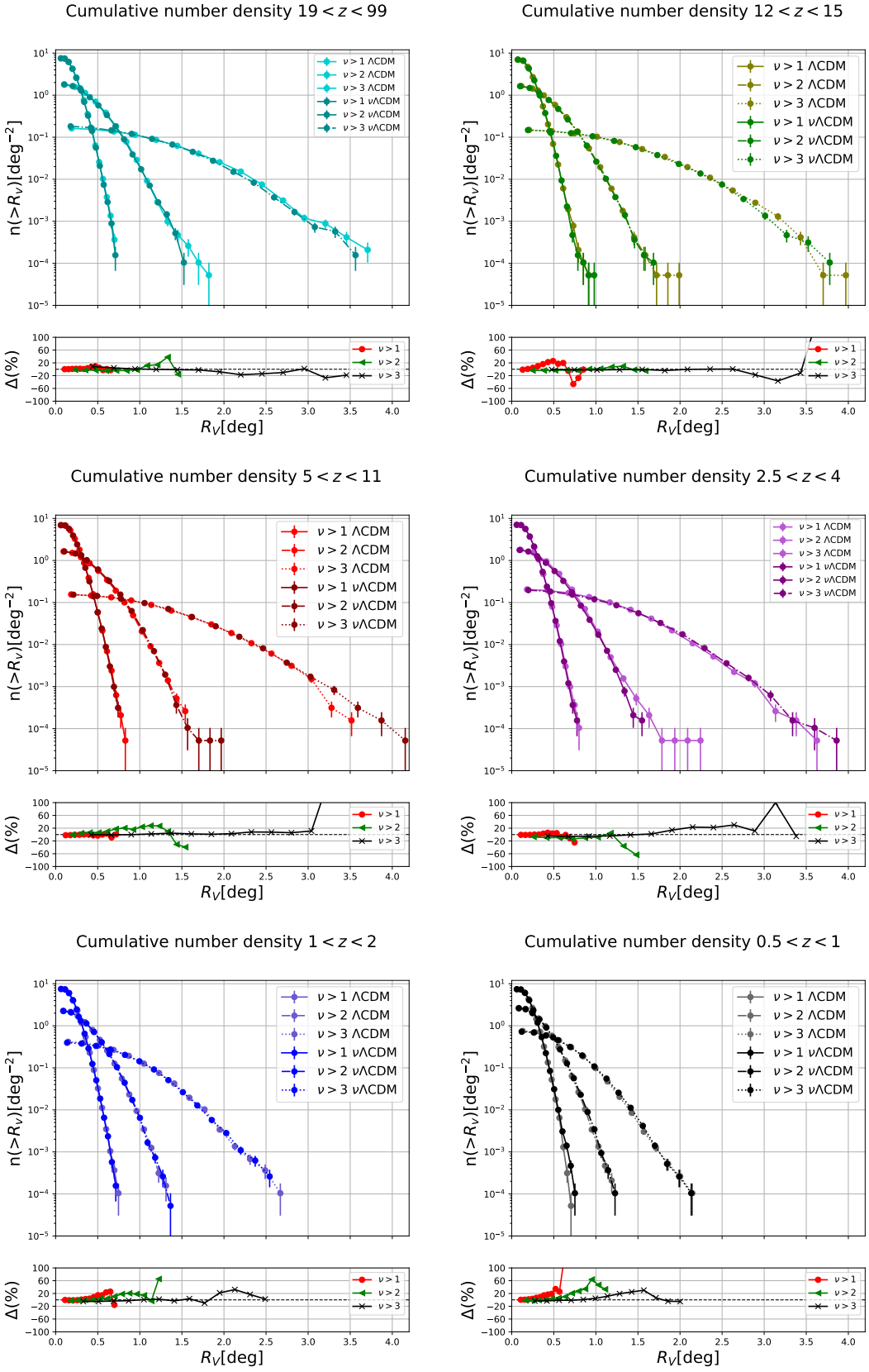

Figure 7.7: Cumulative projected density of lensing voids as a function of their radius R_V for CMB-lensing maps at different redshift ranges. We show both the curves of the ΛCDM cosmology and the ones of the $\nu\Lambda$CDM cosmology for the three void catalogs identified in this work: $\nu > 1$, $\nu > 2$ and $\nu > 3$. The sub-panels show the $\Delta(\%)$ as defined in Eq. (7.1) between the massive and massless neutrino scenarios.

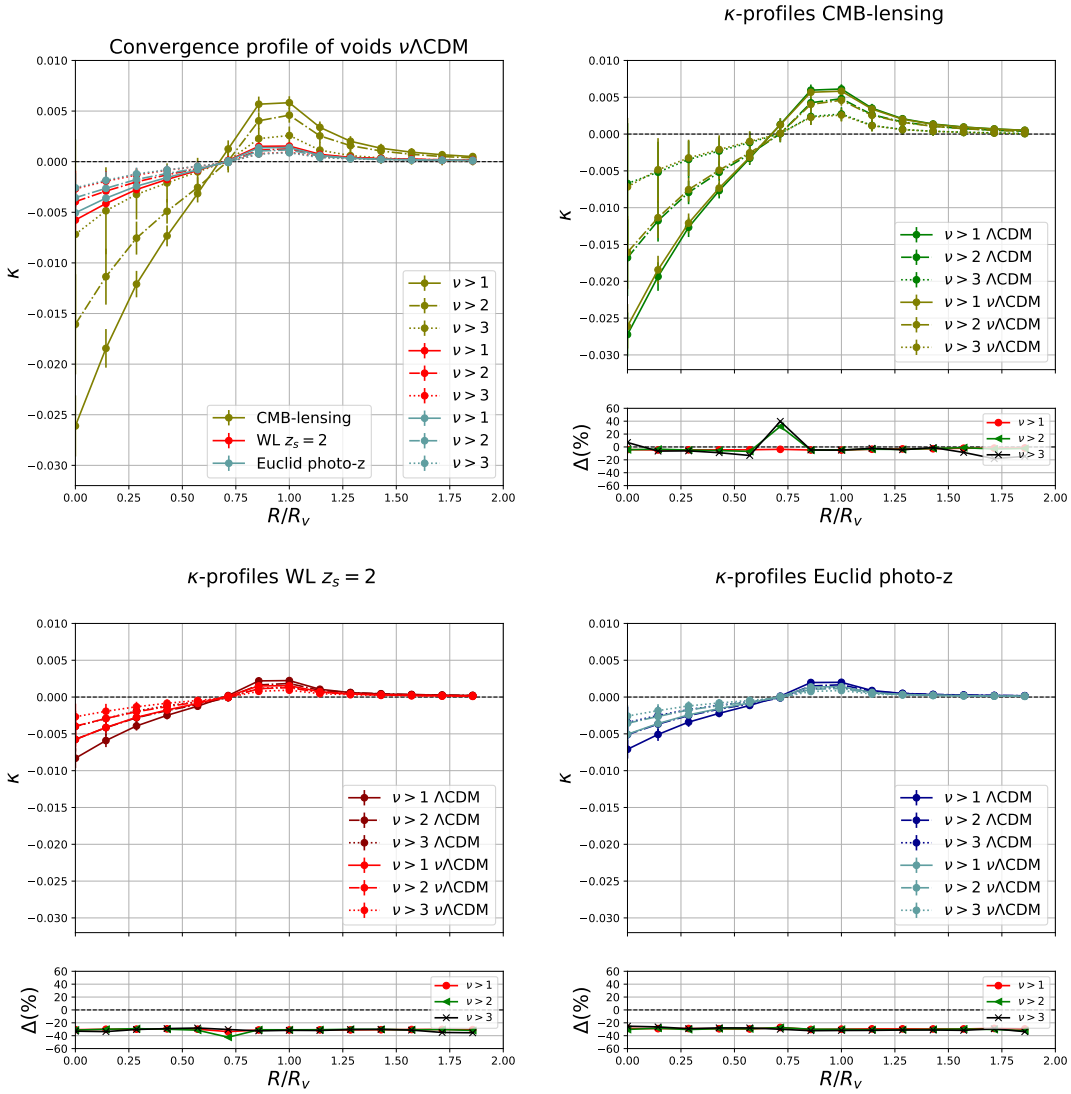

Figure 7.8: TOP-LEFT: Stacked convergence profile of voids from the CMB-lensing map (olive), the WL map with $z_s = 2$ (red) and the lensing map with Euclid redshift distribution (blue) in the $\nu\Lambda$CDM cosmology. Each curve is averaged over all of the voids found in each of the sections we have projected the original full-sky maps into. Different line-styles correspond to different void catalogs identified in this work: $\nu > 1$ (solid), $\nu > 2$ (dash-dotted), $\nu > 3$ (dotted). TOP-RIGHT: Stacked convergence profile of voids for CMB-lensing map; the sub-panel shows the $\Delta(\%)$ between the convergence κ in the $\nu\Lambda$CDM scenario and the ΛCDM one. BOTTOM-LEFT: Stacked convergence profile of voids for WL map $z_s = 2$; the sub-panel shows the $\Delta(\%)$ between the convergence κ in the $\nu\Lambda$CDM and the ΛCDM cosmologies. BOTTOM-RIGHT: Stacked convergence profile of voids for lensing map with Euclid redshift distribution; the sub-panel shows the $\Delta(\%)$ between the convergCDM scenario and the ΛCDM cosmology. Note that in all sub-panels $\Delta(\%)$ are defined in Eq. 7.2. Error bars in all profiles are the variance of each bin in radius w.r.t. all the voids found in our flat sections.

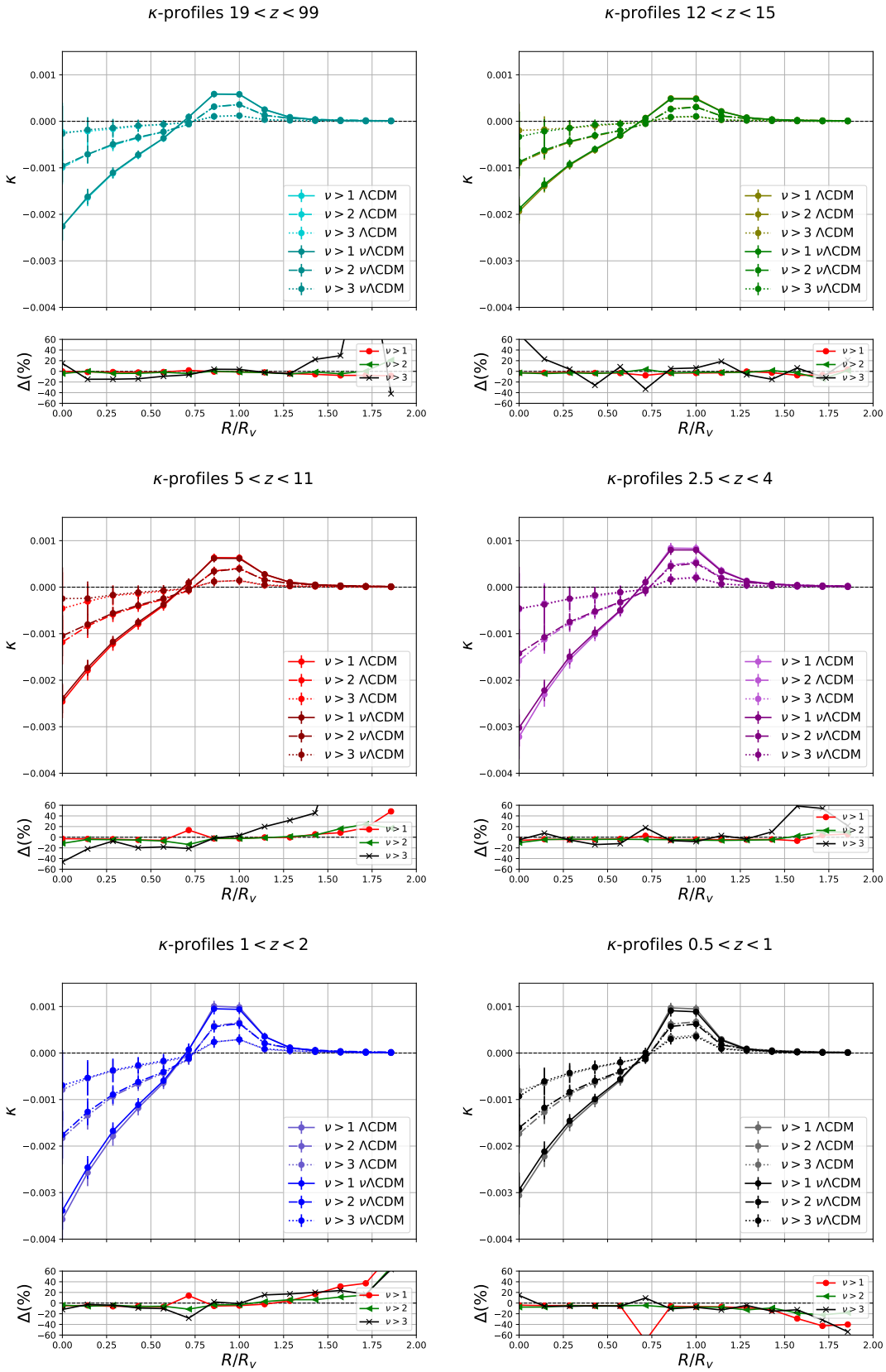

Figure 7.9: Stacked convergence profiles of lensing voids averaged over all the voids found in CMB-lensing map at different redshift ranges as a function of the scaled radial distance $R/R_{\rm V}$ both in the ΛCDM scenario and in the νΛCDM one for the three void catalogs $\nu > 1$, $\nu > 2$ and $\nu > 3$. The sub-panels show the $\Delta^{\kappa}_{R/R_{\rm V}}(\%)$ (see Eq. 7.2) between the κ-values in the νΛCDM cosmology and the ΛCDM one. Error bars in all profiles are the variance of each bin in radius w.r.t. all the voids found in our flat sections.

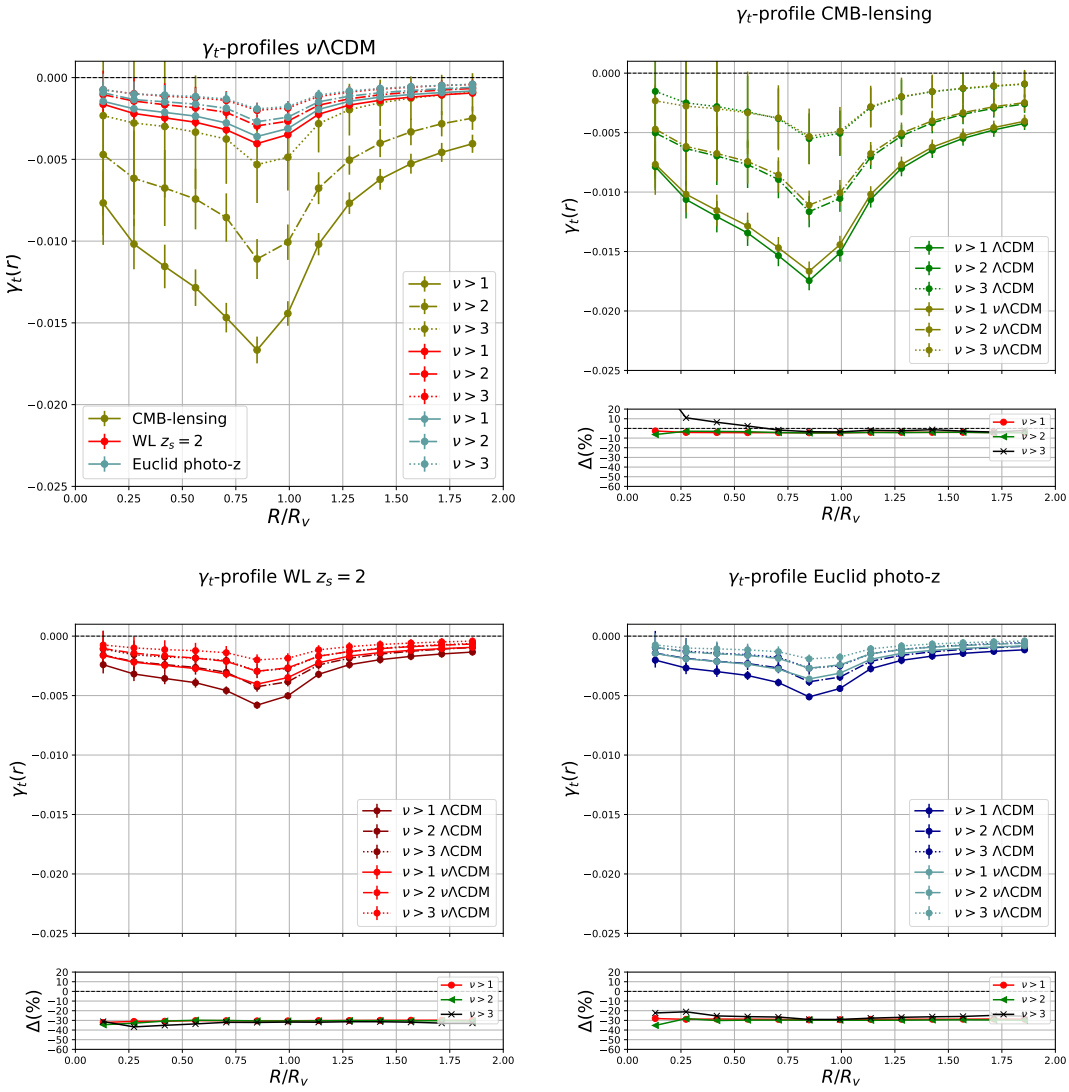

Figure 7.10: TOP-LEFT: Stacked tangential profile of voids from the CMB-lensing map, the WL map with $z_s = 2$ and the lensing map with Euclid redshift distribution in the $\nu\Lambda$CDM cosmology. Each curve is averaged over all of the voids found in each of the sections we have projected the original full-sky maps into. Different line styles correspond to different voids catalogs: $\nu > 1$ (solid), $\nu > 2$ (dash-dotted), $\nu > 3$ (dotted). TOP-RIGHT: Stacked convergence profile of voids for CMB-lensing; the sub-panel shows the $\Delta^{\gamma}_{R/R_V}(\%)$ between the tangential shear γ_t in the $\nu\Lambda$CDM scenario and the ΛCDM cosmology. BOTTOM-LEFT: Stacked tangential shear profile of voids for WL map $z_s = 2$; the sub-panel shows the $\Delta^{\gamma}_{R/R_V}(\%)$ between the tangential shear γ_t in the $\nu\Lambda$CDM scenario and the ΛCDM cosmology. BOTTOM-RIGHT: Stacked tangential shear profile of voids for lensing map with Euclid redshift distribution; the sub-panel shows the $\Delta^{\gamma}_{R/R_V}(\%)$ between the tangential shear γ_t in the $\nu\Lambda$CDM scenario and the ΛCDM cosmology. Error bars in all profiles are the variance of each bin in radius w.r.t. all the voids found in our flat sections.

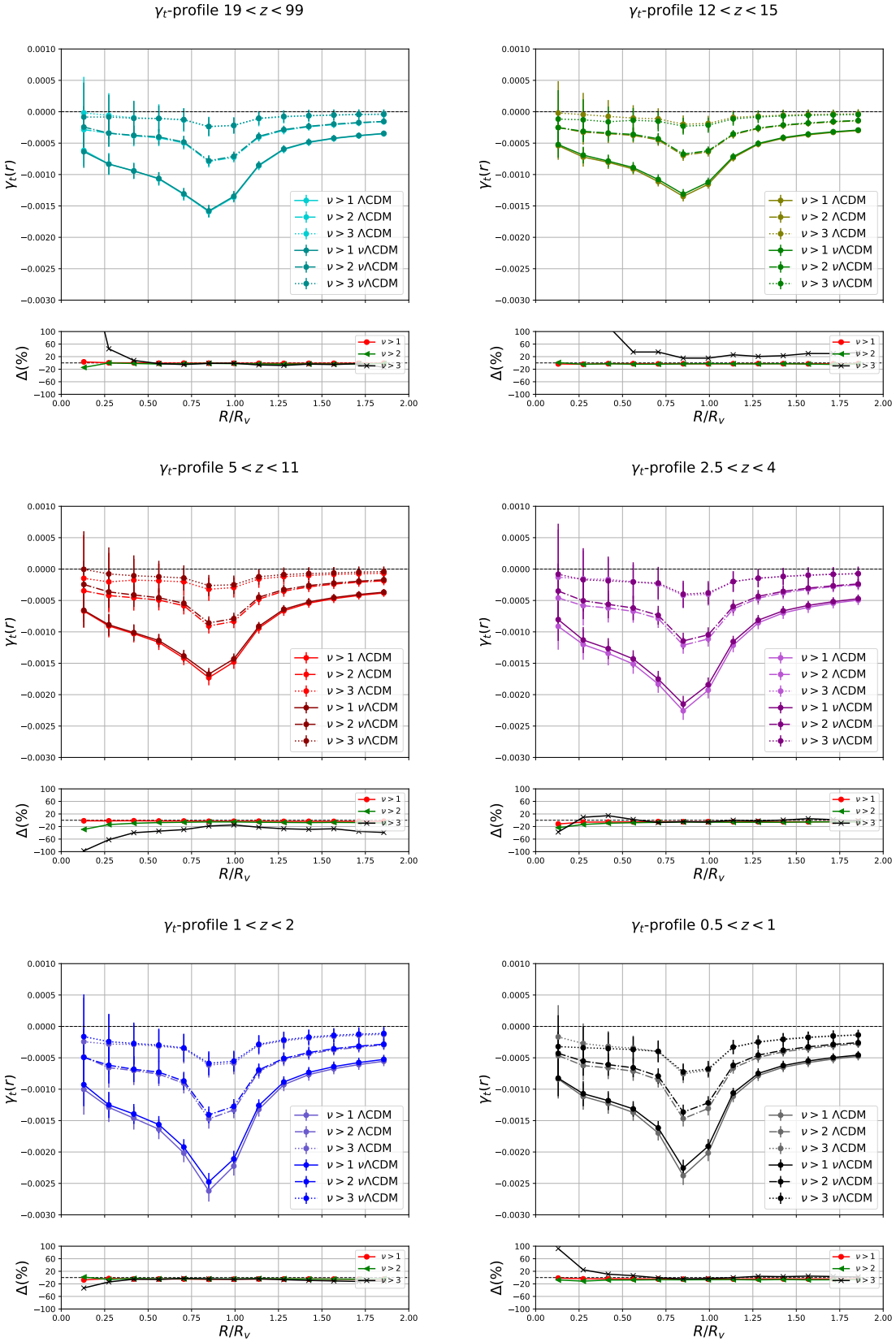

Figure 7.11: The stacked tangential shear profiles of lensing voids found in convergence maps in the ΛCDM and the νΛCDM scenario. The coloured lines show the average profile for the void catalogs used in this work $\nu > 1$, $\nu > 2$ and $\nu > 3$ at different redshift ranges. The sub-panels show the $\Delta^{\gamma}_{\mathrm{R/R_V}}(\%)$ between the γ_{t}-values in the νΛCDM cosmology and the ΛCDM one. The shaded regions instead show the mean uncertainties.

Conclusions

In this thesis we have analyzed the properties of cosmic voids, focusing on the voids identified from lensing convergence maps, the so-called VOLEs (VOids from LEnsing). From a theoretical point of view, voids are under-dense regions of the Mpc scale Universe. It is this peculiar characteristic that makes them unique probes for cosmological parameters (Hamaus et al., 2016) as dark energy and massive neutrinos (Pisani et al., 2015)).

Voids can be identified as under-densities of the matter field using galaxies as tracers (Nadathur et al., 2017); however, other methods have been developed in the literature to find voids. In particular, in this thesis we have adopted the so-called κ-peak statistics, where first peaks are identified in the convergence field, and then they are used as void tracers applying a particular void finder, which identifies voids as regions devoid of κ peaks above a certain SNR threshold. The identidied voids are therefore lensing voids.

In this thesis we study the convergence field directly, being the convergence field the projected line-of-sight density field weighted by the lensing kernel (Davies et al., 2018). Therefore lensing voids are simply under-density regions in the projected matter density field.

In particular, we have analyzed the statistical properties of lensing voids, considering two different cosmological scenarios: the standard ΛCDM cosmology with massless neutrinos, and the $\nu\Lambda$CDM one with massive ν, of total mass $M_\nu = \sum m_\nu$=0.16 eV. We have also considered three different lensing probes, characterized by different source redshift distributions: CMB-lensing, WL($z_s = 2$), and convergence maps characterized by a Euclid photometric redshift distribution of galaxies. For semplicity, all the probes are considered full-sky.

We have also studied the evolution with redshift of κ counts, as well as void counts. Finally, we have analyzed how these properties change when we consider the case massive neutrinos. In this part of the analysis we have observed how the effects of massive neutrinos start to be visible at low redshifts, as expected since at such redshifts they are non relativistic and their free streaming suppress structure formation, especially at nonlinear scales.

In this work, we have shown the properties of lensing voids, starting from the DEMNUNi set of cosmological simulations (Carbone et al., 2016) and the lensing maps obtained via direct ray-tracing across their dark matter distribution as provided by the Lens2Hat code (Calabrese et al., 2015; Fabbian et al., 2018; Hilbert et al., 2020). We have applied to these full-sky simulated convergence maps the 2D tunnel-finding algorithm adapted by (Cautun et al., 2018) in order to look for lensing voids within the convergence field via the κ peak statistics.

Since the 2D void finder works with lensing maps in the flat-sky approximation, we have projected the full-sky DEMNUni maps onto a two-dimensional Cartesian plane, partitioning the original full-sky maps into 192 $10x10$ deg^2 patches, using the partitioning algorithm described by (Davies et al., 2019). These 192 flat-sky sections were the starting point of our analysis.

We have investigated the cumulative projected density distribution of κ-peaks as a function of the SNR $\nu = \kappa/\sigma$, identified in our catalogs. These distributions show the expected decrease as the signal to noise ratio $\nu = \kappa/\sigma$ increases, with a flattening of the curves at negative values of ν. Moreover, we have found that probes at lower redshifts have associated peaks with much larger signal to noise ratio. This can be related to the fact that weak lensing at low redshifts is much more affected by non-linear structure evolution with respect to CMB-lensing.

A similar behaviour has been recovered from the partial CMB-lensing maps representing lens

regions in different redshift bins.

As a next step, we have produced three peak catalogs imposing several thresholds on SNR $\nu_{\rm cut} = 1, 2, 3$. This allows us to discriminate the different properties of voids as we select specific amplitudes of matter perturbations in the convergence field.

We compute the histograms of the void number, $N_{\rm V}$, identified in the full-sky catalogs, as a function of their radius $R_{\rm V}$. In this case, we observe that the number of voids for the catalogs with $\nu > 2$ and $\nu > 3$ increases at lower redshifts, highlighting the effective evolution of such voids.

The void cumulative projected density shows a similar behavior, with voids of larger size being fewer than smaller voids, as expected given the corresponding trend in the κ projected densities. In particular, when we compare the three probes, we see how the CMB-lensing catalogs differ, by more than one order of magnitude, from the other two in the case of $\nu > 3$, which corresponds to very large voids. This is related to the fact that in the CMB-lensing catalogs the convergence peaks with $\nu > 3$ are much rarer if compared to what we can find for the other observables, then the identified voids are much larger and more numerous with respect to the other probes.

Next, we have analysed the stacked void convergence profiles κ and the shear profiles $\gamma_{\rm t}$, as function of the radial distance $R/R_{\rm V}$.

Inspecting the stacked profiles of lensing voids at different redshifts we can recover what we expect: at lower redshifts, voids seem to be much more under-dense (i.e. with a larger depth) whereas on their boundaries we find much more structures (i.e. higher walls at their boundary). This is evidence of an effective evolution of our lensing voids.

Then, we have performed the same analysis on cosmic voids in the case of the $\nu\Lambda$CDM, to compare how the properties of lensing voids change when we consider massive neutrinos, and how the free-streaming of these massive particles influences their evolution with redshift.

We have found that these massive particles smooth out the perturbations in the convergence field; thus, in the cumulative projected density of convergence peaks, we have recovered that the ΛCDM model has a larger number of κ-peaks with higher signal to noise ratio with respect to the model with massive neutrinos. Obviously, this is more visible at low redshifts.

The fact that the convergence maps in the $\nu\Lambda$CDM model have fewer peaks with high signal to noise ratio explains how the total number of lensing voids changes in the presence of massive neutrinos: in fact, we have observed that catalogs with $\nu > 2$ and $\nu > 3$ have a smaller number of voids with respect to the corresponding ΛCDM case.

Finally, from the stacked void convergence profiles, κ, and tangential shear profiles, $\gamma_{\rm t}$, in the presence of massive neutrinos we have inferred that the effect of massive neutrinos consists of a smoothing of the perturbations of the convergence field: voids seem to be much less under-dense with respect to the massless neutrino case at their depth and, at the same time, they presents smaller walls.

Generally speaking, when we consider partial CMB-lensing catalogs at different redshifts, the effects of massive neutrinos starts being observable at $z \sim 1 - 2$, even if differences with respect to the massless neutrino case are only few %, due to the low value of neutrino mass considered.

Further works will investigate how these effect change whit the total neutrino mass M_ν, which in cosmologies more general than the ΛCDM one, can assume larger values than the one considered in this work.

Appendix A

Check of κ-profiles in the ΛCDM scenario

In the analysis of the lensing voids and their properties we have done several checks on convergence profiles of maps in the ΛCDM cosmology to explain the presence of the concavity that affects all the profiles as they approach the center of the voids. In particular, we have computed several κprofiles using different values of the resolution $N_{\rm side}$ associated to the projected square patches. Having chosen the value of $N_{\rm side}$ for the flat-sky patches that suits our data (that is the one that maintain the same resolution of the full-sky maps), we have selected different values of $R_{\rm V}$ and checked how the concavity of the κ-profiles changes as we impose a selection criterion on the radius as well.

A.1 κ-profiles for different $N_{\rm side}$

First, in the analysis of lensing voids in the ΛCDM cosmology, we have projected the full-sky maps on a 2-dimensional plane and we have created flat-sky square patches with an $N_{\rm side}$ of (4096x4096) pixel. All of the full-sky maps used in this thesis are characterized by a

$$N_{\rm side} = 2^{N_{\rm res}}, \tag{A.1}$$

with $N_{\rm res} = 12$, this means that the $N_{\rm side}$ associated to our maps is $N_{\rm side}$=4096.

In the procedure of projecting the full-sky maps on to a plane and then extrapolating our square sections, we have maintained a resolution of (4096,4096) pixel. The κ-profiles that we obtain with an $N_{\rm side} = 4096$ in the case of the CMB-lensing and the WL($z_{\rm s} = 2$) are shown in Fig. A.1. We see clearly the presence of a concavity at small values of $R/R_{\rm V}$, that correspond to radial points that are inside the actual radius $R_{\rm V}$ of the void, especially for the catalog $\nu > 1$. From a physical point of view, the presence of this inflection point seems to imply that the lensing voids we have found in our maps are still fixed *basins*, however if we extrapolate their asymptotic behaviour, it seems to go toward infinitely negative values of κ.

First of all we have that a resolution of (4096x4096) for our projected sections that is higher than the actual resolution of the original full-sky map. This is the reason why we have decided to proceed with the analysis of the κ-profiles associated to the same maps, but starting from different values of $N_{\rm side}$ for our flat square patches. In particular we have considered several resolution values: $N_{\rm side} = 4096, 2048, 1024, 709$. The results of this analysis are shown in Figure A.2.

From Fig. A.2 it is possible to infer two main things. First of all, the behaviour of the curves gets better as we increase the signal to noise ratio, this means that the $\nu > 3$ catalog shows a better behaviour than the $\nu > 1$ one for both the lensing maps; this can be caused by the fact that we are considering voids with larger radii obtained from catalogs with larger $\nu = \kappa/\sigma$. Besides, as the resolution of our flat square patches decreases, the concavity shows an improvement even if it still affects the profiles.

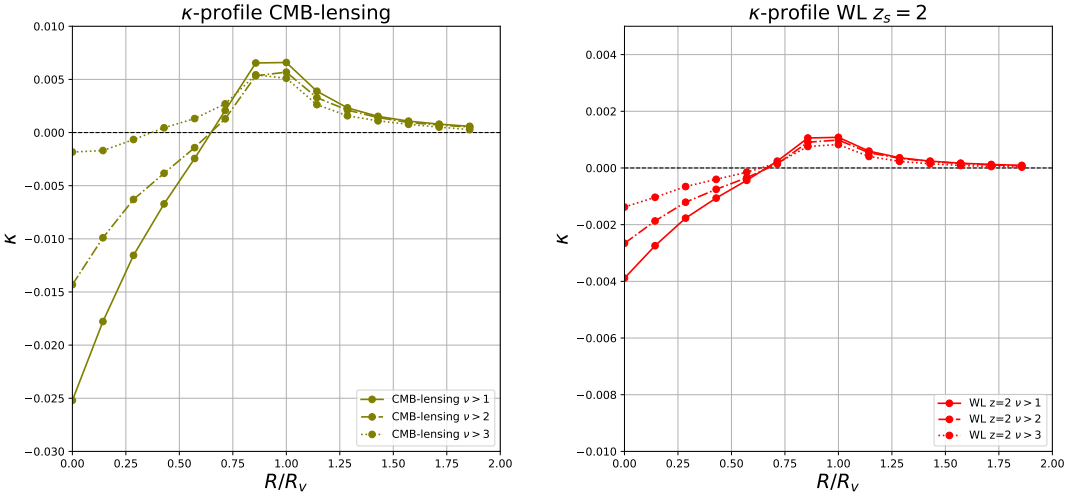

Figure A.1: Stacked convergence profiles of the CMB-lensing map (left) and the WL(z_s=2) map (right) in the case of the three void catalogs $\nu > 1$, $\nu > 2$ and $\nu > 3$ as a function of the stacked radial distance R/R_v.

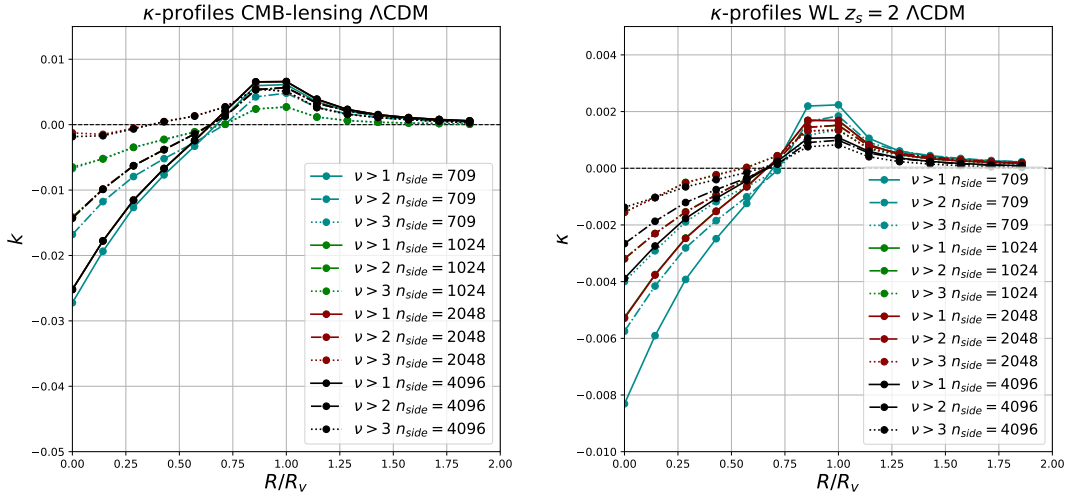

Figure A.2: Convergence profiles of CMB-lensing map (left) and lensing map with $z_s = 2$ (right) averaged over all the sections with different resolution values $N_{\rm side}$. Different linestyles (solid, dashed, and dotted) refer to different value for the SNR threshold ($\nu > 1$, 2, 3 respectively).

It is possible to compute what should be the right value of $N_{\rm side}$ for our flat sections that maintains unchanged the resolution of the original full-sky map, simply by taking the ratio of the surface (100 deg^2 for flat-patches, 40000 deg^2 for the full-sky) discretized and represented into pixel grid, this is:

$$\frac{100}{N^2_{\rm side,flat}} = \frac{40000}{12N^2_{\rm side,full-sky}} \tag{A.2}$$

Since $N_{\rm side,full-sky}$ is set by our full-sky maps, $N_{\rm side,full-sky} = 4096$, we can recover a value of $N_{\rm side,flat}$=709 for our projected sections. This is why we have decided to use in our analysis an $N_{\rm side,flat} = 709$ for our flat square patches: not to introduce changes in the resolution of the full-sky

maps and in order not to underestimate or overestimate the resolution of the convergence field.

A.2 κ-profile for different R_V values

A second check on our profiles is based on the selection of the radii of our lensing voids.

In Fig. A.3 we show the convergence profiles of the CMB-lensing map and the WL map with $z_s = 2$ averaged over all the projected sections in the ΛCDM scenario.

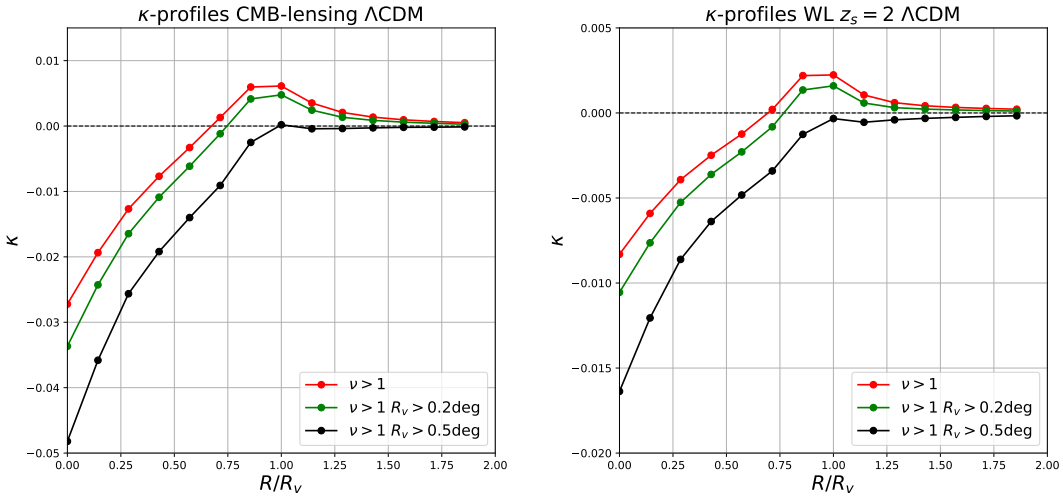

Figure A.3: Convergence profile of CMB-lensing map (left) and WL map with $z_S = 2$ (right), averaged over all the sections with a resolution of $N_{\rm side} = 709$ and different $R_{\rm V,min}$ selected.

In both cases we plot the κ-profiles obtained from void catalogs with $\nu > 1$, $\nu > 2$ and $\nu > 3$; in particular, we plot also the curves computed by choosing the catalog $\nu > 1$ and selecting from this catalog all lensing voids with radii $R_V > 0.2$ deg and $R_V > 0.5$ deg. It means that we are selecting voids with associated radius R_V larger than a certain value.

Imposing a certain cut on the radius R_V does not change the concavity of the void κ-profiles, as can be seen by Fig. A.3. This could be interpreted as the profile is fully due to the native resolution of the full-sky lensing maps we have analyzed in this work. Even if a full-sky resolution of $N_{\rm side} = 4096$ is extremely large, when projected to 10x10 deg^2 patches, it translates into a lower resolution when compared to the one usually adopted in flat-sky analyses. This means that we smooth out small scale structures with respect to the latter case, which is e.g. considered in Davies et al. (2018). In fact, works in preparation (Vielzeuf et al. 2021, in prep.), that cross-correlate our same set of simulated CMB-lensing maps with void catalogs obtained applying the 2D void finder from Sánchez et al. (2017); Vielzeuf et al. (2019) directly to the DM halo lightcones constructed from the DEMNUni simulations, show that CMB-lensing void profiles start to become convex as the smoothing scale in the void-finder is decreased.

Appendix B

Values of $\Delta(\%)$ between the $\nu\Lambda$CDM and the ΛCDM cosmologies

Here we show some of the percent residuals $\Delta_{\nu,R_V,R/R_V}(\%)$ obtained both from the three probes we have analyzed: the CMB-lensing map, the weak lensing $z_s = 2$ map and the Euclid-like redshift distribution map and for the six CMB-lensing summed maps: $19 < z_1 < 99$, $12 < z_2 < 15$, $5 < z_3 < 11$, $2.5 < z_4 < 4$, $1 < z_5 < 2$ and $0.5 < z_6 < 1$.

B.1 $\Delta(\%)$ of the cumulative projected density of lensing peaks

$\Delta(\%)_{\rm CMB}$	$\Delta(\%)_{z_s=2}$	$\Delta(\%)_{\rm Euclid}$
-1.6	-0.7	-0.9
-1.6	-1.1	-1.1
-1.6	-1.3	-0.7
-1.6	-0.6	0.1
-1.7	-0.1	0.1
-1.8	0.7	-0.3
-1.9	0.3	-1.0
-2.0	0.9	-3.1
-2.5	0.6	-5.2
-2.3	-3.2	-7.5
-2.1	-5.6	-11.7
-3.7	-10.2	-12.8
-6.1	-9.6	-12.8

Table B.1: Values of $\Delta_\nu(\%)$ for the cumulative projected density of κ-peaks as function of $\nu = \frac{\kappa}{\sigma}$ for the three probes: the CMB-lensing map, the WL($z_s = 2$) map and the Euclid-like redshift distribution map.

$\Delta(\%)_{z_1}$	$\Delta(\%)_{z_2}$	$\Delta(\%)_{z_3}$	$\Delta(\%)_{z_4}$	$\Delta(\%)_{z_5}$	$\Delta(\%)_{z_6}$
0.03	-0.3	-0.1	-0.4	-0.2	-0.3
-0.04	-0.3	-0.1	-0.4	-0.3	-0.7
-0.2	-0.4	-0.1	-0.5	-0.4	-0.6
-0.6	-0.4	0.1	-0.5	-0.3	-0.5
-0.8	-0.4	0.1	-0.4	-0.1	-0.4
-0.5	-0.3	0.1	-0.4	-0.05	-0.4
1.3	-0.5	0.04	-0.3	-0.4	-1.6
5.1	-1.0	0.2	0.4	-1.1	-2.5
1.2	-2.3	0.4	0.3	-3.0	-4.6
20.5	-3.3	1.5	0.4	-5.7	-7.7
32.9	-4.0	1.8	0.8	-7.3	-10.3
53.8	-4.9	4.9	2.1	-4.9	-13.8
78.7	-3.9	3.8	4.5	-7.8	-20.3

Table B.2: Values of $\Delta_\nu(\%)$ for the cumulative projected density of κ-peaks as function of $\nu = \frac{\kappa}{\sigma}$ for the six CMB-lensing summed maps at different redshift ranges.

B.2 $\Delta(\%)$ of the cumulative projected density of voids

$\Delta(\%)_{\rm CMB}$			$\Delta(\%)_{z_s=2}$			$\Delta(\%)_{\rm Euclid}$		
$\nu > 1$	$\nu > 2$	$\nu > 3$	$\nu > 1$	$\nu > 2$	$\nu > 3$	$\nu > 1$	$\nu > 2$	$\nu > 3$
-3.0	-2.9	-5.8	-2.5	-2.5	-3.1	-2.6	0.9	-6.0
-0.1	-2.3	-5.4	-0.8	-0.2	-4.4	-0.4	0.8	-5.5
3.7	-1.8	-5.6	0.9	1.4	-3.9	0.7	1.8	-5.5
6.6	0.1	-3.4	2.3	2.5	0.1	2.6	2.0	-4.1
9.7	1.3	-1.5	5.2	4.6	2.1	4.3	5.6	0.3
15.0	2.7	-2.3	7.0	8.6	3.3	5.9	7.7	7.5
18.5	5.9	3.9	9.3	13.2	10.7	8.4	11.4	16.5
27.3	5.3	7.5	13.9	14.9	16.9	10.3	10.8	33.7
34.0	5.5	-1.7	9.8	9.9	27.5	17.4	8.8	66.9
44.6	12.5	4.7	10.77	14.2	25.8	34.1	2.9	75.7
39.0	12.9	12.2	17.9	13.9	2.1	75.6	15.1	-33.3
32.5	42.1	20.2	81.5	18.4	38.7	41.1	43.9	-
20.8	49.9	-	274.5	25.9	8.6	-26.0	36.9	-

Table B.3: Values of $\Delta_{R_V}(\%)$ for the cumulative projected density of lensing voids as function of their radius R_V for the CMB-lensing map, the WL($z_s = 2$) map and the Euclid-like map for the three catalogs identified in this thesis $\nu > 1$, $\nu > 2$ and $\nu > 3$.

$\Delta(\%)_{z_1}$			$\Delta(\%)_{z_2}$			$\Delta(\%)_{z_3}$		
$\nu > 1$	$\nu > 2$	$\nu > 3$	$\nu > 1$	$\nu > 2$	$\nu > 3$	$\nu > 1$	$\nu > 2$	$\nu > 3$
0.2	-1.4	8.6	-1.3	-3.9	-1.0	-2.1	-0.2	-0.4
0.3	-2.4	4.2	0.8	-3.8	-1.7	-1.7	4.2	-1.0
1.1	-3.2	1.0	4.6	-3.3	-2.1	-0.8	6.4	-0.3
1.4	-4.5	-0.3	9.9	-2.3	-1.4	-0.6	6.1	1.9
1.6	-4.1	-1.5	16.0	-3.6	-0.6	0.1	9.6	4.5
0.8	-4.1	-2.3	22.3	0.6	-4.1	0.1	17.6	2.0
3.4	-1.7	-8.0	25.8	1.7	-0.3	-2.7	20.3	1.0
6.9	11.7	-17.1	17.2	7.2	0.3	-3.3	15.8	2.7
9.4	14.0	-14.1	19.7	9.5	0.7	-0.1	24.2	8.1
4.8	38.1	-10.3	-4.9	-1.5	-17.6	2.7	27.8	7.6
-2.6	-15.8	1.6	-46.4	-4.6	-36.6	-8.9	26.7	5.7
0.7	-	-26.8	-27.2	-	-11.7	0.6	10.1	11.2
-2.8	-	-18.4	-0.9	-	221.8	-	-30.9	197.9

Table B.4: Values of $\Delta_{R_V}(\%)$ for the cumulative projected density of lensing voids for partial CMB-lensing maps at redshift ranges $19 < z_1 < 99$, $12 < z_2 < 15$, $5 < z_3 < 11$.

$\Delta(\%)_{z_4}$			$\Delta(\%)_{z_5}$			$\Delta(\%)_{z_6}$		
$\nu > 1$	$\nu > 2$	$\nu > 3$	$\nu > 1$	$\nu > 2$	$\nu > 3$	$\nu > 1$	$\nu > 2$	$\nu > 3$
-0.9	-7.2	-4.5	-0.3	-2.1	-5.0	0.3	-1.5	-3.4
-1.3	-9.6	-6.0	-1.2	-0.8	-4.8	0.6	-1.5	-3.2
-0.9	-9.4	-5.2	-1.3	0.1	-3.5	1.8	-0.6	-1.1
-0.1	-14.0	-4.3	-0.8	0.7	-2.6	3.3	0.7	-1.4
0.0001	-10.1	-1.0	1.1	3.6	0.8	6.4	3.5	1.1
2.9	-8.6	1.9	2.7	4.5	2.0	8.8	6.0	4.8
5.8	4.7	13.9	4.0	10.6	-3.2	14.2	9.9	11.4
3.6	-35.9	23.3	8.9	18.4	3.6	16.8	20.7	19.4
4.4	-63.4	22.1	14.6	20.6	-9.9	18.9	27.5	24.9
-7.5	-	30.0	14.6	18.3	22.0	34.1	34.1	30.1
-1.2	-	11.2	23.4	14.4	32.1	25.8	63.9	6.4
-11.9	-	99.4	25.9	-3.4	17.0	110.3	46.7	-4.3
-24.6	-	-5.5	-15.7	65.3	2.4	310.1	33.1	-5.2

Table B.5: Values of $\Delta_{R_V}(\%)$ for the cumulative projected density of lensing voids for the CMB-lensing maps at $2.5 < z_4 < 4$, $1 < z_5 < 2$, $0.5 < z_6 < 1$.

B.3 $\Delta(\%)$ of the stacked convergence profile

$\Delta(\%)_{\rm CMB}$			$\Delta(\%)_{z_s=2}$			$\Delta(\%)_{\rm Euclid}$		
$\nu > 1$	$\nu > 2$	$\nu > 3$	$\nu > 1$	$\nu > 2$	$\nu > 3$	$\nu > 1$	$\nu > 2$	$\nu > 3$
-4.1	-4.3	6.9	-30.6	-31.2	-32.9	-28.7	-30.2	-25.2
-4.7	-3.4	-6.4	-30.0	-30.0	-33.6	-29.0	-28.3	-26.3
-4.5	-4.81	-6.1	-29.8	-29.0	-30.3	-28.8	-30.4	-29.1
-4.5	-5.6	-8.9	-29.3	-29.9	-28.9	-29.2	-29.1	-27.8
-4.3	-6.9	-13.1	-29.8	-31.4	-28.0	-29.5	-29.3	-27.9
-3.6	31.8	39.7	-33.	-42.4	-30.3	-27.2	-27.3	-30.0
-4.7	-5.0	-4.6	-31.0	-30.7	-32.4	-30.3	-29.9	-32.2
-4.8	-4.5	-4.9	-31.0	-30.8	-31.6	-29.8	-30.0	-31.8
-3.5	-3.5	-2.0	-30.9	-30.6	-31.8	-29.4	-30.6	-31.0
-3.0	-3.8	-4.3	-31.0	-30.0	-30.4	-29.3	-30.6	-31.2
-2.8	-2.3	-0.9	-30.7	-30.1	-30.1	-29.5	-30.1	-31.2
-1.9	-1.	-8.5	-30.3	-30.	-31.3	-29.5	-29.5	-31.6
-1.8	-3.1	-18.1	-30.3	-30.4	-34.9	-28.	-30.4	-29.2
-1.5	-2.3	-14.	-30.5	-31.8	-35.4	-29.4	-32.1	-33.7

Table B.6: Values of $\Delta_{\rm R/R_v}(\%)$ for the convergence profiles of the CMB-lensing map, the WL($z_{\rm s} = 2$) map and the Euclid-like lensing map for the three different catalogs $\nu > 1$, $\nu > 2$ and $\nu > 3$.

$\Delta(\%)_{z_1}$			$\Delta(\%)_{z_2}$			$\Delta(\%)_{z_3}$		
$\nu > 1$	$\nu > 2$	$\nu > 3$	$\nu > 1$	$\nu > 2$	$\nu > 3$	$\nu > 1$	$\nu > 2$	$\nu > 3$
-0.05	-4.1	15.0	-2.9	-2.8	69.9	-2.8	-11.5	-46.3
-1.3	0.03	-14.8	-2.8	-4.3	23.0	-3.2	-4.2	-21.9
-1.3	-3.9	-14.7	-1.8	-2.8	3.9	-3.6	-4.7	-7.3
-2.0	-3.7	-13.9	-2.9	-4.0	-26.0	-5.0	-5.3	-19.8
-1.2	-1.7	-9.3	-3.3	-2.1	8.5	-5.9	-7.1	-18.1
1.9	-4.1	-6.5	-7.5	3.8	-33.3	13.3	-13.7	-21.1
-0.6	0.4	3.9	-2.9	-3.2	5.0	-2.4	-1.9	-1.8
-1.02	-1.3	3.7	-3.2	-1.9	6.4	-2.4	-2.4	3.2
-1.9	-2.4	-1.8	-2.8	-1.8	18.6	-0.4	-0.9	19.8
-4.1	-4.8	-4.4	-0.3	-2.0	-6.4	-0.3	1.3	31.8
-5.6	-1.4	22.4	-2.5	1.7	-14.9	5.5	3.9	45.5
-7.6	-4.6	29.5	-7.4	-3.0	6.4	8.5	16.1	187.3
-7.5	0.5	243.4	-7.0	-14.3	-10.5	17.7	24.4	117.9
-8.4	21.0	-41.9	3.5	1.5	20.7	48.5	17.2	179.6

Table B.7: Values of $\Delta_{\rm R/R_v}(\%)$ of the convergence profiles associated to the lensing maps z_1, z_2 and z_3 for the usual void catalogs $\nu > 1$, $\nu > 2$ and $\nu > 3$.

$\Delta(\%)_{z_4}$			$\Delta(\%)_{z_5}$			$\Delta(\%)_{z_6}$		
$\nu > 1$	$\nu > 2$	$\nu > 3$	$\nu > 1$	$\nu > 2$	$\nu > 3$	$\nu > 1$	$\nu > 2$	$\nu > 3$
-6.0	-10.1	-4.8	-5.2	-3.8	-12.0	-3.9	-7.4	14.5
-3.7	-4.6	7.5	-4.3	-5.9	-2.5	-4.8	-7.4	-5.8
-4.4	-3.6	-5.1	-6.1	-4.0	-3.9	-4.5	-4.6	-6.0
-4.0	-4.1	-13.8	-5.8	-6.3	-9.2	-5.0	-5.8	-5.2
-3.2	-3.9	-11.9	-7.1	-6.0	-10.3	-5.1	-5.0	-5.8
2.7	-4.2	17.7	13.8	-11.4	-28.1	-70.3	-4.4	9.4
-4.7	-4.6	-6.3	-5.4	-3.4	2.2	-6.1	-8.0	-10.7
-4.0	-5.4	-8.2	-4.6	-3.1	-1.0	-6.6	-7.4	-7.9
-4.7	-6.0	2.9	-2.0	2.8	15.3	-7.1	-7.7	-12.9
-4.5	-5.4	-3.1	4.3	6.3	17.0	-8.8	-12.7	-4.0
-3.9	-4.8	10.1	16.9	6.4	20.0	-12.7	-9.1	-15.2
-6.7	2.4	58.4	31.1	11.4	23.6	-28.9	-18.6	-12.6
4.0	10.1	54.0	37.1	15.2	16.7	-42.7	-21.9	-31.6
5.8	9.5	21.4	91.1	67.1	63.1	-40.1	-17.9	-53.8

Table B.8: Values of $\Delta_{R/R_V}(\%)$ of the convergence profiles associated to the lensing maps z_4, z_5 and z_6 and the usual void catalogs $\nu > 1$, $\nu > 2$ and $\nu > 3$.

B.4 $\Delta(\%)$ of the stacked tangential shear profile

$\Delta(\%)_{\rm CMB}$			$\Delta(\%)_{z_s=2}$			$\Delta(\%)_{\rm Euclid}$		
$\nu > 1$	$\nu > 2$	$\nu > 3$	$\nu > 1$	$\nu > 2$	$\nu > 3$	$\nu > 1$	$\nu > 2$	$\nu > 3$
-2.6	-6.3	52.1	-32.2	-34.5	-31.2	-28.1	-35.2	-22.0
-4.2	-2.9	11.0	-31.0	-32.9	-36.7	-28.9	-28.1	-21.1
-4.3	-3.0	6.3	-30.8	-30.7	-35.1	-28.6	-30.1	-25.4
-4.4	-3.4	2.5	-30.2	-29.8	-33.6	-28.7	-29.7	-26.1
-4.3	-4.2	-1.6	-30.3	-30.1	-32.0	-28.9	-29.7	-26.5
-4.5	-4.7	-3.4	-30.4	-30.5	-32.1	-29.5	-29.7	-29.0
-4.5	-4.5	-3.6	-30.4	-30.6	-31.7	-29.2	-29.7	-29.0
-4.0	-4.1	-1.7	-30.2	-30.4	-31.9	-28.9	-29.9	-27.6
-4.0	-4.3	-2.4	-30.1	-30.2	-31.4	-28.8	-29.7	-26.8
-4.1	-4.0	-1.3	-29.9	-30.2	-31.4	-28.8	-29.5	-26.2
-4.0	-3.9	-2.8	-29.8	-30.4	-31.8	-28.7	-29.3	-25.9
-4.1	-4.4	-3.8	-29.8	-30.3	-32.8	-28.6	-29.5	-24.8
-4.2	-4.4	-2.0	-29.8	-30.6	-32.8	-28.7	-29.8	-25.6

Table B.9: Values of $\Delta_{R/R_V}(\%)$ of the tangential shear profiles of the CMB-lensing map, the WL($z_s = 2$) map and the Euclid-like map for the three different catalogs $\nu > 1$, $\nu > 2$ and $\nu > 3$.

$\Delta(\%)_{z_1}$			$\Delta(\%)_{z_2}$			$\Delta(\%)_{z_3}$		
$\nu > 1$	$\nu > 2$	$\nu > 3$	$\nu > 1$	$\nu > 2$	$\nu > 3$	$\nu > 1$	$\nu > 2$	$\nu > 3$
3.3	-14.4	364.9	-3.2	0.9	482.5	-1.8	-29.2	-97.4
0.4	-0.1	44.8	-4.3	-4.4	184.9	-2.1	-13.8	-62.1
0.3	-1.8	7.9	-2.3	-2.6	117.1	-1.6	-9.7	-39.7
-0.8	-3.5	-2.2	-2.5	-4.1	34.7	-2.4	-7.4	-34.7
-0.7	-2.6	-5.2	-3.0	-4.1	34.7	-2.4	-6.5	-29.9
-0.8	-1.5	-1.4	-2.7	-3.2	15.2	-3.2	-5.3	-18.4
-1.0	-2.3	-1.1	-2.8	-2.5	15.1	-3.2	-5.3	-14.9
-1.3	-3.2	-6.6	-2.6	-2.8	25.9	-2.9	-6.4	-22.3
-1.4	-3.9	-8.2	-2.2	-3.1	20.7	-3.6	-6.9	-27.1
-1.2	-3.2	-3.9	-2.6	-2.6	22.9	-3.4	-7.5	-29.1
-1.2	-3.7	-5.2	-2.9	-3.5	29.9	-3.6	-6.8	-27.1
-1.0	-3.2	-2.5	-2.7	-4.7	29.8	-3.6	-7.3	-35.3
-0.9	-1.9	-13.9	-2.3	-3.1	32.6	-3.2	-8.7	-38.9

Table B.10: Values of $\Delta_{R/Rv}(\%)$ of the tangential shear profiles of lensing maps z_1, z_2 and z_3 for the usual catalogs $\nu > 1$, $\nu > 2$ and $\nu > 3$.

$\Delta(\%)_{z_4}$			$\Delta(\%)_{z_5}$			$\Delta(\%)_{z_6}$		
$\nu > 1$	$\nu > 2$	$\nu > 3$	$\nu > 1$	$\nu > 2$	$\nu > 3$	$\nu > 1$	$\nu > 2$	$\nu > 3$
-11.8	-23.8	-37.6	-7.5	1.6	-33.2	-1.0	-7.5	92.5
-6.0	-13.5	9.5	-3.0	-5.9	-13.0	-3.9	-11.3	24.7
-5.6	-9.3	14.5	-4.5	-2.9	-5.2	-3.8	-7.8	10.7
-5.3	-7.8	2.4	-4.5	-4.2	-5.8	-4.1	-7.6	6.1
-4.3	-6.0	-7.3	-4.7	-3.9	-2.7	-4.76	-6.8	-0.8
-4.8	-5.6	-4.5	-5.0	-4.4	-4.4	-5.1	-7.2	-4.0
-4.4	-5.9	-5.7	-5.	-4.2	-5.4	-5.3	-6.8	-2.9
-4.9	-6.4	1	-4.6	-3.2	-4.2	-4.7	-6.6	-0.3
-4.9	-6.4	-2.2	-4.5	-3.8	-6.8	-4.3	-7.3	4.2
-4.8	-6.0	0.7	-4.5	-4.7	-9.0	-4.1	-6.2	2.9
-5.1	-5.5	5.0	-4.8	-4.9	-10.7	-4.5	-7.1	4.7
-4.5	-5.1	1.8	-5.0	-5.2	-12.4	-4.0	-6.9	3.4
-4.6	-5.	-1.5	-5.0	-3.8	-11.2	-4.1	-6.2	1.9

Table B.11: Values of $\Delta_{R/Rv}(\%)$ of the tangential shear profiles of lensing maps z_4, z_5 and z_6 for the usual catalogs $\nu > 1$, $\nu > 2$ and $\nu > 3$.

Bibliography

B. Abolfathi, D. S. Aguado, G. Aguilar, C. Allende Prieto, A. Almeida, T. T. Ananna, F. Anders, S. F. Anderson, B. H. Andrews, B. Anguiano, and et al. The Fourteenth Data Release of the Sloan Digital Sky Survey: First Spectroscopic Data from the Extended Baryon Oscillation Spectroscopic Survey and from the Second Phase of the Apache Point Observatory Galactic Evolution Experiment. ApJS, 235:42, Apr. 2018. doi: 10.3847/1538-4365/aa9e8a. URL http://adsabs.harvard.edu/abs/2018ApJS..235...42A.

Q. R. Ahmad, R. C. Allen, T. C. Andersen, J. D. Anglin, J. C. Barton, E. W. Beier, M. Bercovitch, J. Bigu, S. D. Biller, R. A. Black, I. Blevis, R. J. Boardman, J. Boger, E. Bonvin, M. G. Boulay, M. G. Bowler, T. J. Bowles, S. J. Brice, M. C. Browne, T. V. Bullard, G. Bühler, J. Cameron, Y. D. Chan, H. H. Chen, M. Chen, X. Chen, B. T. Cleveland, E. T. Clifford, J. H. Cowan, D. F. Cowen, G. A. Cox, X. Dai, F. Dalnoki-Veress, W. F. Davidson, P. J. Doe, G. Doucas, M. R. Dragowsky, C. A. Duba, F. A. Duncan, M. Dunford, J. A. Dunmore, E. D. Earle, S. R. Elliott, H. C. Evans, G. T. Ewan, J. Farine, H. Fergani, A. P. Ferraris, R. J. Ford, J. A. Formaggio, M. M. Fowler, K. Frame, E. D. Frank, W. Frati, N. Gagnon, J. V. Germani, S. Gil, K. Graham, D. R. Grant, R. L. Hahn, A. L. Hallin, E. D. Hallman, A. S. Hamer, A. A. Hamian, W. B. Handler, R. U. Haq, C. K. Hargrove, P. J. Harvey, R. Hazama, K. M. Heeger, W. J. Heintzelman, J. Heise, R. L. Helmer, J. D. Hepburn, H. Heron, J. Hewett, A. Hime, M. Howe, J. G. Hykawy, M. C. Isaac, P. Jagam, N. A. Jelley, C. Jillings, G. Jonkmans, K. Kazkaz, P. T. Keener, J. R. Klein, A. B. Knox, R. J. Komar, R. Kouzes, T. Kutter, C. C. Kyba, J. Law, I. T. Lawson, M. Lay, H. W. Lee, K. T. Lesko, J. R. Leslie, I. Levine, W. Locke, S. Luoma, J. Lyon, S. Majerus, H. B. Mak, J. Maneira, J. Manor, A. D. Marino, N. McCauley, A. B. McDonald, D. S. McDonald, K. McFarlane, G. McGregor, R. Meijer Drees, C. Mifflin, G. G. Miller, G. Milton, B. A. Moffat, M. Moorhead, C. W. Nally, M. S. Neubauer, F. M. Newcomer, H. S. Ng, A. J. Noble, E. B. Norman, V. M. Novikov, M. O'Neill, C. E. Okada, R. W. Ollerhead, M. Omori, J. L. Orrell, S. M. Oser, A. W. Poon, T. J. Radcliffe, A. Roberge, B. C. Robertson, R. G. Robertson, S. S. Rosendahl, J. K. Rowley, V. L. Rusu, E. Saettler, K. K. Schaffer, M. H. Schwendener, A. Schülke, H. Seifert, M. Shatkay, J. J. Simpson, C. J. Sims, D. Sinclair, P. Skensved, A. R. Smith, M. W. Smith, T. Spreitzer, N. Starinsky, T. D. Steiger, R. G. Stokstad, L. C. Stonehill, R. S. Storey, B. Sur, R. Tafirout, N. Tagg, N. W. Tanner, R. K. Taplin, M. Thorman, P. M. Thornewell, P. T. Trent, Y. I. Tserkovnyak, R. van Berg, R. G. van de Water, C. J. Virtue, C. E. Waltham, J. X. Wang, D. L. Wark, N. West, J. B. Wilhelmy, J. F. Wilkerson, J. R. Wilson, P. Wittich, J. M. Wouters, and M. Yeh. Direct Evidence for Neutrino Flavor Transformation from Neutral-Current Interactions in the Sudbury Neutrino Observatory. Phys. Rev. Lett., 89 (1):011301, July 2002. doi: 10.1103/PhysRevLett.89.011301. URL https://ui.adsabs.harvard.edu/abs/2002PhRvL..89a1301A.

S. N. Ahmed, A. E. Anthony, E. W. Beier, A. Bellerive, S. D. Biller, J. Boger, M. G. Boulay, M. G. Bowler, T. J. Bowles, S. J. Brice, T. V. Bullard, Y. D. Chan, M. Chen, X. Chen, B. T. Cleveland, G. A. Cox, X. Dai, F. Dalnoki-Veress, P. J. Doe, R. S. Dosanjh, G. Doucas, M. R. Dragowsky, C. A. Duba, F. A. Duncan, M. Dunford, J. A. Dunmore, E. D. Earle, S. R. Elliott, H. C. Evans, G. T. Ewan, J. Farine, H. Fergani, F. Fleurot, J. A. Formaggio, M. M. Fowler, K. Frame, B. G. Fulsom, N. Gagnon, K. Graham, D. R. Grant, R. L. Hahn, J. C. Hall, A. L. Hallin, E. D. Hall-

man, A. S. Hamer, W. B. Handler, C. K. Hargrove, P. J. Harvey, R. Hazama, K. M. Heeger, W. J. Heintzelman, J. Heise, R. L. Helmer, R. J. Hemingway, A. Hime, M. A. Howe, P. Jagam, N. A. Jelley, J. R. Klein, M. S. Kos, A. V. Krumins, T. Kutter, C. C. Kyba, H. Labranche, R. Lange, J. Law, I. T. Lawson, K. T. Lesko, J. R. Leslie, I. Levine, S. Luoma, R. MacLellan, S. Majerus, H. B. Mak, J. Maneira, A. D. Marino, N. McCauley, A. B. McDonald, S. McGee, G. McGregor, C. Mifflin, K. K. Miknaitis, G. G. Miller, B. A. Moffat, C. W. Nally, B. G. Nickel, A. J. Noble, E. B. Norman, N. S. Oblath, C. E. Okada, R. W. Ollerhead, J. L. Orrell, S. M. Oser, C. Ouellet, S. J. Peeters, A. W. Poon, B. C. Robertson, R. G. Robertson, E. Rollin, S. S. Rosendahl, V. L. Rusu, M. H. Schwendener, O. Simard, J. J. Simpson, C. J. Sims, D. Sinclair, P. Skensved, M. W. Smith, N. Starinsky, R. G. Stokstad, L. C. Stonehill, R. Tafirout, Y. Takeuchi, G. Tešić, M. Thomson, M. Thorman, R. van Berg, R. G. van de Water, C. J. Virtue, B. L. Wall, D. Waller, C. E. Waltham, H. W. Tseung, D. L. Wark, N. West, J. B. Wilhelmy, J. F. Wilkerson, J. R. Wilson, J. M. Wouters, M. Yeh, and K. Zuber. Measurement of the Total Active ^{8}B Solar Neutrino Flux at the Sudbury Neutrino Observatory with Enhanced Neutral Current Sensitivity. Phys. Rev. Lett., 92(18):181301, May 2004. doi: 10.1103/PhysRevLett.92.181301. URL https://ui.adsabs.harvard.edu/abs/2004PhRvL..92r1301A.

S. Alam, M. Ata, S. Bailey, F. Beutler, D. Bizyaev, J. A. Blazek, A. S. Bolton, J. R. Brownstein, A. Burden, C.-H. Chuang, J. Comparat, A. J. Cuesta, K. S. Dawson, D. J. Eisenstein, S. Escoffier, H. Gil-Marín, J. N. Grieb, N. Hand, S. Ho, K. Kinemuchi, D. Kirkby, F. Kitaura, E. Malanushenko, V. Malanushenko, C. Maraston, C. K. McBride, R. C. Nichol, M. D. Olmstead, D. Oravetz, N. Padmanabhan, N. Palanque-Delabrouille, K. Pan, M. Pellejero-Ibanez, W. J. Percival, P. Petitjean, F. Prada, A. M. Price-Whelan, B. A. Reid, S. A. Rodríguez-Torres, N. A. Roe, A. J. Ross, N. P. Ross, G. Rossi, J. A. Rubiño-Martín, S. Saito, S. Salazar-Albornoz, L. Samushia, A. G. Sánchez, S. Satpathy, D. J. Schlegel, D. P. Schneider, C. G. Scóccola, H.-J. Seo, E. S. Sheldon, A. Simmons, A. Slosar, M. A. Strauss, M. E. C. Swanson, D. Thomas, J. L. Tinker, R. Tojeiro, M. V. Magaña, J. A. Vazquez, L. Verde, D. A. Wake, Y. Wang, D. H. Weinberg, M. White, W. M. Wood-Vasey, C. Yèche, I. Zehavi, Z. Zhai, and G.-B. Zhao. The clustering of galaxies in the completed SDSS-III Baryon Oscillation Spectroscopic Survey: cosmological analysis of the DR12 galaxy sample. MNRAS, 470:2617–2652, Sept. 2017. doi: 10.1093/mnras/stx721. URL http://adsabs.harvard.edu/abs/2017MNRAS.470.2617A.

A. Balbi, P. Ade, J. Bock, J. Borrill, A. Boscaleri, P. De Bernardis, P. G. Ferreira, S. Hanany, V. Hristov, A. H. Jaffe, A. T. Lee, S. Oh, E. Pascale, B. Rabii, P. L. Richards, G. F. Smoot, R. Stompor, C. D. Winant, and J. H. P. Wu. Erratum: Constraints on Cosmological Parameters from MAXIMA-1. ApJ, 558(2):L145–L145, Sept. 2001. doi: 10.1086/323608. URL https://ui.adsabs.harvard.edu/abs/2001ApJ...558L.145B.

M. Bartelmann. TOPICAL REVIEW Gravitational lensing. Classical and Quantum Gravity, 27 (23):233001, Dec. 2010. doi: 10.1088/0264-9381/27/23/233001. URL https://ui.adsabs.harvard.edu/abs/2010CQGra..27w3001B.

M. Bartelmann and P. Schneider. Weak gravitational lensing. Phys. Rep., 340(4-5):291–472, Jan. 2001. doi: 10.1016/S0370-1573(00)00082-X. URL https://ui.adsabs.harvard.edu/abs/2001PhR...340..291B.

R. Becker-Szendy, C. B. Bratton, D. Casper, S. T. Dye, W. Gajewski, M. Goldhaber, T. J. Haines, P. G. Halverson, D. Kielczewska, W. R. Kropp, J. G. Learned, J. M. Losecco, S. Matsuno, G. McGrath, C. McGrew, R. Miller, L. R. Price, F. Reines, J. Schultz, H. W. Sobel, J. L. Stone, L. R. Sulak, and R. Svoboda. Electron- and muon-neutrino content of the atmospheric flux. Phys. Rev. D, 46(9):3720–3724, Nov. 1992. doi: 10.1103/PhysRevD.46.3720. URL https://ui.adsabs.harvard.edu/abs/1992PhRvD..46.3720B.

C. L. Bennett, D. Larson, J. L. Weiland, N. Jarosik, G. Hinshaw, N. Odegard, K. M. Smith, R. S. Hill, B. Gold, M. Halpern, E. Komatsu, M. R. Nolta, L. Page, D. N. Spergel, E. Wollack, J. Dunkley, A. Kogut, M. Limon, S. S. Meyer, G. S. Tucker, and E. L. Wright. Nine-year Wilkinson Microwave Anisotropy Probe (WMAP) Observations: Final Maps and Results. ApJS, 208(2):20, Oct. 2013. doi: 10.1088/0067-0049/208/2/20. URL https://ui.adsabs.harvard.edu/abs/2013ApJS..208...20B.

S. M. Bilenky. Neutrino. History of a unique particle. European Physical Journal H, 38(3):345–404, May 2013. doi: 10.1140/epjh/e2012-20068-9. URL https://ui.adsabs.harvard.edu/abs/2013EPJH...38..345B.

D. Blas, M. Garny, T. Konstandin, and J. Lesgourgues. Structure formation with massive neutrinos: going beyond linear theory. JCAP, 2014(11):039, Nov. 2014. doi: 10.1088/1475-7516/2014/11/039. URL https://ui.adsabs.harvard.edu/abs/2014JCAP...11..039B.

M. M. Brouwer, V. Demchenko, J. Harnois-Déraps, M. Bilicki, C. Heymans, H. Hoekstra, K. Kuijken, M. Alpaslan, S. Brough, Y.-C. Cai, M. V. Costa-Duarte, A. Dvornik, T. Erben, H. Hildebrandt, B. W. Holwerda, P. Schneider, C. Sifón, and E. van Uitert. Studying galaxy troughs and ridges using weak gravitational lensing with the Kilo-Degree Survey. MNRAS, 481(4):5189–5209, Dec 2018. doi: 10.1093/mnras/sty2589. URL https://ui.adsabs.harvard.edu/abs/2018MNRAS.481.5189B.

M. Calabrese, C. Carbone, G. Fabbian, M. Baldi, and C. Baccigalupi. Multiple lensing of the cosmic microwave background anisotropies. JCAP, 2015(3):049, Mar. 2015. doi: 10.1088/1475-7516/2015/03/049. URL https://ui.adsabs.harvard.edu/abs/2015JCAP...03..049C.

C. Carbone, V. Springel, C. Baccigalupi, M. Bartelmann, and S. Matarrese. Full-sky maps for gravitational lensing of the cosmic microwave background. MNRAS, 388(4):1618–1626, Aug. 2008. doi: 10.1111/j.1365-2966.2008.13544.x. URL https://ui.adsabs.harvard.edu/abs/2008MNRAS.388.1618C.

C. Carbone, C. Baccigalupi, M. Bartelmann, S. Matarrese, and V. Springel. Lensed CMB temperature and polarization maps from the Millennium Simulation. MNRAS, 396(2):668–679, June 2009. doi: 10.1111/j.1365-2966.2009.14746.x. URL https://ui.adsabs.harvard.edu/abs/2009MNRAS.396..668C.

C. Carbone, M. Petkova, and K. Dolag. DEMNUni: ISW, Rees-Sciama, and weak-lensing in the presence of massive neutrinos. JCAP, 2016(7):034, July 2016. doi: 10.1088/1475-7516/2016/07/034. URL https://ui.adsabs.harvard.edu/abs/2016JCAP...07..034C.

M. Cautun, E. Paillas, Y.-C. Cai, S. Bose, J. Armijo, B. Li, and N. Padilla. The Santiago-Harvard-Edinburgh-Durham void comparison - I. SHEDding light on chameleon gravity tests. MNRAS, 476(3):3195–3217, May 2018. doi: 10.1093/mnras/sty463. URL https://ui.adsabs.harvard.edu/abs/2018MNRAS.476.3195C.

S. R. Choudhury and S. Hannestad. Updated results on neutrino mass and mass hierarchy from cosmology with Planck 2018 likelihoods. JCAP, 2020(7):037, July 2020. doi: 10.1088/1475-7516/2020/07/037. URL https://ui.adsabs.harvard.edu/abs/2020JCAP...07..037C.

C. T. Davies, M. Cautun, and B. Li. Weak lensing by voids in weak lensing maps. MNRAS, 480(1):L101–L105, Oct. 2018. doi: 10.1093/mnrasl/sly135. URL https://ui.adsabs.harvard.edu/abs/2018MNRAS.480L.101D.

C. T. Davies, M. Cautun, and B. Li. The self-similarity of weak lensing peaks. MNRAS, 488(4): 5833–5851, Oct. 2019. doi: 10.1093/mnras/stz2157. URL https://ui.adsabs.harvard.edu/abs/2019MNRAS.488.5833D.

A. D. Dolgov. Neutrinos in cosmology. Phys. Rep., 370(4-5):333–535, Nov. 2002. doi: 10.1016/S0370-1573(02)00139-4. URL https://ui.adsabs.harvard.edu/abs/2002PhR...370..333D.

T. Eifler, H. Miyatake, E. Krause, C. Heinrich, V. Miranda, C. Hirata, J. Xu, S. Hemmati, M. Simet, P. Capak, A. Choi, O. Dore, C. Doux, X. Fang, R. Hounsell, E. Huff, H.-J. Huang, M. Jarvis, D. Masters, E. Rozo, D. Scolnic, D. N. Spergel, M. Troxel, A. von der Linden, Y. Wang, D. H. Weinberg, L. Wenzl, and H.-Y. Wu. Cosmology with the Wide-Field Infrared Survey Telescope – Multi-Probe Strategies. arXiv e-prints, art. arXiv:2004.05271, Apr. 2020. URL https://ui.adsabs.harvard.edu/abs/2020arXiv200405271E.

I. Esteban, M. C. Gonzalez-Garcia, M. Maltoni, I. Martinez-Soler, and T. Schwetz. Updated fit to three neutrino mixing: exploring the accelerator-reactor complementarity. Journal of High Energy Physics, 2017(1):87, Jan. 2017. doi: 10.1007/JHEP01(2017)087. URL https://ui.adsabs.harvard.edu/abs/2017JHEP...01..087E.

G. Fabbian, M. Calabrese, and C. Carbone. CMB weak-lensing beyond the Born approximation: a numerical approach. JCAP, 2018(2):050, Feb. 2018. doi: 10.1088/1475-7516/2018/02/050. URL https://ui.adsabs.harvard.edu/abs/2018JCAP...02..050F.

Y. Fukuda, T. Hayakawa, E. Ichihara, K. Inoue, K. Ishihara, H. Ishino, Y. Itow, T. Kajita, J. Kameda, S. Kasuga, K. Kobayashi, Y. Kobayashi, Y. Koshio, M. Miura, M. Nakahata, S. Nakayama, A. Okada, K. Okumura, N. Sakurai, M. Shiozawa, Y. Suzuki, Y. Takeuchi, Y. Totsuka, S. Yamada, M. Earl, A. Habig, E. Kearns, M. D. Messier, K. Scholberg, J. L. Stone, L. R. Sulak, C. W. Walter, M. Goldhaber, T. Barszczxak, D. Casper, W. Gajewski, P. G. Halverson, J. Hsu, W. R. Kropp, L. R. Price, F. Reines, M. Smy, H. W. Sobel, M. R. Vagins, K. S. Ganezer, W. E. Keig, R. W. Ellsworth, S. Tasaka, J. W. Flanagan, A. Kibayashi, J. G. Learned, S. Matsuno, V. J. Stenger, D. Takemori, T. Ishii, J. Kanzaki, T. Kobayashi, S. Mine, K. Nakamura, K. Nishikawa, Y. Oyama, A. Sakai, M. Sakuda, O. Sasaki, S. Echigo, M. Kohama, A. T. Suzuki, T. J. Haines, E. Blaufuss, B. K. Kim, R. Sanford, R. Svoboda, M. L. Chen, Z. Conner, J. A. Goodman, G. W. Sullivan, J. Hill, C. K. Jung, K. Martens, C. Mauger, C. McGrew, E. Sharkey, B. Viren, C. Yanagisawa, W. Doki, K. Miyano, H. Okazawa, C. Saji, M. Takahata, Y. Nagashima, M. Takita, T. Yamaguchi, M. Yoshida, S. B. Kim, M. Etoh, K. Fujita, A. Hasegawa, T. Hasegawa, S. Hatakeyama, T. Iwamoto, M. Koga, T. Maruyama, H. Ogawa, J. Shirai, A. Suzuki, F. Tsushima, M. Koshiba, M. Nemoto, K. Nishijima, T. Futagami, Y. Hayato, Y. Kanaya, K. Kaneyuki, Y. Watanabe, D. Kielczewska, R. A. Doyle, J. S. George, A. L. Stachyra, L. L. Wai, R. J. Wilkes, and K. K. Young. Evidence for Oscillation of Atmospheric Neutrinos. Phys. Rev. Lett., 81(8):1562–1567, Aug. 1998. doi: 10.1103/PhysRevLett.81.1562. URL https://ui.adsabs.harvard.edu/abs/1998PhRvL..81.1562F.

K. M. Gorski, B. D. Wandelt, F. K. Hansen, E. Hivon, and A. J. Banday. The HEALPix Primer. arXiv e-prints, art. astro-ph/9905275, May 1999. URL https://ui.adsabs.harvard.edu/abs/1999astro.ph..5275G.

D. Gruen, O. Friedrich, A. Amara, D. Bacon, C. Bonnett, W. Hartley, B. Jain, M. Jarvis, T. Kacprzak, E. Krause, A. Mana, E. Rozo, E. S. Rykoff, S. Seitz, E. Sheldon, M. A. Troxel, V. Vikram, T. M. C. Abbott, F. B. Abdalla, S. Allam, R. Armstrong, M. Banerji, A. H. Bauer, M. R. Becker, A. Benoit-Lévy, G. M. Bernstein, R. A. Bernstein, E. Bertin, S. L. Bridle, D. Brooks, E. Buckley-Geer, D. L. Burke, D. Capozzi, A. Carnero Rosell, M. Carrasco Kind, J. Carretero, M. Crocce, C. E. Cunha, C. B. D'Andrea, L. N. da Costa, D. L.

DePoy, S. Desai, H. T. Diehl, J. P. Dietrich, P. Doel, T. F. Eifler, A. F. Neto, E. Fernandez, B. Flaugher, P. Fosalba, J. Frieman, D. W. Gerdes, R. A. Gruendl, G. Gutierrez, K. Honscheid, D. J. James, K. Kuehn, N. Kuropatkin, O. Lahav, T. S. Li, M. Lima, M. A. G. Maia, M. March, P. Martini, P. Melchior, C. J. Miller, R. Miquel, J. J. Mohr, B. Nord, R. Ogando, A. A. Plazas, K. Reil, A. K. Romer, A. Roodman, M. Sako, E. Sanchez, V. Scarpine, M. Schubnell, I. Sevilla-Noarbe, R. C. Smith, M. Soares-Santos, F. Sobreira, E. Suchyta, M. E. C. Swanson, G. Tarle, J. Thaler, D. Thomas, A. R. Walker, R. H. Wechsler, J. Weller, Y. Zhang, and J. Zuntz. Weak lensing by galaxy troughs in DES Science Verification data. MNRAS, 455:3367–3380, Jan. 2016. doi: 10.1093/mnras/stv2506. URL http://adsabs.harvard.edu/abs/2016MNRAS.455.3367G.

L. Guzzo and The Vipers Team. VIPERS: An Unprecedented View of Galaxies and Large-scale Structure Halfway Back in the Life of the Universe. The Messenger, 151:41–46, Mar. 2013. URL http://adsabs.harvard.edu/abs/2013Msngr.151...41G.

L. Guzzo and Vipers Team. The VIMOS Public Extragalactic Redshift Survey (VIPERS): Science Highlights and Final Data Release. The Messenger, 168:40–47, June 2017. doi: 10.18727/0722-6691/5025. URL http://adsabs.harvard.edu/abs/2017Msngr.168...40G.

N. Hamaus, A. Pisani, P. M. Sutter, G. Lavaux, S. Escoffier, B. D. Wand elt, and J. Weller. Constraints on Cosmology and Gravity from the Dynamics of Voids. Phys. Rev. Lett., 117 (9):091302, Aug. 2016. doi: 10.1103/PhysRevLett.117.091302. URL https://ui.adsabs.harvard.edu/abs/2016PhRvL.117i1302H.

S. Hilbert, A. Barreira, G. Fabbian, P. Fosalba, C. Giocoli, S. Bose, M. Calabrese, C. Carbone, C. T. Davies, B. Li, C. Llinares, and P. Monaco. The accuracy of weak lensing simulations. MNRAS, 493(1):305–319, Mar. 2020. doi: 10.1093/mnras/staa281. URL https://ui.adsabs.harvard.edu/abs/2020MNRAS.493..305H.

E. W. Kolb and M. S. Turner. The early universe, volume 69. 1990. URL https://ui.adsabs.harvard.edu/abs/1990eaun.book.....K.

E. Komatsu, J. Dunkley, M. R. Nolta, C. L. Bennett, B. Gold, G. Hinshaw, N. Jarosik, D. Larson, M. Limon, L. Page, D. N. Spergel, M. Halpern, R. S. Hill, A. Kogut, S. S. Meyer, G. S. Tucker, J. L. Weiland, E. Wollack, and E. L. Wright. Five-Year Wilkinson Microwave Anisotropy Probe Observations: Cosmological Interpretation. ApJS, 180(2):330–376, Feb. 2009. doi: 10.1088/0067-0049/180/2/330. URL https://ui.adsabs.harvard.edu/abs/2009ApJS..180..330K.

E. Krause, T.-C. Chang, O. Doré, and K. Umetsu. The Weight of Emptiness: The Gravitational Lensing Signal of Stacked Voids. ApJ, 762(2):L20, Jan. 2013. doi: 10.1088/2041-8205/762/2/L20.

C. D. Kreisch, A. Pisani, C. Carbone, J. Liu, A. J. Hawken, E. Massara, D. N. Spergel, and B. D. Wandelt. Massive neutrinos leave fingerprints on cosmic voids. MNRAS, 488:4413–4426, Sept. 2019. doi: 10.1093/mnras/stz1944. URL https://ui.adsabs.harvard.edu/abs/2019MNRAS.488.4413K.

R. Laureijs, J. Amiaux, S. Arduini, J. L. Augueres, J. Brinchmann, R. Cole, M. Cropper, C. Dabin, L. Duvet, A. Ealet, B. Garilli, P. Gondoin, L. Guzzo, J. Hoar, H. Hoekstra, R. Holmes, T. Kitching, T. Maciaszek, Y. Mellier, F. Pasian, W. Percival, J. Rhodes, G. Saavedra Criado, M. Sauvage, R. Scaramella, L. Valenziano, S. Warren, R. Bender, F. Castander, A. Cimatti, O. Le Fèvre, H. Kurki-Suonio, M. Levi, P. Lilje, G. Meylan, R. Nichol, K. Pedersen, V. Popa, R. Rebolo Lopez, H. W. Rix, H. Rottgering, W. Zeilinger, F. Grupp, P. Hudelot, R. Massey,

M. Meneghetti, L. Miller, S. Paltani, S. Paulin-Henriksson, S. Pires, C. Saxton, T. Schrabback, G. Seidel, J. Walsh, N. Aghanim, L. Amendola, J. Bartlett, C. Baccigalupi, J. P. Beaulieu, K. Benabed, J. G. Cuby, D. Elbaz, P. Fosalba, G. Gavazzi, A. Helmi, I. Hook, M. Irwin, J. P. Kneib, M. Kunz, F. Mannucci, L. Moscardini, C. Tao, R. Teyssier, J. Weller, G. Zamorani, M. R. Zapatero Osorio, O. Boulade, J. J. Foumond, A. Di Giorgio, P. Guttridge, A. James, M. Kemp, J. Martignac, A. Spencer, D. Walton, T. Blümchen, C. Bonoli, F. Bortoletto, C. Cerna, L. Corcione, C. Fabron, K. Jahnke, S. Ligori, F. Madrid, L. Martin, G. Morgante, T. Pamplona, E. Prieto, M. Riva, R. Toledo, M. Trifoglio, F. Zerbi, F. Abdalla, M. Douspis, C. Grenet, S. Borgani, R. Bouwens, F. Courbin, J. M. Delouis, P. Dubath, A. Fontana, M. Frailis, A. Grazian, J. Koppenhöfer, O. Mansutti, M. Melchior, M. Mignoli, J. Mohr, C. Neissner, K. Noddle, M. Poncet, M. Scodeggio, S. Serrano, N. Shane, J. L. Starck, C. Surace, A. Taylor, G. Verdoes-Kleijn, C. Vuerli, O. R. Williams, A. Zacchei, B. Altieri, I. Escudero Sanz, R. Kohley, T. Oosterbroek, P. Astier, D. Bacon, S. Bardelli, C. Baugh, F. Bellagamba, C. Benoist, D. Bianchi, A. Biviano, E. Branchini, C. Carbone, V. Cardone, D. Clements, S. Colombi, C. Conselice, G. Cresci, N. Deacon, J. Dunlop, C. Fedeli, F. Fontanot, P. Franzetti, C. Giocoli, J. Garcia-Bellido, J. Gow, A. Heavens, P. Hewett, C. Heymans, A. Holland, Z. Huang, O. Ilbert, B. Joachimi, E. Jennins, E. Kerins, A. Kiessling, D. Kirk, R. Kotak, O. Krause, O. Lahav, F. van Leeuwen, J. Lesgourgues, M. Lombardi, M. Magliocchetti, K. Maguire, E. Majerotto, R. Maoli, F. Marulli, S. Maurogordato, H. McCracken, R. McLure, A. Melchiorri, A. Merson, M. Moresco, M. Nonino, P. Norberg, J. Peacock, R. Pello, M. Penny, V. Pettorino, C. Di Porto, L. Pozzetti, C. Quercellini, M. Radovich, A. Rassat, N. Roche, S. Ronayette, E. Rossetti, B. Sartoris, P. Schneider, E. Semboloni, S. Serjeant, F. Simpson, C. Skordis, G. Smadja, S. Smartt, P. Spano, S. Spiro, M. Sullivan, A. Tilquin, R. Trotta, L. Verde, Y. Wang, G. Williger, G. Zhao, J. Zoubian, and E. Zucca. Euclid Definition Study Report. arXiv e-prints, art. arXiv:1110.3193, Oct. 2011. URL https://ui.adsabs.harvard.edu/abs/2011arXiv1110.3193L.

J. Lesgourgues and S. Pastor. Massive neutrinos and cosmology. Phys. Rep., 429(6):307–379, July 2006. doi: 10.1016/j.physrep.2006.04.001. URL https://ui.adsabs.harvard.edu/abs/2006PhR...429..307L.

J. Lesgourgues and S. Pastor. Massive neutrinos and cosmology. Physics Reports, 429(6): 307–379, mar 2006. doi: 10.1016/j.physrep.2006.04.001. URL http://arxiv.org/abs/astro-ph/0603494http://dx.doi.org/10.1016/j.physrep.2006.04.001.

J. Lesgourgues and S. Pastor. Neutrino mass from cosmology, 2012. ISSN 16877357.

J. Lesgourgues and S. Pastor. Neutrino cosmology and Planck. New Journal of Physics, 16, 2014. ISSN 13672630. doi: 10.1088/1367-2630/16/6/065002.

S. Masi. The BOOMERanG experiment and the curvature of the universe. Progress in Particle and Nuclear Physics, 48(1):243–261, Jan. 2002. doi: 10.1016/S0146-6410(02)00131-X. URL https://ui.adsabs.harvard.edu/abs/2002PrPNP..48..243M.

E. Massara, F. Villaescusa-Navarro, M. Viel, and P. M. Sutter. Voids in massive neutrino cosmologies. JCAP, 11:018, Nov. 2015. doi: 10.1088/1475-7516/2015/11/018. URL https://ui.adsabs.harvard.edu/abs/2015JCAP...11..018M.

B. O. Mummery, I. G. McCarthy, S. Bird, and J. Schaye. The separate and combined effects of baryon physics and neutrino free streaming on large-scale structure. MNRAS, 471(1):227–242, Oct. 2017. doi: 10.1093/mnras/stx1469. URL https://ui.adsabs.harvard.edu/abs/2017MNRAS.471..227M.

S. Nadathur, S. Hotchkiss, and R. Crittenden. Tracing the gravitational potential using cosmic voids. MNRAS, 467(4):4067–4079, June 2017. doi: 10.1093/mnras/stx336. URL https://ui.adsabs.harvard.edu/abs/2017MNRAS.467.4067N.

K. Nakamura and S. Petkov. Neutrino Mass, Mixing and Oscillations. Chin. Phys. C, 40(10): 100001, 2016. doi: 10.1088/1674-1137/40/10/100001.

M. C. Neyrinck, M. A. Aragón-Calvo, D. Jeong, and X. Wang. A halo bias function measured deeply into voids without stochasticity. MNRAS, 441(1):646–655, June 2014. doi: 10.1093/mnras/stu589. URL https://ui.adsabs.harvard.edu/abs/2014MNRAS.441..646N.

R. B. Patterson. Prospects for Measurement of the Neutrino Mass Hierarchy. Annual Review of Nuclear and Particle Science, 65:177–192, Oct. 2015. doi: 10.1146/annurev-nucl-102014-021916. URL https://ui.adsabs.harvard.edu/abs/2015ARNPS..65..177P.

P. J. E. Peebles. The large-scale structure of the universe. 1980. URL https://ui.adsabs.harvard.edu/abs/1980lssu.book.....P.

S. Perlmutter, G. Aldering, S. Deustua, S. Fabbro, G. Goldhaber, D. E. Groom, A. G. Kim, M. Y. Kim, R. A. Knop, P. Nugent, C. R. Pennypacker, M. della Valle, R. S. Ellis, R. G. McMahon, N. Walton, A. Fruchter, N. Panagia, A. Goobar, I. M. Hook, C. Lidman, R. Pain, P. Ruiz-Lapuente, B. Schaefer, and Supernova Cosmology Project. Cosmology From Type IA Supernovae: Measurements, Calibration Techniques, and Implications. In American Astronomical Society Meeting Abstracts, volume 191 of American Astronomical Society Meeting Abstracts, page 85.04, Dec. 1997. URL https://ui.adsabs.harvard.edu/abs/1997AAS...191.8504P.

S. Perlmutter, G. Aldering, G. Goldhaber, R. A. Knop, P. Nugent, P. G. Castro, S. Deustua, S. Fabbro, A. Goobar, D. E. Groom, I. M. Hook, A. G. Kim, M. Y. Kim, J. C. Lee, N. J. Nunes, R. Pain, C. R. Pennypacker, R. Quimby, C. Lidman, R. S. Ellis, M. Irwin, R. G. McMahon, P. Ruiz-Lapuente, N. Walton, B. Schaefer, B. J. Boyle, A. V. Filippenko, T. Matheson, A. S. Fruchter, N. Panagia, H. J. M. Newberg, W. J. Couch, and T. S. C. Project. Measurements of Ω and Λ from 42 High-Redshift Supernovae. ApJ, 517(2):565–586, June 1999. doi: 10.1086/307221. URL https://ui.adsabs.harvard.edu/abs/1999ApJ...517..565P.

A. Petri. Mocking the weak lensing universe: The LensTools Python computing package. Astronomy and Computing, 17:73–79, Oct. 2016. doi: 10.1016/j.ascom.2016.06.001. URL https://ui.adsabs.harvard.edu/abs/2016A&C....17...73P.

A. Pisani, P. M. Sutter, N. Hamaus, E. Alizadeh, R. Biswas, B. D. Wandelt, and C. M. Hirata. Counting voids to probe dark energy. Phys. Rev. D, 92(8):083531, Oct. 2015. doi: 10.1103/PhysRevD.92.083531. URL https://ui.adsabs.harvard.edu/abs/2015PhRvD..92h3531P.

Planck Collaboration, P. A. R. Ade, N. Aghanim, C. Armitage-Caplan, M. Arnaud, M. Ashdown, F. Atrio-Barand ela, J. Aumont, C. Baccigalupi, A. J. Banday, R. B. Barreiro, J. G. Bartlett, E. Battaner, K. Benabed, A. Benoît, A. Benoit-Lévy, J. P. Bernard, M. Bersanelli, P. Bielewicz, J. Bobin, J. J. Bock, A. Bonaldi, J. R. Bond, J. Borrill, F. R. Bouchet, M. Bridges, M. Bucher, C. Burigana, R. C. Butler, E. Calabrese, B. Cappellini, J. F. Cardoso, A. Catalano, A. Challinor, A. Chamballu, R. R. Chary, X. Chen, H. C. Chiang, L. Y. Chiang, P. R. Christensen, S. Church, D. L. Clements, S. Colombi, L. P. L. Colombo, F. Couchot, A. Coulais, B. P. Crill, A. Curto, F. Cuttaia, L. Danese, R. D. Davies, R. J. Davis, P. de Bernardis, A. de Rosa, G. de Zotti, J. Delabrouille, J. M. Delouis, F. X. Désert, C. Dickinson, J. M. Diego, K. Dolag, H. Dole, S. Donzelli, O. Doré, M. Douspis, J. Dunkley, X. Dupac, G. Efstathiou, F. Elsner,

T. A. Enßlin, H. K. Eriksen, F. Finelli, O. Forni, M. Frailis, A. A. Fraisse, E. Franceschi, T. C. Gaier, S. Galeotta, S. Galli, K. Ganga, M. Giard, G. Giardino, Y. Giraud-Héraud, E. Gjerløw, J. González-Nuevo, K. M. Górski, S. Gratton, A. Gregorio, A. Gruppuso, J. E. Gudmundsson, J. Haissinski, J. Hamann, F. K. Hansen, D. Hanson, D. Harrison, S. Henrot-Versillé, C. Hernández-Monteagudo, D. Herranz, S. R. Hildebrand t, E. Hivon, M. Hobson, W. A. Holmes, A. Hornstrup, Z. Hou, W. Hovest, K. M. Huffenberger, A. H. Jaffe, T. R. Jaffe, J. Jewell, W. C. Jones, M. Juvela, E. Keihänen, R. Keskitalo, T. S. Kisner, R. Kneissl, J. Knoche, L. Knox, M. Kunz, H. Kurki-Suonio, G. Lagache, A. Lähteenmäki, J. M. Lamarre, A. Lasenby, M. Lattanzi, R. J. Laureijs, C. R. Lawrence, S. Leach, J. P. Leahy, R. Leonardi, J. León-Tavares, J. Lesgourgues, A. Lewis, M. Liguori, P. B. Lilje, M. Linden-Vørnle, M. López-Caniego, P. M. Lubin, J. F. Macías-Pérez, B. Maffei, D. Maino, N. Mand olesi, M. Maris, D. J. Marshall, P. G. Martin, E. Martínez-González, S. Masi, M. Massardi, S. Matarrese, F. Matthai, P. Mazzotta, P. R. Meinhold, A. Melchiorri, J. B. Melin, L. Mendes, E. Menegoni, A. Mennella, M. Migliaccio, M. Millea, S. Mitra, M. A. Miville-Deschênes, A. Moneti, L. Montier, G. Morgante, D. Mortlock, A. Moss, D. Munshi, J. A. Murphy, P. Naselsky, F. Nati, P. Natoli, C. B. Netterfield, H. U. Nørgaard-Nielsen, F. Noviello, D. Novikov, I. Novikov, I. J. O'Dwyer, S. Osborne, C. A. Oxborrow, F. Paci, L. Pagano, F. Pajot, R. Paladini, D. Paoletti, B. Partridge, F. Pasian, G. Patanchon, D. Pearson, T. J. Pearson, H. V. Peiris, O. Perdereau, L. Perotto, F. Perrotta, V. Pettorino, F. Piacentini, M. Piat, E. Pierpaoli, D. Pietrobon, S. Plaszczynski, P. Platania, E. Pointecouteau, G. Polenta, N. Ponthieu, L. Popa, T. Poutanen, G. W. Pratt, G. Prézeau, S. Prunet, J. L. Puget, J. P. Rachen, W. T. Reach, R. Rebolo, M. Reinecke, M. Remazeilles, C. Renault, S. Ricciardi, T. Riller, I. Ristorcelli, G. Rocha, C. Rosset, G. Roudier, M. Rowan-Robinson, J. A. Rubiño-Martín, B. Rusholme, M. Sandri, D. Santos, M. Savelainen, G. Savini, D. Scott, M. D. Seiffert, E. P. S. Shellard, L. D. Spencer, J. L. Starck, V. Stolyarov, R. Stompor, R. Sudiwala, R. Sunyaev, F. Sureau, D. Sutton, A. S. Suur-Uski, J. F. Sygnet, J. A. Tauber, D. Tavagnacco, L. Terenzi, L. Toffolatti, M. Tomasi, M. Tristram, M. Tucci, J. Tuovinen, M. Türler, G. Umana, L. Valenziano, J. Valiviita, B. Van Tent, P. Vielva, F. Villa, N. Vittorio, L. A. Wade, B. D. Wandelt, I. K. Wehus, M. White, S. D. M. White, A. Wilkinson, D. Yvon, A. Zacchei, and A. Zonca. Planck 2013 results. XVI. Cosmological parameters. A&A, 571:A16, Nov. 2014. doi: 10.1051/0004-6361/201321591. URL https://ui.adsabs.harvard.edu/abs/2014A&A...571A..16P.

Planck Collaboration, N. Aghanim, Y. Akrami, M. Ashdown, J. Aumont, C. Baccigalupi, M. Ballardini, A. J. Banday, R. B. Barreiro, N. Bartolo, S. Basak, R. Battye, K. Benabed, J. P. Bernard, M. Bersanelli, P. Bielewicz, J. J. Bock, J. R. Bond, J. Borrill, F. R. Bouchet, F. Boulanger, M. Bucher, C. Burigana, R. C. Butler, E. Calabrese, J. F. Cardoso, J. Carron, A. Challinor, H. C. Chiang, J. Chluba, L. P. L. Colombo, C. Combet, D. Contreras, B. P. Crill, F. Cuttaia, P. de Bernardis, G. de Zotti, J. Delabrouille, J. M. Delouis, E. Di Valentino, J. M. Diego, O. Doré, M. Douspis, A. Ducout, X. Dupac, S. Dusini, G. Efstathiou, F. Elsner, T. A. Enßlin, H. K. Eriksen, Y. Fantaye, M. Farhang, J. Fergusson, R. Fernandez-Cobos, F. Finelli, F. Forastieri, M. Frailis, A. A. Fraisse, E. Franceschi, A. Frolov, S. Galeotta, S. Galli, K. Ganga, R. T. Génova-Santos, M. Gerbino, T. Ghosh, J. González-Nuevo, K. M. Górski, S. Gratton, A. Gruppuso, J. E. Gudmundsson, J. Hamann, W. Handley, F. K. Hansen, D. Herranz, S. R. Hildebrandt, E. Hivon, Z. Huang, A. H. Jaffe, W. C. Jones, A. Karakci, E. Keihänen, R. Keskitalo, K. Kiiveri, J. Kim, T. S. Kisner, L. Knox, N. Krachmalnicoff, M. Kunz, H. Kurki-Suonio, G. Lagache, J. M. Lamarre, A. Lasenby, M. Lattanzi, C. R. Lawrence, M. Le Jeune, P. Lemos, J. Lesgourgues, F. Levrier, A. Lewis, M. Liguori, P. B. Lilje, M. Lilley, V. Lindholm, M. López-Caniego, P. M. Lubin, Y. Z. Ma, J. F. Macías-Pérez, G. Maggio, D. Maino, N. Mandolesi, A. Mangilli, A. Marcos-Caballero, M. Maris, P. G. Martin, M. Martinelli, E. Martínez-González, S. Matarrese, N. Mauri, J. D. McEwen, P. R. Meinhold, A. Melchiorri, A. Mennella, M. Migliaccio, M. Millea, S. Mitra, M. A. Miville-Deschênes, D. Molinari, L. Montier, G. Morgante, A. Moss, P. Natoli, H. U. Nørgaard-Nielsen, L. Pagano, D. Paoletti, B. Par-

tridge, G. Patanchon, H. V. Peiris, F. Perrotta, V. Pettorino, F. Piacentini, L. Polastri, G. Polenta, J. L. Puget, J. P. Rachen, M. Reinecke, M. Remazeilles, A. Renzi, G. Rocha, C. Rosset, G. Roudier, J. A. Rubiño-Martín, B. Ruiz-Granados, L. Salvati, M. Sandri, M. Savelainen, D. Scott, E. P. S. Shellard, C. Sirignano, G. Sirri, L. D. Spencer, R. Sunyaev, A. S. Suur-Uski, J. A. Tauber, D. Tavagnacco, M. Tenti, L. Toffolatti, M. Tomasi, T. Trombetti, L. Valenziano, J. Valiviita, B. Van Tent, L. Vibert, P. Vielva, F. Villa, N. Vittorio, B. D. Wand elt, I. K. Wehus, M. White, S. D. M. White, A. Zacchei, and A. Zonca. Planck 2018 results. VI. Cosmological parameters. arXiv e-prints, art. arXiv:1807.06209, July 2018. URL https://ui.adsabs.harvard.edu/abs/2018arXiv180706209P.

E. Platen, R. van de Weygaert, and B. J. T. Jones. A cosmic watershed: the WVF void detection technique. MNRAS, 380(2):551–570, Sept. 2007. doi: 10.1111/j.1365-2966.2007.12125.x. URL https://ui.adsabs.harvard.edu/abs/2007MNRAS.380..551P.

A. Refregier. Weak Gravitational Lensing by Large-Scale Structure. ARA&A, 41:645–668, Jan. 2003. doi: 10.1146/annurev.astro.41.111302.102207. URL https://ui.adsabs.harvard.edu/abs/2003ARA&A..41..645R.

A. G. Riess, A. V. Filippenko, P. Challis, A. Clocchiatti, A. Diercks, P. M. Garnavich, R. L. Gilliland, C. J. Hogan, S. Jha, R. P. Kirshner, B. Leibundgut, M. M. Phillips, D. Reiss, B. P. Schmidt, R. A. Schommer, R. C. Smith, J. Spyromilio, C. Stubbs, N. B. Suntzeff, and J. Tonry. Observational Evidence from Supernovae for an Accelerating Universe and a Cosmological Constant. AJ, 116(3):1009–1038, Sept. 1998. doi: 10.1086/300499. URL https://ui.adsabs.harvard.edu/abs/1998AJ....116.1009R.

S. Saito, M. Takada, and A. Taruya. Nonlinear power spectrum in the presence of massive neutrinos: Perturbation theory approach, galaxy bias, and parameter forecasts. Phys. Rev. D, 80 (8):083528, Oct. 2009. doi: 10.1103/PhysRevD.80.083528. URL https://ui.adsabs.harvard.edu/abs/2009PhRvD..80h3528S.

C. Sánchez, J. Clampitt, A. Kovacs, B. Jain, J. García-Bellido, S. Nadathur, D. Gruen, N. Hamaus, D. Huterer, P. Vielzeuf, A. Amara, C. Bonnett, J. DeRose, W. G. Hartley, M. Jarvis, O. Lahav, R. Miquel, E. Rozo, E. S. Rykoff, E. Sheldon, R. H. Wechsler, J. Zuntz, T. M. C. Abbott, F. B. Abdalla, J. Annis, A. Benoit-Lévy, G. M. Bernstein, R. A. Bernstein, E. Bertin, D. Brooks, E. Buckley-Geer, A. Carnero Rosell, M. Carrasco Kind, J. Carretero, M. Crocce, C. E. Cunha, C. B. D'Andrea, L. N. da Costa, S. Desai, H. T. Diehl, J. P. Dietrich, P. Doel, A. E. Evrard, A. Fausti Neto, B. Flaugher, P. Fosalba, J. Frieman, E. Gaztanaga, R. A. Gruendl, G. Gutierrez, K. Honscheid, D. J. James, E. Krause, K. Kuehn, M. Lima, M. A. G. Maia, J. L. Marshall, P. Melchior, A. A. Plazas, K. Reil, A. K. Romer, E. Sanchez, M. Schubnell, I. Sevilla-Noarbe, R. C. Smith, M. Soares-Santos, F. Sobreira, E. Suchyta, G. Tarle, D. Thomas, A. R. Walker, J. Weller, and DES Collaboration. Cosmic voids and void lensing in the Dark Energy Survey Science Verification data. MNRAS, 465(1):746–759, Feb. 2017. doi: 10.1093/mnras/stw2745. URL https://ui.adsabs.harvard.edu/abs/2017MNRAS.465..746S.

C. Sánchez, J. Clampitt, A. Kovacs, B. Jain, J. García-Bellido, S. Nadathur, D. Gruen, N. Hamaus, D. Huterer, P. Vielzeuf, A. Amara, C. Bonnett, J. DeRose, W. G. Hartley, M. Jarvis, O. Lahav, R. Miquel, E. Rozo, E. S. Rykoff, E. Sheldon, R. H. Wechsler, J. Zuntz, T. M. Abbott, F. B. Abdalla, J. Annis, A. Benoit-Lévy, G. M. Bernstein, R. A. Bernstein, E. Bertin, D. Brooks, E. Buckley-Geer, A. Carnero Rosell, M. Carrasco Kind, J. Carretero, M. Crocce, C. E. Cunha, C. B. D'Andrea, L. N. da Costa, S. Desai, H. T. Diehl, J. P. Dietrich, P. Doel, A. E. Evrard, A. Fausti Neto, B. Flaugher, P. Fosalba, J. Frieman, E. Gaztanaga, R. A. Gruendl, G. Gutierrez, K. Honscheid, D. J. James, E. Krause, K. Kuehn, M. Lima, M. A. Maia, J. L. Marshall, P. Melchior, A. A. Plazas, K. Reil, A. K. Romer, E. Sanchez, M. Schubnell, I. Sevilla-Noarbe, R. C. Smith, M. Soares-Santos, F. Sobreira, E. Suchyta, G. Tarle, D. Thomas, A. R. Walker,

and J. Weller. Cosmic voids and void lensing in the Dark Energy Survey Science Verification data. Monthly Notices of the Royal Astronomical Society, 465(1), 2017. ISSN 13652966. doi: 10.1093/mnras/stw2745.

N. Schuster, N. Hamaus, A. Pisani, C. Carbone, C. D. Kreisch, G. Pollina, and J. Weller. The bias of cosmic voids in the presence of massive neutrinos. JCAP, 2019(12):055, Dec. 2019. doi: 10.1088/1475-7516/2019/12/055. URL https://ui.adsabs.harvard.edu/abs/2019JCAP...12..055S.

K. Sharon, M. B. Bayliss, H. Dahle, S. J. Dunham, M. K. Florian, M. D. Gladders, T. L. Johnson, G. Mahler, R. Paterno-Mahler, J. R. Rigby, K. E. Whitaker, M. Akhshik, B. P. Koester, K. Murray, J. D. Remolina González, and E. Wuyts. Strong Lens Models for 37 Clusters of Galaxies from the SDSS Giant Arcs Survey. ApJS, 247(1):12, Mar. 2020. doi: 10.3847/1538-4365/ab5f13. URL https://ui.adsabs.harvard.edu/abs/2020ApJS..247...12S.

G. F. Smoot. COBE observations and results. In L. Maiani, F. Melchiorri, and N. Vittorio, editors, 3K cosmology, volume 476 of American Institute of Physics Conference Series, pages 1–10, May 1999. doi: 10.1063/1.59326. URL https://ui.adsabs.harvard.edu/abs/1999AIPC..476....1S.

F. J. P. Soler, C. D. Froggatt, and F. Muheim. Neutrinos in Particle Physics, Astrophysics and Cosmology. 2009. URL https://ui.adsabs.harvard.edu/abs/2009nppa.book.....S.

N. Straumann. The history of the cosmological constant problem. arXiv e-prints, art. gr-qc/0208027, Aug. 2002. URL https://ui.adsabs.harvard.edu/abs/2002gr.qc.....8027S.

P. M. Sutter, G. Lavaux, N. Hamaus, A. Pisani, B. D. Wandelt, M. Warren, F. Villaescusa-Navarro, P. Zivick, Q. Mao, and B. B. Thompson. VIDE: The Void IDentification and Examination toolkit. Astronomy and Computing, 9:1–9, Mar. 2015. doi: 10.1016/j.ascom.2014.10.002. URL https://ui.adsabs.harvard.edu/abs/2015A&C.....9....1S.

J. A. Tyson. Large Synoptic Survey Telescope: Overview. In J. A. Tyson and S. Wolff, editors, Survey and Other Telescope Technologies and Discoveries, volume 4836 of Society of Photo-Optical Instrumentation Engineers (SPIE) Conference Series, pages 10–20, Dec. 2002. doi: 10.1117/12.456772. URL https://ui.adsabs.harvard.edu/abs/2002SPIE.4836...10T.

R. van de Weygaert and E. Platen. Cosmic Voids: Structure, Dynamics and Galaxies. In International Journal of Modern Physics Conference Series, volume 1 of International Journal of Modern Physics Conference Series, pages 41–66, Jan. 2011. doi: 10.1142/S2010194511000092. URL https://ui.adsabs.harvard.edu/abs/2011IJMPS...1...41V.

R. van de Weygaert and W. Schaap. The Cosmic Web: Geometric Analysis, volume 665, pages 291–413. 2009. doi: 10.1007/978-3-540-44767-2_11. URL https://ui.adsabs.harvard.edu/abs/2009LNP...665..291V.

L. Van Waerbeke and Y. Mellier. Gravitational Lensing by Large Scale Structures: A Review. arXiv e-prints, art. astro-ph/0305089, May 2003. URL https://ui.adsabs.harvard.edu/abs/2003astro.ph..5089V.

P. Vielzeuf, A. Kovács, U. Demirbozan, P. Fosalba, E. Baxter, N. Hamaus, D. Huterer, R. Miquel, S. Nadathur, G. Pollina, C. Sánchez, L. Whiteway, T. M. C. Abbott, S. Allam, J. Annis, S. Avila, D. Brooks, D. L. Burke, A. C. Rosell, M. C. Kind, J. Carretero, R. Cawthon, M. Costanzi, L. N. da Costa, J. De Vicente, S. Desai, H. T. Diehl, P. Doel, T. F. Eifler, S. Everett,

B. Flaugher, J. Frieman, J. García-Bellido, E. Gaztanaga, D. W. Gerdes, D. Gruen, R. A. Gruendl, J. Gschwend, G. Gutierrez, W. G. Hartley, D. L. Hollowood, K. Honscheid, D. J. James, K. Kuehn, N. Kuropatkin, O. Lahav, M. Lima, M. A. G. Maia, M. March, J. L. Marshall, P. Melchior, F. Menanteau, A. Palmese, F. P. Chinchón, A. A. Plazas, E. Sanchez, V. Scarpine, S. Serrano, I. S. Noarbe, M. Smith, E. Suchyta, G. Tarle, D. Thomas, J. Weller, and J. Zuntz. Dark Energy Survey Year 1 Results: the lensing imprint of cosmic voids on the Cosmic Microwave Background. (November 2019), 2019. URL http://arxiv.org/abs/1911.02951.

X. Wang, M. Tegmark, and M. Zaldarriaga. Is cosmology consistent? Phys. Rev. D, 65 (12):123001, June 2002. doi: 10.1103/PhysRevD.65.123001. URL https://ui.adsabs.harvard.edu/abs/2002PhRvD..65l3001W.

S. Weinberg. The Cosmological Constant Problems (Talk given at Dark Matter 2000, February, 2000). arXiv e-prints, art. astro-ph/0005265, May 2000. URL https://ui.adsabs.harvard.edu/abs/2000astro.ph..5265W.

D. G. York, J. Adelman, J. Anderson, John E., S. F. Anderson, J. Annis, N. A. Bahcall, J. A. Bakken, R. Barkhouser, S. Bastian, E. Berman, W. N. Boroski, S. Bracker, C. Briegel, J. W. Briggs, J. Brinkmann, R. Brunner, S. Burles, L. Carey, M. A. Carr, F. J. Castander, B. Chen, P. L. Colestock, A. J. Connolly, J. H. Crocker, I. Csabai, P. C. Czarapata, J. E. Davis, M. Doi, T. Dombeck, D. Eisenstein, N. Ellman, B. R. Elms, M. L. Evans, X. Fan, G. R. Federwitz, L. Fiscelli, S. Friedman, J. A. Frieman, M. Fukugita, B. Gillespie, J. E. Gunn, V. K. Gurbani, E. de Haas, M. Haldeman, F. H. Harris, J. Hayes, T. M. Heckman, G. S. Hennessy, R. B. Hindsley, S. Holm, D. J. Holmgren, C.-h. Huang, C. Hull, D. Husby, S.-I. Ichikawa, T. Ichikawa, Ž. Ivezić, S. Kent, R. S. J. Kim, E. Kinney, M. Klaene, A. N. Kleinman, S. Kleinman, G. R. Knapp, J. Korienek, R. G. Kron, P. Z. Kunszt, D. Q. Lamb, B. Lee, R. F. Leger, S. Limmongkol, C. Lindenmeyer, D. C. Long, C. Loomis, J. Loveday, R. Lucinio, R. H. Lupton, B. MacKinnon, E. J. Mannery, P. M. Mantsch, B. Margon, P. McGehee, T. A. McKay, A. Meiksin, A. Merelli, D. G. Monet, J. A. Munn, V. K. Narayanan, T. Nash, E. Neilsen, R. Neswold, H. J. Newberg, R. C. Nichol, T. Nicinski, M. Nonino, N. Okada, S. Okamura, J. P. Ostriker, R. Owen, A. G. Pauls, J. Peoples, R. L. Peterson, D. Petravick, J. R. Pier, A. Pope, R. Pordes, A. Prosapio, R. Rechenmacher, T. R. Quinn, G. T. Richards, M. W. Richmond, C. H. Rivetta, C. M. Rockosi, K. Ruthmansdorfer, D. Sand ford, D. J. Schlegel, D. P. Schneider, M. Sekiguchi, G. Sergey, K. Shimasaku, W. A. Siegmund, S. Smee, J. A. Smith, S. Snedden, R. Stone, C. Stoughton, M. A. Strauss, C. Stubbs, M. SubbaRao, A. S. Szalay, I. Szapudi, G. P. Szokoly, A. R. Thakar, C. Tremonti, D. L. Tucker, A. Uomoto, D. Vanden Berk, M. S. Vogeley, P. Waddell, S.-i. Wang, M. Watanabe, D. H. Weinberg, B. Yanny, N. Yasuda, and SDSS Collaboration. The Sloan Digital Sky Survey: Technical Summary. AJ, 120(3):1579–1587, Sept. 2000. doi: 10.1086/301513. URL https://ui.adsabs.harvard.edu/abs/2000AJ....120.1579Y.

C. Zhao, C. Tao, Y. Liang, F.-S. Kitaura, and C.-H. Chuang. DIVE in the cosmic web: voids with Delaunay triangulation from discrete matter tracer distributions. MNRAS, 459(3):2670–2680, July 2016. doi: 10.1093/mnras/stw660. URL https://ui.adsabs.harvard.edu/abs/2016MNRAS.459.2670Z.